A NEW QUANTITATIVE METHOD FOR THE DETERMINATION OF REGIONAL RATES OF CEREBRAL PROTEIN SYNTHESIS FROM L-[1 11C]LEUCINE PET IMAGES

Veronese, Mattia

Awarding institution:
King's College London
University of Padua

Title: A NEW QUANTITATIVE METHOD FOR THE DETERMINATION OF REGIONAL RATES OF CEREBRAL PROTEIN SYNTHESIS FROM L-[1 11C]LEUCINE PET IMAGES

Author: Mattia Veronese

A NEW QUANTITATIVE METHOD FOR THE DETERMINATION OF REGIONAL RATES OF CEREBRAL PROTEIN SYNTHESIS FROM L-[1 $-^{11}C$]LEUCINE PET IMAGES

Mattia Veronese

April 2009

Contents

Background

The work that we are presenting comes from a collaboration between the Bioengineering group of the University of Padova and the Section of Neuroadaptation and Protein Metabolism (SNPM).

SNPM is an integral part of the Neuroscience Research community at the National Institutes of Health (NIH), the primary United States Federal agency for conducting and supporting medical research. SNPM laboratories are located on the NIH campus in Bethesda, Maryland in the Division of Intramural Research of the National Institute of Mental Health (NIMH).

The aim of SNPM research is to understand the role of protein metabolism in adaptive responses of the nervous system and to do it they develop, apply, and refine imaging methods that can be used to quantitatively measure these changes in vivo in all structures of the nervous system in animals and in man.

The role of the Bioengineering group of Padova University in this collaboration is to provide ideas to develop and improve these new quantification methods, using its experience in kinetic model design.

Figure 1: The pictures show the NIH and its scientists at work. NIH is an agency of the U.S. Department of Health and Human Services. With the headquarters in Bethesda, Maryland, the NIH has more than 18,000 employees on the main campus and at satellite sites across the United States. Helping to lead the way toward important medical discoveries that improve people's health and save lives, NIH scientists investigate ways to prevent disease as well as the causes, treatments, and even cures for common and rare diseases. Composed of 27 Institutes and Centers, the NIH provides leadership and financial support to researchers in every state and throughout the world.
The NIH annually invests over $28 billion in medical research. More than 83% of the NIH's funding is awarded through almost $50,000$ competitive grants to more than $325,000$ researchers at over $3,000$ universities, medical schools, and other research institutions in every state and around the world. About 10% of the NIH's budget supports projects conducted by nearly 6,000 scientists in its own laboratories (`www.nih.gov`).

Chapter 1

Introduction

The Biosynthesis of proteins is a fundamental process for the physiological maintenance and functioning of organisms. In fact, it is through the action of the different proteins that every biological system can achieve and control all metabolic processes required for life. The event of the synthesis, even though it follows a well-defined process common to each cell of the organism, assumes different facets depending on the particular biological system to which it refers. For example in the central nervous system (CNS), de novo protein synthesis is critical for adaptive responses such as long-term memory formation. Animal studies indicate, in fact, that regional rates of cerebral protein synthesis (rCPS) are altered in models of various clinical disorders and in certain physiologic states. It has been shown that rCPS is modified during brain development and during the process of aging and it is directly correlated to many of the diseases of the CNS. With the development and validation of the L-[1 $-^{11}$ C]leucine PET method ([28]; [30]), fully quantitative measurement of rCPS in vivo in human subjects is now possible. The method has been implemented in awake, healthy young men and the results demonstrated that reproducible measurements of rCPS with low variability can be obtained [2]. Recently, the method has been utilized in study of normal human brain in awake and under

anesthesia [3]. Future applications are expected in subjects with neurodegenerative diseases, and with neurodevelopmental disorders.

The analysis of L-[1 $-^{11}$ C]leucine PET data in non-human primates [30] and in human subjects ([34]; [2]; [3]) is focused in particular to the region-of-interest (ROI) level. This is due to two reasons: firstly the ROI data are averaged over large numbers of voxels in the field of view of the PET scanner, and so noise is reduced. Secondly, the computational burden of analyzing data at the voxel level can be extraordinarily high. Even though the elaboration at ROI level has a lot of advantages, it also represents an important limitation for the homogenous tissue kinetic model (HOM) that the method uses for the rCPS quantification. In fact, due to the limited spatial resolution of PET, a region of interest (ROI) likely contains a heterogeneous mixture of tissues, a characteristic that the HOM does not take into account in its representation of the system. A different approach to the problem can be done through Spectral Analysis (SA) [8]. This technique applies to heterogeneous as well as homogeneous tissues, and therefore, it might be an alternative quantitative method. In the present work we found that the standard SA algorithms ([8]; [36]) cannot be directly applied to the L-[1 $-^{11}$ C]leucine PET data because the estimates that they provide for rCPS at the ROI level are not physiological and in are not in agreement with the previous studies ([2]; [35]). For this reason we developed a new algorithm based on SA to estimate rCPS and the other variables of interest at the ROI level. The method was tested in simulation experiments and then applied to measured data. The results were compared to the estimates provided by the alternative approaches for rCPS quantification from the L-[1 $-^{11}$ C]leucine PET data.

Chapter 2

The Biosynthesis of Protein

2.1 The regional rate of cerebral protein synthesis

2.1.1 The importance of protein synthesis

Biosynthesis of proteins is a fundamental process necessary for the physiological maintenance and functioning of organisms. In the central nervous system (CNS), de novo protein synthesis is critical for adaptive responses such as long-term memory formation.

Animal studies indicate that the protein synthesis is altered in models of various clinical conditions including fragile X syndrome[1] [25], Phenylketonuria[2] [29], ischemia/stroke [40], CNS tumors [39], epilepsy [7], and in certain physiologic states such as slow wave sleep [22]. Studies in rodents have demonstrated that de novo protein synthesis changes during the process of ag-

[1]Fragile X syndrome (FrX) is the most common inherited form of mental retardation in males with an estimated frequency of 1/4000. It is caused by the absence of the fragile X mental retardation protein (FMRP) encoded by the silenced fragile X mental retardation gene (Fmr1).

[2]Phenylketonuria (PKU) is an autosomal recessive genetic disorder characterized by a deficiency in the enzyme phenylalanine hydroxylase (PAH). This enzyme is necessary to metabolize the amino acid phenylalanine to the amino acid tyrosine. This condition can cause problems with brain development, leading to progressive mental retardation and seizures.

ing [16] and during brain development [33]. Activity-dependent protein synthesis is thought to be an integral step in many forms of synaptic plasticity [23]. This fact is confirmed in a study about the developmental plasticity in monkeys where regionally selective changes in protein synthesis were found. For all these reasons, a measure of the regional rate of cerebral protein synthesis (rCPS) would have many applications in the study of normal human brain and in clinical medicine by providing a new tool to investigate disorders of brain development, recovery from brain injury, and neurodegenerative diseases. In particular, variations in rCPS likely reflect adaptive processes taking place over a longer period of time compared with the acute physiological changes signaled by measurements of regional cerebral metabolic rate for glucose or cerebral blood flow. Thus, changes in rCPS are expected to reflect long-term adaptive phenomena and provide complementary information to existing techniques on elucidating CNS processes.

2.1.2 A PET technique for the measurement of rCPS

One of the most informative ways to study the protein synthesis is through functional imaging. Functional imaging methods have been developed, refined and finally applied to quantitatively measure the specific metabolism processes *in vivo* in all structures of the nervous system in animals and in man. Through them maps of the absolute rates of physiological or biochemical processes simultaneously can be provided in all parts of the body of the living organism, but for the particular purposes of this work, we will focus to those techniques that investigate the human brain.

There are different types of functional brain imaging methods, such as the quantitative autoradiography, the functional magnetic resonance imaging (fMRI), the laser Doppler flowme-

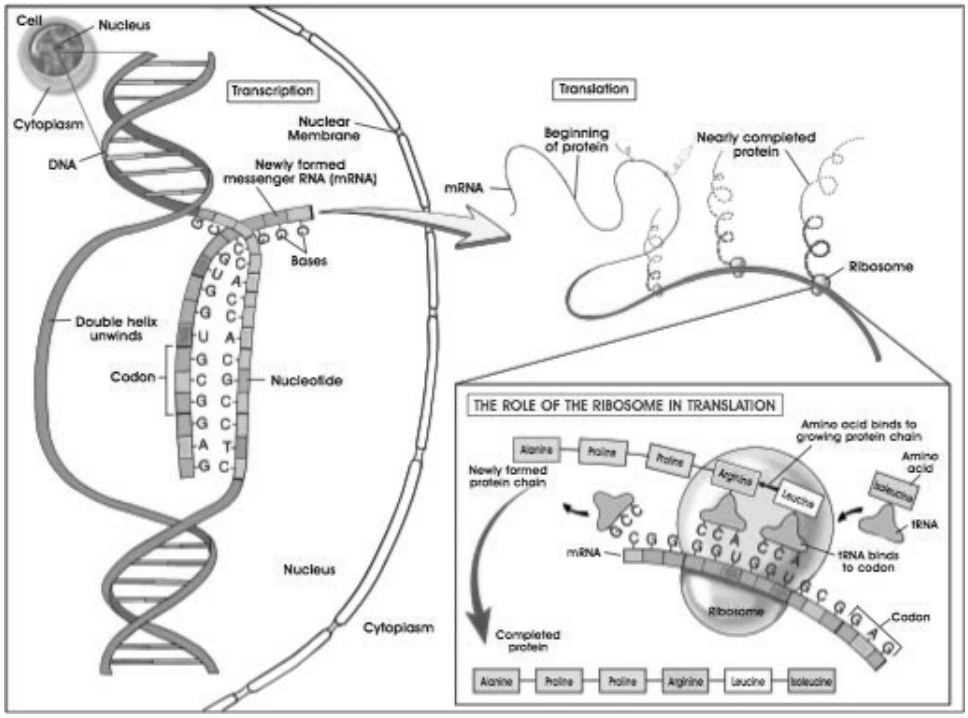

Figure 2.1: A representation of the complex mechanisms of the protein synthesis process (`www.stemcells.nih.gov`)

try or positron emission tomography (PET). PET is a nuclear medicine imaging technique which produces a three-dimensional image or map of functional processes in the body. The system of measure detects pairs of gamma rays emitted indirectly by a positron-emitting radionuclide, which is introduced into the body on a biologically active molecule (tracer). From the spatial-temporal registration of the tracer it is possible to quantify the physiological process associated in a specific location of the examined subject trough a computer analysis. The type of metabolic parameters that PET provides, depends on the type of tracer used during the PET study and on the mathematical method of data elaboration. Actually different kind of tracers and quantification methods exist, and this allows PET to be applied in different areas of medical care like oncology, cardiology,

psychiatry and neurology. In this work we also utilize a PET approach to measure our protein synthesis parameters of interest. In fact, even though different techniques to estimate the regional rate of protein synthesis had been developed, only the L-[1 $-^{11}C$]leucine PET method ([28]; [30]; [2]) allows to quantify it in human in vivo.

In this method the L-[1 $-^{11}$ C]leucine[3] is injected in the patient with a intravenous access. The radioactivity of the tracer in brain is then registered from the PET instrumentation. After this process the data are elaborated using a mathematical estimation algorithm that finally provides the quantification of the variables of interest. For the correctness of the results the role of the leucine is essential. Before the L-[1 $-^{11}$ C]leucine PET method, studies with others radiolabeled amino acid tracers were tried to measure rCPS but none of them provided quantitative results ([26]; [14]) as a consequence of the amino acid's recycling effects that the methods don't consider, unlike the leucine technique. If plasma is the only source of the amino acid in the tissue, the integrated specific activity of the precursor amino acid in the tissue can be estimated from the measured time course of the amino acid in arterial plasma and a compartmental model of the behavior of the amino acid in the tissue, but, it has been shown that, in brain, protein degradation in the tissue is also a significant source of amino acid ([31]; [29]). Even 60 minutes after a bolus injection of a radiolabeled amino acid, the sizeable pool of tissue protein is largely unlabeled and amino acids derived from the steady-state breakdown of unlabeled protein are constantly diluting the specific activity of the precursor amino acid coming from plasma. Studies in experimental animals have shown that this can result in a significant under-

[3]Leucine is an amino acid, normally involved in the human metabolism. By a chemical reaction one of the carbon atoms is substituted with ^{11}C and the L-[1 $-^{11}$ C]leucine is so produced. In this way we obtained a PET tracer that allows following the process involved in the leucine metabolism and so also the protein synthesis.

estimation of rCPS [31]. The L-[1 $-^{11}$ C]leucine PET method accounted for the effect of recycling for measurement of rCPS by including in the operational equation a factor, λ, which is the fraction of the precursor pool for protein synthesis derived from arterial plasma. The fraction derived from tissue proteolysis is then 1-λ [28]. Because the L-[1 $-^{11}$ C]leucine method accounts for the unlabeled leucine which is recycled from proteolysis, it provides a truly quantitative rate of protein synthesis. The L-[1 $-^{11}$ C]leucine PET method has been validated in non-human primates [30] and applied to humans [34]. The reproducibility and variability of measurements of λ and rCPS have been studied in normal subjects [2]. Recently studies have compared the differences of λ and rCPS in awake and propofol[4] anesthetized normal subjects. In the next sections we present the details of the L-[1 $-^{11}$ C]leucine PET method. To be clearer we distinguish two parts: the first one, which explains the whole process for data acquisition from the patients, and the second that is directly related to the quantification of λ and rCPS from the acquired data.

[4]Propofol is a short-acting intravenous sedative agent used for the induction of general anesthesia for adults and children, maintenance of general anesthesia, and sedation in medical contexts, such as intensive care unit (ICU) sedation for intubated, mechanically ventilated adults, and in procedures such as colonoscopy.

2.2 The acquisition of the data

In this section we present the whole process to obtain the data used for the quantification of metabolic parameters, from the choice of the subjects to the acquisition and elaboration of the PET images.
The data from the human subjects that we used in this work to evaluate the regional rate of cerebral protein synthesis were collected with a well-defined acquisition program [2]. This schedule, in fact, has to be very rigid to ensure the patient safety and certify the validity of the data obtained. The scheme of acquisition can be split in the following steps:

- The choice of the subjects
- The Brain MRI
- The L-[1 $-^{11}C$]leucine synthesis
- The PET studies
- The L-[1 $-^{11}C$]leucine blood sample analysis
- The PET data time courses

2.2.1 The choice of Subjects

Eighteen to 24 year old male volunteers were prospectively evaluated by clinical history, physical examination and a structured clinical interview which is designed to identify psychiatric diagnoses based on DSM-IV criteria [38]. The criteria to be suitable for the study were:

1. no current or past diagnoses of psychiatric, neurologic or chronic medical condition;
2. no history of neurologic trauma;

3. no family history of genetically transmissible neurologic syndrome;

4. HIV negative.

Subjects were excluded if they did not meet all inclusion criteria. Nine right handed subjects, in a range of 21-24 years old, were selected for the study. Each subject underwent two L-[$1-^{11}C$]leucine PET examinations and one non-contrast magnetic resonance scan (MRI) of the brain. The repetition of two PET studies was used to study the repeatability of the method [2] but for this work only the data acquired with the first examination has been used. The protocol was approved by the National Institutes of Health Combined Neuroscience Institutional Review Board and the National Institutes of Health Radiation Safety Committee. All subjects gave written informed consent prior to study enrollment.

2.2.2 Brain MRI

All subjects underwent a non-contrast T1 weighted MRI of the brain for region of interest (ROI) placement and to exclude structural brain abnormalities. MRI examinations were performed using a head coil on either a 1.5 Tesla Signa (GE Medical Systems, Milwaukee, WI), or a 3 Tesla unit (Phillips). Typical imaging parameters were: 3D fast spin gradient echo, echo time/repetition time: 9 ms/2 ms, 20 flip angle, 1 net excitation, in plane field of view (FOV): 240 mm, 256 x 256 matrix, 1 mm slice thickness without interleaved slices. Images were reconstructed to voxel dimensions of 0.94 x 0.94 x 1 to 1.3 mm, and interpolated to voxel dimensions of 0.94 mm^3. ROIs were placed on each MRI by visually identifying anatomic landmarks, and manually outlining the individual regions and whole brain. For some subjects some regions, in particular for the smallest

like the hypothalamus, a correct anatomical identification was impossible to do and so we avoided inclusion of this data in the quantification process.

2.2.3 L-[$1-^{11}C$]Leucine Synthesis

D,L-[$1-^{11}C$]Leucine was prepared from $H^{11}CN$ with a modified Strecker-Bucherer reaction [32]. Pure L-amino-acid was isolated from the racemic mixture by chiral HPLC with a Chirobiotic T column (10 x 250 mm) (Advanced Separation Technologies Inc., Whippany, NJ, USA), mobile phase of ethanol/water: 5/95 (V/V), and a flow rate of 3 ml/min. Retention times of the L- and D-isomers were approximately 7 and 8 min as determined by the corresponding standards. L-[$1-^{11}C$]leucine was obtained with a radiochemical purity of >99% and an estimated specific activity of 3 mCi/nmol.

2.2.4 PET Studies

Subjects were instructed to consume a high protein snack and then fast for eight hours prior to each PET study. On the morning of the study, arterial and intravenous lines were placed in the radial artery of the non-dominant hand and contralateral antecubital fossa, respectively. PET studies were performed on very high-performance PET instrumentation whose particularities will be examined in detail in the next section. Subjects were positioned in the scanner and a 3 min transmission scan was acquired for optimal subject positioning within the field of view (FOV). A 6 minute transmission scan was then obtained for attenuation correction. Ninety-minute dynamic emission scans were initiated coincident with the intravenous infusion of 20-30 mCi of L-[$1-^{11}C$]leucine administered over 2 minutes. Data were acquired in list mode and reconstructed using the motion-compensated 3D ordinary Poisson ordered subset expectation

maximum (OSEM) algorithm. 3D frames of data were reconstructed to 207 slices 1.23 mm thick. Each image was organized as 42 frames of data with the following time grid: 16 x 15 sec, 4 x 30 sec, 4 x 60 sec, 4 x 150 sec, 14 x 300 sec. With this schedule data were sampled frequently at the beginning of experiment when the tracer activity was changing rapidly and less frequently when the activity was changing more slowly. All activities were decay corrected to the time of radiotracer injection.

2.2.5 [^{11}C]Leucine Blood Sample Analysis

Arterial blood sampling was initiated concurrently with the start of the ^{11}Cleucine infusion to determine the time courses of the concentrations of unlabeled and labeled leucine in plasma and total ^{11}C and $^{11}CO_2$ activities in whole blood. Timed samples were hand drawn continuously ($\sim$ one sample/9-10 sec) for the first 4 minutes, and at increasing intervals thereafter for a total of $\sim$ 40 samples per study. The procedure apportioned blood samples as follows:

1. Approximately 0.2-0.3 mL of whole blood was transferred to a preweighed tube containing 1 N NaOH; the tube was immediately reweighed and counted in a gamma counter (Cobra II Auto Gamma, Packard Instrument CO., Inc., Downers Grove, IL, USA) to obtain total activity in whole blood.

2. Approximately 0.5 mL was centrifuged to remove red cells and 0.2 mL of plasma from each sample was diluted in distilled water and deproteinized at 4°C by the addition of a solution of 16% (W/V) sulfosalicylic acid containing L-norleucine (0.04 mmol/L) as an internal standard for amino acid analysis. Labeled and unlabeled leucine concentrations in the acid-soluble fraction were assayed by gamma

counting and fluorescence detection of post-column ortho-phthaldehyde derivatized amino acids separated with ion exchange HPLC (Agilent Technologies, Inc., Santa Clara, CA, USA and Pickering Laboratories Equipment, Mountain View, CA, USA), respectively.

3. Approximately 1 mL of whole blood was injected through the septum of a sealed vial into 2 ml of 8% sulfosalacylic acid. Attached to the septum of the vial was a polyethylene cup with a filter paper soaked with 1 N NaOH. The vial was weighed and, after allowing 30 min for the evolution of $^{11}CO_2$, the filter paper was removed and counted.

^{11}C activities in all samples were decay corrected to the time of injection.

2.2.6 PET Data time courses

For each study, a 3D volume was constructed from the average of the emission data acquired between 30 and 60 min. This volume was isotropically smoothed with a Gaussian filter (FWHM 3 mm) and aligned to the MRI volume by use of the Flexible Image Registration Toolbox (FLIRT) [12] with a 3D rigid body transformation. The resliced average 30-60 min PET image was visually reviewed for correct alignment with the MRI by use of Vinci software (Volume Imaging in Neurological Research, Co-Registration and ROIs Included, Max-Planck-Institute for Neurological Research, Cologne, Germany). The transformation parameters were then applied to each frame of the PET study (without prior smoothing) to effect their alignment with the MRI volume. ROIs drawn on MRIs were transferred to L-[$1-^{11}C$]leucine scans to compute regional tissue time-activity curves (TACs).

2.3 The PET instrumentation

The PET instrumentation, used to acquire the data of this work, consists of a high technological system projected for researcher studies. The system is particular for two reasons:

- *It uses a new generation brain PET tomograph*
- *It utilizes a new high performance method for the reconstruction of the images and their resolution recovery*

In this section we present the features of this instrumentation to understand the characteristics of the images provided by it.

2.3.1 The brain PET tomograph: the ECAT HRRT

The ECAT HRRT (High Resolution Research Tomograph) ([41]; [10]) is a dedicated brain and small animal PET scanner, with design features that enable high image spatial resolution combined with high sensitivity. The HRRT is the first commercially available scanner that utilizes a double layer of LSO/LYSO (lutetium-oxy-orthosilicate) crystals to achieve photon detection with depth-of-interaction information. This technology allows a reduction in crystal size and its short scintillation rise and decay time a short coincidence time window with a reduction of dead time.

The HRRT is built of eight panel detector heads arranged in an octagon with a head to head distance of 46.9 cm for opposing heads and 1.7 cm for neighboring heads. The gantry has a 35 cm diameter patient opening with an axially 25.2 cm long and transaxially 31.2 cm wide electronic FOV (Field of View). The HRRT is a Siemens PET scanner unique in its genre. In fact, if we compare it with the GE Advance[5] PET scanner (Figure 2.3)

[5]GE Advance PET scanner is the highest resolution PET system manufactured by GE

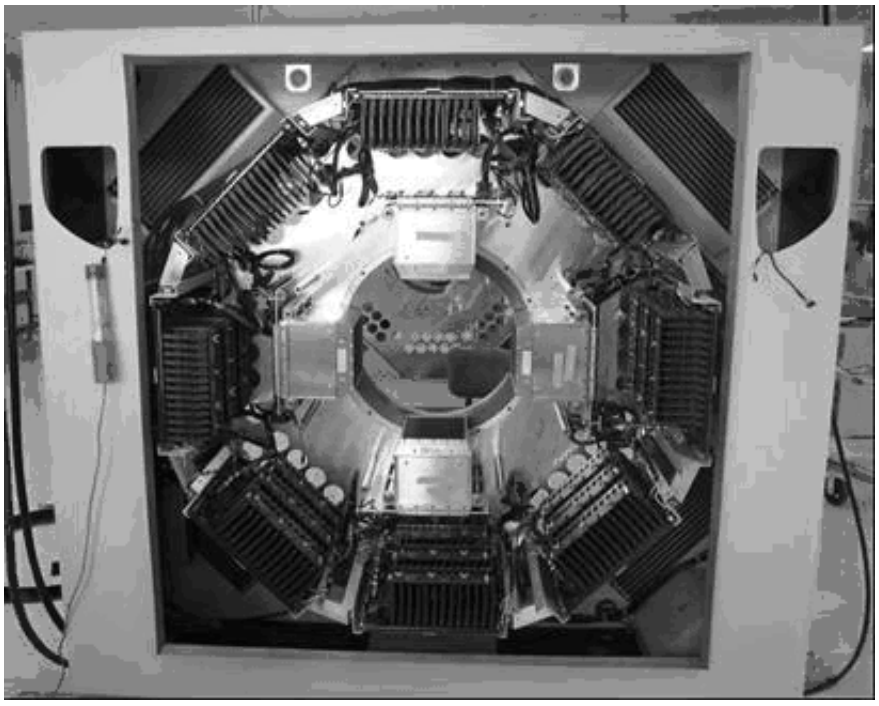

Figure 2.2: Front view of the ECAT HRRT scanner by CPS Innovations, Knoxville, TN. The topology of the HRRT is an octagon of dual-layer (LSO/LYSO) detector banks, each bank being an array of 9 x 13 blocks, and each block containing 8 x 8 crystals of size 2.1 x 2.1 x 10-mm each. With 119,808 crystals, the HRRT has 4.5 billion potential lines of response. The HRRT has a 35-cm patient port, making it suitable for human brain studies as well as large animal studies.

it is evident that the performance of the HRRT is better. HRRT has a smaller detection hole than the GE but it is at the same time sensitive at a huge number of Line of Response (LOR) per second. However, what is interesting for our data is the very high resolution that HRRT has. This resolution contributes to providing high quality brain images in which the volume of each voxel is very small. To understand better in what this difference of resolution consists we reported in Figure 2.4 the phantom scans in the two different tomographs. In the HRRT image,

Medical Systems. Unlike the HRRT it is characterized by a FOV sufficiently large to study not only the brain but all the human body.

Features	GE Advance (2D and 3D)	HRRT (3D Only)
Geometry	Circular (diam. 93 cm)	Octagonal (diam. 47 cm)
Structure	18 rings of 672 crystals per ring =12K	8 panels of 9x13 blocks 8x8x2 detectors = 120K
Number of LOR (Line Of Response) per second	25 Mega	4.5 Giga
Transverse 3D resolution	6-7 mm	2.5-3 mm
Axial 3D resolution	6-7 mm	2.5-3 mm

Figure 2.3: Comparison between GE Advance PET scanner and HRRT

we can see easily details of the phantom that are not present in GE one. But it is not only high-quality of the scanner to cause this difference. In fact, to arrive at these results, it is necessary to correct the data from all the errors that affect the acquisition protocol, like random coincidences and motion, and only after this the images can be reconstructed. For this reason, a very complete system to perform HRRT PET reconstruction has been developed and optimized.

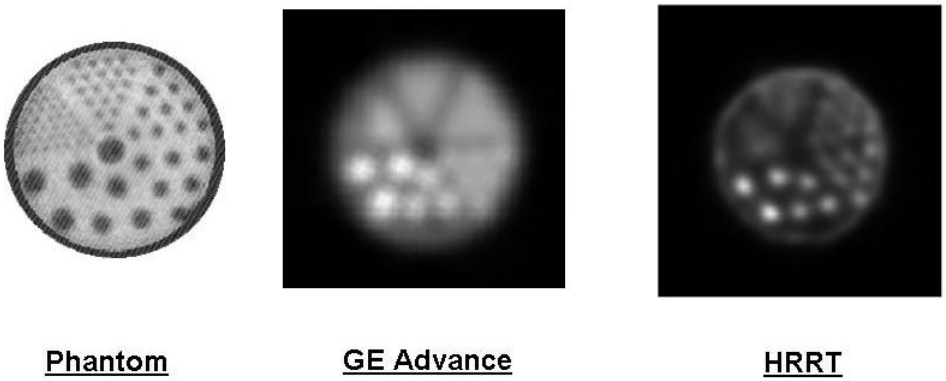

Figure 2.4: The different resolution between GE Advance PET scanner and HRRT in a phantom scan [10].

2.3.2 MOLAR: The Reconstruction Algorithm

The Motion-compensation OSEM[6] [11] List-mode Algorithm for Resolution-recovery Reconstruction (MOLAR) is a complete system for managing and performing iterative PET reconstructions. The system is the result of an ongoing collaboration between three organizations in the NIH Intramural Research Program as well as Yale University, SUNY Buffalo, and CPS Innovations, Knoxville, TN, USA. MOLAR has been designed for use with the ECAT HRRT (High Resolution Research Tomograph, CPS Innovations) operating in list-mode but this reconstruction engine is readily adaptable to any PET scanner. This system elaborates all the data acquired by PET scanner including the attenuation correction coefficient, randoms estimate, scatter estimate, number of events, crystal indices, motion-corrected event coordinates and region-of-support bound. The motion correction information is tracked and elaborated via the Polaris Optical Tracking System (Northern Digital Inc., Waterloo, Ontario, Canada). The system is very complex and requires a powerful computational engine for the information processing. This is made by a computer cluster of 46-nodes, each one with a double AMD processor. The typical reconstruction time for one frame is less than one hour. The MOLAR system applied to the HRRT provides images with resolution of less than 3 mm and data are corrected for attenuation, scatter and randoms. This characteristic influences in a positive way the quality of the time-activity curves associated with each voxel and so also the finally results of the quantification.

[6]Ordered Subsets Expectation Maximization reconstruction algorithm.

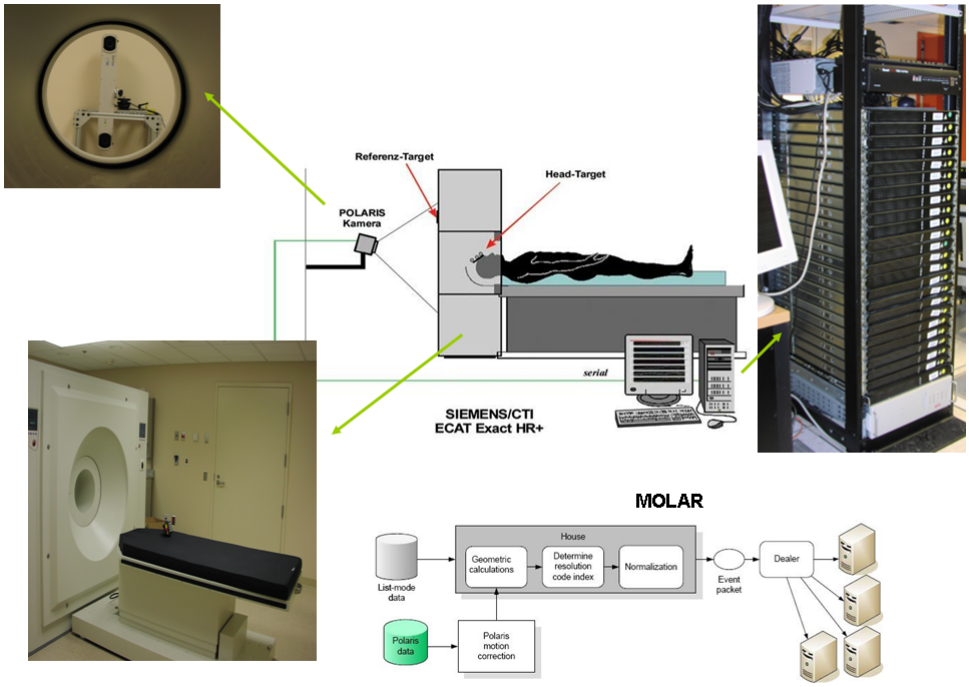

Figure 2.5: The MOLAR is not simply an algorithm but is a complex system that works interactively with the PET scanner to improve the quality of the reconstructed data.

Chapter 3

The compartmental approach

3.1 The kinetic model

After the acquisition and reconstruction of the L-[1 −11 C]leucine PET data, the acquired information is processed for the quantification of λ and rCPS. To do this, we identify the constants of a kinetic model from which the variables of interest are calculated. The features of this kinetic model and its capacity to describe the physiological leucine system are crucial for the goodness of the final results and for this importance we are going to present in this section its main characteristics.

3.1.1 The kinetic model of unlabeled leucine

To define the kinetic model for the L-[1 −11 C]leucine PET data it is necessary to analyze before the biochemical metabolism associated with unlabeled leucine. From the knowledge of the leucine metabolic system a comprehensive model of it can be represented in Figure 3.1 [31]. In this model C_p, C_e and C_m represent the concentration of free leucine in plasma, extracellular space and intracellular space respectively. C_{pp} and P represent the leucine in t-RNA complex and in cellular protein. The rate constants of the model are:

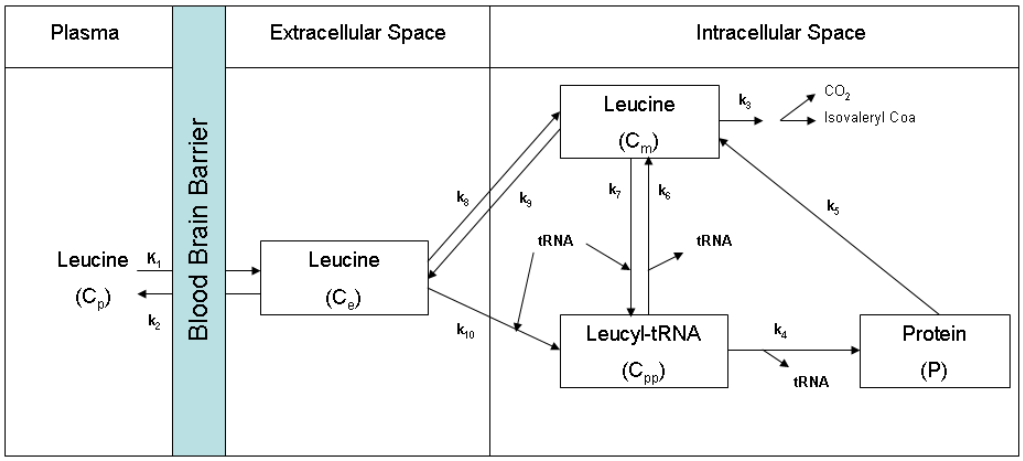

Figure 3.1: The unlabeled leucine kinetic model

- K_1, for carrier-mediated transport of leucine from plasma to tissue;
- k_2, for transport back from tissue to plasma;
- k_3, for catabolism of leucine;
- k_4, for leucine incorporation into protein;
- k_5, for release of free leucine by protein degradation;
- k_6, for deacylation of leucyl-tRNA;
- k_7, for transfer of leucine from the intracellular leucine pool to precursor;
- k_8, for transport of leucine from extracellular space to intracellular leucine pool;
- k_9, for transport of leucine from intracellular pool to extracellular space;
- k_{10}, for transport of leucine from extracellular space to intracellular pool for the protein synthesis.

It is clearly evident that this model can not be used directly for any estimation because it contains too many parameters, but it provides a complete description of the leucine distribution in the various brain compartments and their connections. For these reasons, this model can be very useful as starting point to define a model for L-[$1-^{11}C$]leucine from which the parameters can be estimated.

3.1.2 The Homogenous Kinetic Model for L-[$1-^{11}C$]-leucine

The model for the behavior of L-[$1-^{11}C$]leucine in brain (Figure 3.2) was semplified from the comprehensive model for leucine (Figure 3.1) [28]. It contains only four rate constants: K_1 and k_2 for carrier mediated transport from plasma to brain and back from brain to plasma, respectively; k_3 for metabolism of leucine to yield CO_2; and k_4 for incorporation of leucine into protein. The rate constants are identical for labeled and unlabeled leucine. To obtain this result the following assumptions are applied:

- The tissue region is homogenous with respect to concentrations of amino acids, rates of blood flow, and rates of transport, metabolism, and incorporation of amino acids into protein;

- The concentration of unlabeled leucine in arterial plasma and rates of amino-acid metabolism and protein synthesis are assumed constant during all the experiment period (steady state);

- Concentrations of labeled leucine are sufficiently small that the tracer theory holds, and there are no isotope effects associated with its use;

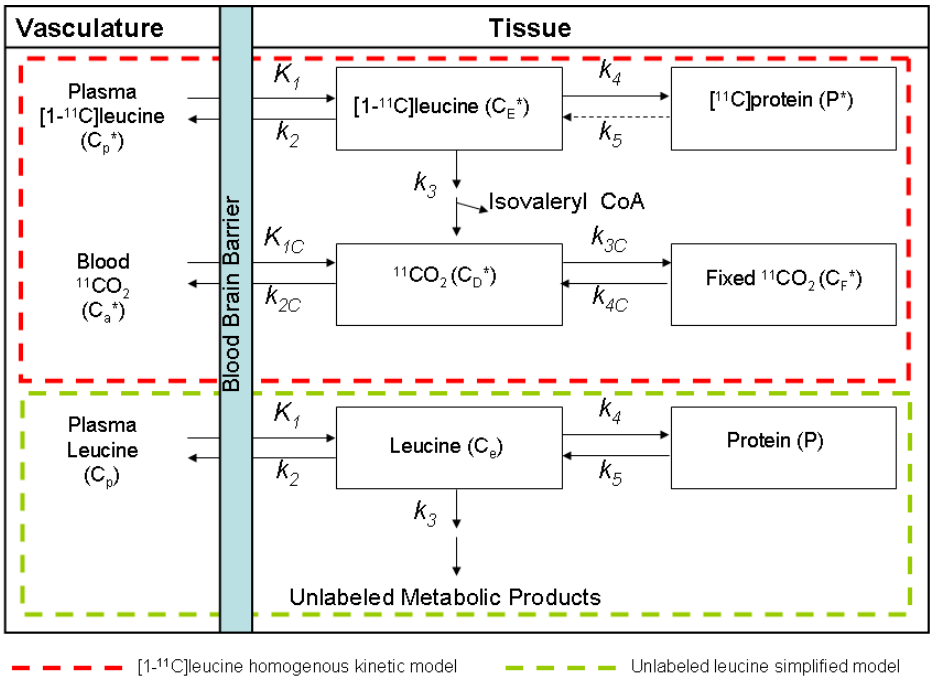

Figure 3.2: The L-[1 $-^{11}C$]leucine homogenous kinetic model (HOM) and the simplified model for the unlabelled leucine.

- The model does not distinguish intra and extracellular spaces, and pools of free leucine and tRNA-bound leucine are combined and represented by a single tissue pool;

- There is no significant loss of label and no recycling or L-[1 $-^{11}C$]leucine from breakdown of labeled protein.

This last hypothesis can be justified, in light of the long average half-life (>3 days) of brain protein [17] compared to the experimental time (90 minutes). For this reason, we know that the rate constant for breakdown of unlabeled tissue protein, k_5, is very small. In the case of unlabeled protein, k_5 acts on the large pool of brain protein producing a significant amount of unlabeled leucine in the tissue. In the case of labeled protein k_5 acts on the very small pool of labeled protein (P^*) produced during the study duration. We assume, therefore, that $k_5 P^* \sim 0$.

The total concentration of ^{11}C in the field of view of the PET camera (C_T^*) at time T includes free [^{11}C]leucine and [^{11}C]leucine incorporated into protein in the tissue (C_E^* and P^*, respectively) as well as activity in the blood in the brain ($V_b C_b^*$, where V_b is the fraction of the volume occupied by blood and C_b^* is the concentration of activity in whole blood). It also includes the labeled products of [^{11}C]leucine metabolism: $^{11}CO_2$, and products of $^{11}CO_2$ fixation. We assume negligible fixation of $^{11}CO_2$ during the experimental period [5], and that diffusible $^{11}CO_2$ in brain rapidly equilibrates with the arterial blood [5], i.e., its concentration can be approximated by $V_D C_c^*$, where C_c^* is the $^{11}CO_2$ activity in whole blood and V_D is the brain/blood equilibrium distribution volume of $^{11}CO_2$. Therefore

$$C_T^*(t) \simeq (1 - V_b)[C_E^*(t) + P^*(t) + V_D C_c^*(t)] + V_b C_b^*(t). \quad (3.1)$$

Time courses of C_c^*, C_b^*, and plasma ^{11}leucine concentration (C_p^*) are measured from arterial blood samples taken at the time of the PET study. For any set of rate constants, the time courses of C_E^* and P^* can be calculated from C_p^* by solving the differential equations corresponding to the compartmental model:

$$\begin{cases} \frac{dC_E^*}{dt} &= K_1 C_p^*(t) - (k_2 + k_3 + k_4) C_E^*(t) \\ \frac{dP^*}{dt} &= k_4 C_E^*(t) \end{cases} \quad (3.2)$$

In the model of Figure 3.2 also the behavior of the unlabeled leucine is described. The compartmental model defined the following equations

$$\begin{cases} \frac{dC_E}{dt} &= K_1 C_p(t) - (k_2 + k_3 + k_4) C_E(t) + K_5 P(t) \\ \frac{dP}{dt} &= k_4 C_E(t) - k_5 P(t) \end{cases} \quad (3.3)$$

in which the rate constants have the same meaning and the same value of the labeled leucine model. The hypothesis that the unlabeled leucine is in steady state in both exchangeable

pool and in protein can be expressed as

$$\frac{dC_E}{dt} = \frac{dP}{dt} = 0 \tag{3.4}$$

The fact that the labeled and unlabeled leucine have the same rate constants is justified by the equivalence of physiological behavior of the molecules (no isotope effects are present in the labeled leucine) and this feature is fundamental for the evaluation of rCPS. In fact, we will show in the next section, the rCPS is defined from the unlabeled leucine parameter model but we used the estimated parameters of the labeled leucine model to calculate it.

3.2 Parameter estimation of the homogenous kinetic model

In this section we show how the rate constants (K_1, $k_2 + k_3$, k_4, V_b) and the variables of interest (λ and rCPS) are estimated from the data and the homogeneous kinetic model (HOM).

3.2.1 Rate Constant Estimation

For each ROI, including whole brain, the rate constants (K_1, $k_2 + k_3$, k_4) and the blood volume (V_b) were estimated using a weighted, non-linear least-squares (NLLS) method to fit the model equation for total activity (Equation 3.1) to the measured [^{11}C]leucine activity in plasma, total ^{11}C and $^{11}CO_2$ activity in blood, and total activity in the ROI [2]. The equilibrium brain/blood distribution ratio for $^{11}CO_2$ was fixed at the value measured in rhesus monkeys (V_D=0.41; [30]), a value in agreement with the mean whole brain/plasma distribution volume determined from $^{11}CO_2$ studies in humans [4] (The blood/plasma equilibrium distribution ratio for $^{11}CO_2$ in human subjects is close to unity). Weights were inversely proportional to the standard deviation of the decay corrected activity in each frame of data. Assuming Poisson statistics, that the counts originate only in the region itself, and that there are no other noise effects such as randoms or deadtime, the standard deviation (SD) was modeled as:

$$SD(C_T(t_i)) = N\sqrt{\frac{e^{\gamma t_i} C_T(t_i)}{\Delta t_i}} \tag{3.5}$$

where γ is the decay constant for ^{11}C, t_i is the midpoint of Frame i, Δt_i is the length of Frame i, and N is a coefficient of proportionality (Demonstration of Equation 3.5 in Appendix A). The expression used for the representation of the error in the acquired data is directly correlated with the behavior of

the tracer in the tissues. Let us consider [^{11}C]Leucine uptake in brain (Figure 3.3). As we can see from the pictures the L-[$1-^{11}C$]leucine needs a period of time to move from the blood to tissues and, after a peak corresponding the maximum value, its activity decreases and then changes little with time. Comparing the two last pictures we note that the noise level increases. This aspect, due to the decay of ^{11}C, is directly related with the decreasing number of counts registered by the scanner and so with the low accuracy that the PET machine has for the last measures. For this reason in Equation 3.5 there is a term that refers to the decay of the tracer and the time of acquisition ($e^{\gamma t_i}$): a small number of counts corresponds to a high error in the measures.

It is important to understand why Equation 3.5 considers also the time interval of acquisition. The role of Δt_i reflects the number of the events detected in a period of time: the longer the acquisition time, the higher the number of counts detected for that sample. Consistent with this if the period of acquisition is small also the number of counts is low and so the noise in that sample will be higher. The law, defined in Equation 3.5, takes in account all these factors. In Figure 3.4 we can see the effects of Equation 3.5 in measured data. What is relevant to see is that the highest weights do not correspond to the data with highest values but to that with the best compromise between the quantity of tracer and time resolution. The least weighted data instead is at the beginning, when there is little tracer in the tissues or at the end when the tracer activity is low due to radioactivity decay. Before the estimation of the rate constants, it is fundamental to correct the data for the delay between the tracer arrival time in the brain and the arterial sampling site. For this reason, all the signals used in this work are in advance corrected from this phenomenon trough a fixed grid approach (Section 3.3).

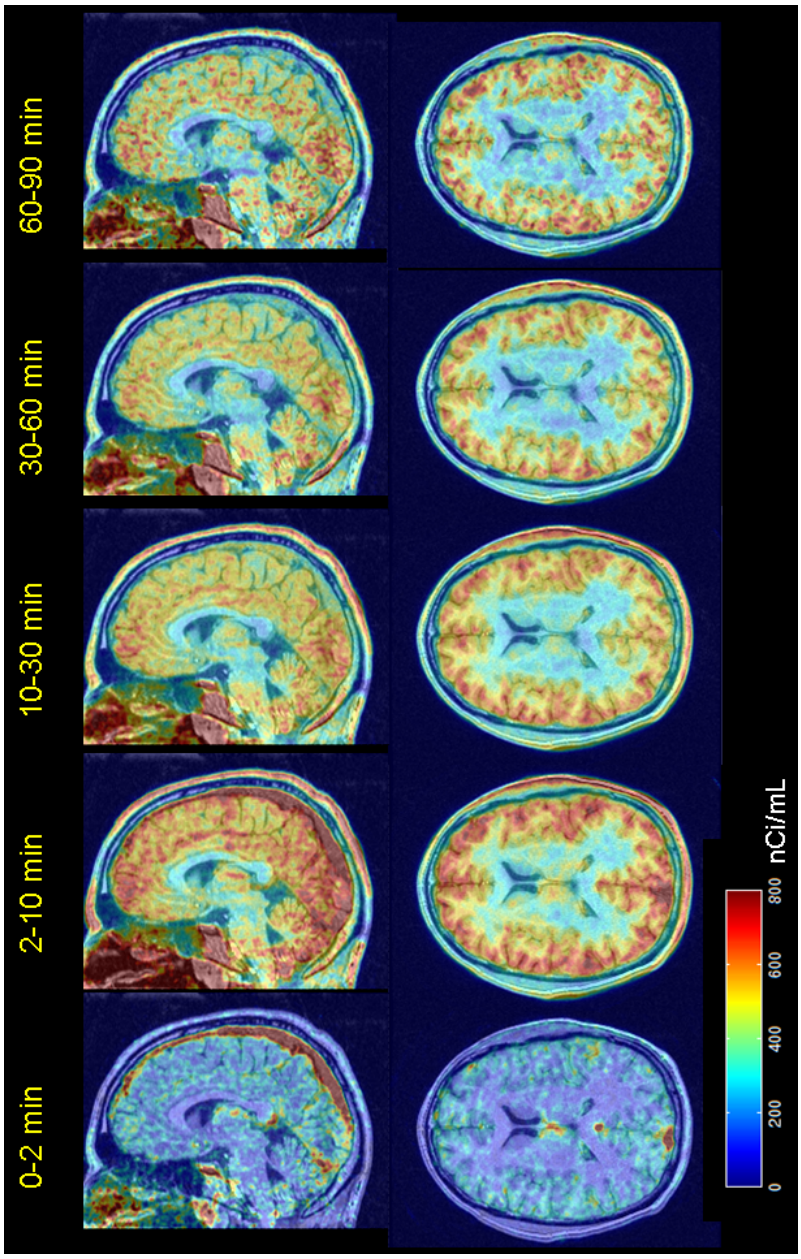

Figure 3.3: The behavior of the tracer decay-corrected in the tissues during the time. The images are the average of the signals in different intervals [0-2 mins; 2-10 mins; 10-30 mins; 30-60 mins; 60-90 mins]. At the beginning there is no tracer in the tissues but with the time it starts to arrive. At the end the concentration of L-[1 $-^{11}C$]leucine is stationary but we can see that the images are noisier due to the ^{11}C decay.

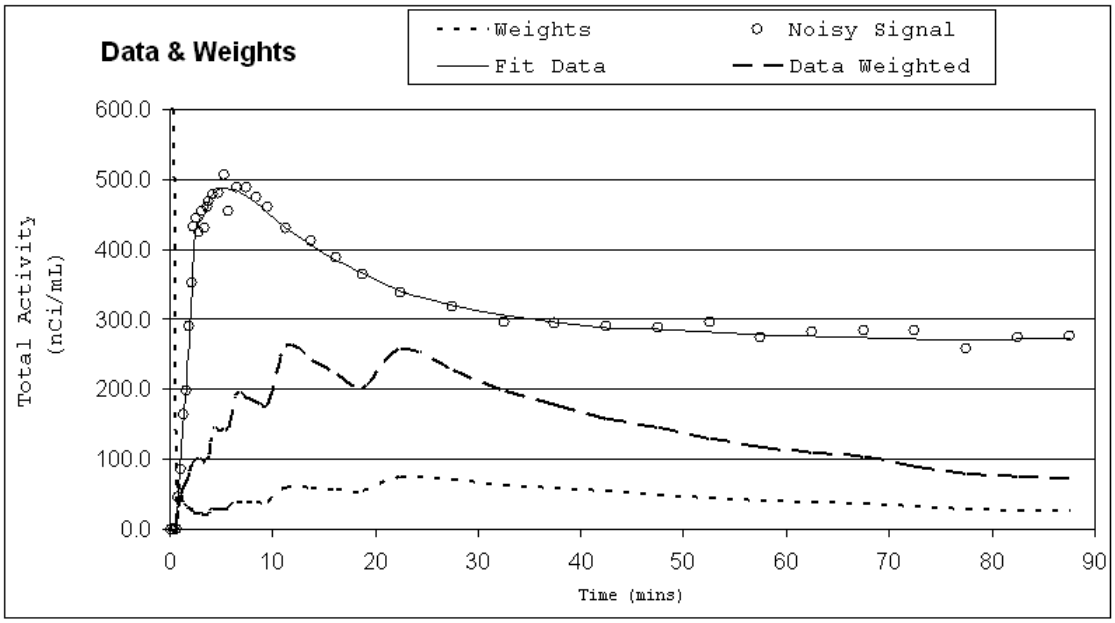

Figure 3.4: The data weighted.

3.2.2 rCPS and λ relationship with the HOM parameters

After the kinetic model parameter estimation rCPS can then be determined by the relationship

$$\text{rCPS} = \left(\frac{K_1 k_4}{k_2 + k_3} \right) C_p \tag{3.6}$$

where C_p is the plasma concentration of unlabeled leucine. This equation comes from the definition of the rCPS, the differential equations of HOM (Equations 3.3) and the assumption that unlabeled leucine, in both exchangeable pool and in protein, is in a steady-state. (In Appendix B all the mathematical passages to justify Equation 3.6 are reported and explained).
λ, the fraction of leucine in the precursor pool for protein synthesis derived from arterial plasma, can be also expressed in

terms of the rate constants. The formulation of λ is

$$\lambda = \frac{k_2 + k_3}{k_2 + k_3 + k_4} \tag{3.7}$$

(A complete demonstration, from where this expression comes, is reported in [28]) In terms of K_{Patlak}, the net uptake rate constant for [^{11}C]leucine, rCPS can also be expressed as

$$\text{rCPS} = \left(\frac{K_1 k_4}{k_2 + k_3 + k_4}\right)\frac{C_p}{\lambda} = K_{Patlak}\frac{C_p}{\lambda} \tag{3.8}$$

While rCPS may be directly calculated from Equation 3.6, the importance of λ arises from its physiologic relevance. Without knowledge of λ, it is not possible to distinguish whether changes in rCPS between states/conditions are primary effects or are secondary to changes in recycling of leucine from tissue proteolysis, or some combination of the two processes. This was originally elucidated in the development the L-[$1-^{14}C$]leucine autoradiographic method. The high accuracy of estimates of λ using the L-[$1-^{11}C$]leucine PET method were confirmed in validation experiments in monkeys [30]. The role of λ becomes fundamental if we want calculate rCPS with approaches that do not have access to the rate constants. In those cases the only expression to quantify rCPS is through the estimation of λ. Some of the algorithms that we will use in this work will meet this condition.

3.3 The Delay estimation

In this section we explain how we corrected the data from the presence of delay in the arterial input function.

3.3.1 The delay correction with a grid approach

The presence of this delay, due to a comprehensive difference between the tracer arrival in the brain and the arterial sampling site, can greatly influence the goodness of estimates if not taken into account. For this reason, before appling every kind of quantification technique, it is necessary to correct the data for its presence. To do this, we shifted the blood curves in a range of values and, fitting the whole brain time-activity curve with a chosen model[1], we selected the delay time that produced the best fit of the data. Weighted Residual Sum of Squares (WRSS) was used as selection index. The range of possible delays defined a grid from 0 to 20 seconds with an interval of 1 second.

This approach for the correction is affected by a limit: the shift of the signal for the delay correction reduces the length of the blood signals and this could be problematic for the parameter estimation. In fact, it is easier to process signals with the same length than signals with different timeline. To resolve the problem we applied the delay correction maintaining the original length of all the blood curves simply by repeating the last sample.

Tracer appearance times in various parts of the brain differ from the mean of the brain as a whole by ± 2 seconds [15]. For this reason, in each study the whole brain tracer arrival delay value was used for all regions. We reported in the Table 3.1 the

[1]This approach that we have used for the arterial delay correction requires a model for the representation of the system to which the data refers. It is not completely clear if the choice of model affects the estimation of the delay. At the moment, for our analysis the homogenous kinetic model (Section 3.1) is used.

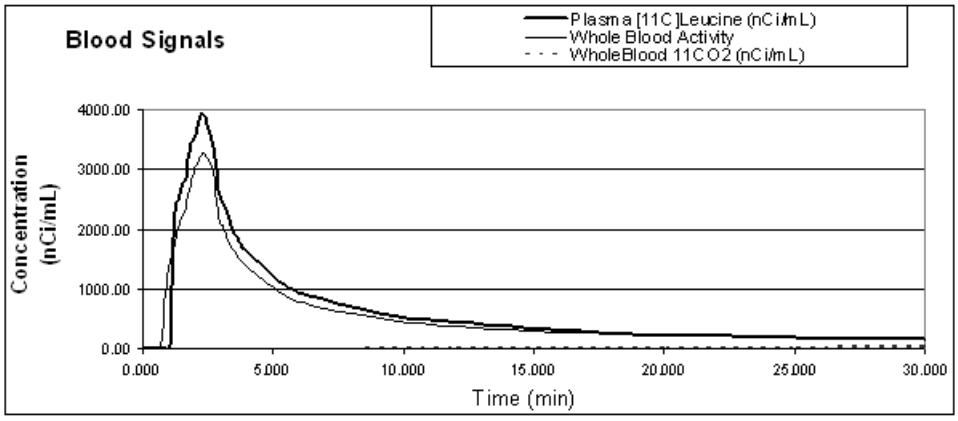

Figure 3.5: Typical blood signals measured during the PET acquisition.

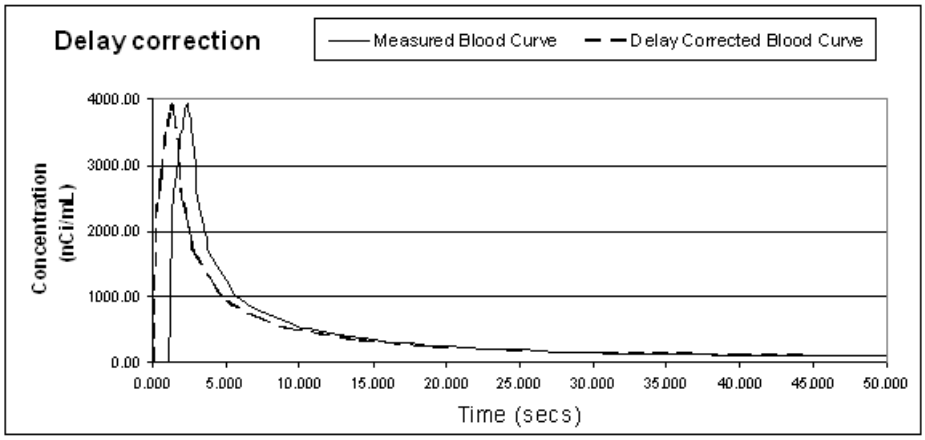

Figure 3.6: In this figure we report two blood signals, one delay corrected (continuos line) and one delay uncorrected (dash line).

Subject	**Estimated Delay (sec)**
1	14
2	5
3	4
4	1
5	5
6	11
7	14
8	9
9	13

Table 3.1: In this table we report the estimates of the delay for the 9 subjects. The evaluation is based on homogenous kinetic model.

delay values estimated from the subjects considered in this work. This method for the delay estimation has been used other times in this work with different modeling approaches. The purpose is to understand if this delay estimation is affected by the choice of kinetic model (Section 5.2).

3.4 The results of NLLS applied to HOM

In Figure 3.7 we report the results of the estimation for K_1, V_b, λ and rCPS in different ROIs. Each value is the average of the 9 subjects that we considered in this study where the Standard Deviation (SD) represents the intersubject variability of the estimates. Looking through the different regions, we can observe that the values of λ are quite similar, but rCPS that changes among the different ROIs[2], we cannot, however, have any information about the goodness of the estimates. In fact, they cannot be compared with anything else because the data that we used are experimental data and we don't know a priori the values of the variables that we estimated with this method. However we know that this technique has been validated [28] and at the moment the goal is to estimate rCPS and λ from L-[1 $-^{11}$ C]leucine PET data.

As an empiric method to understand the capacity of HOM to describe L-[1 $-^{11}$ C]leucine data we can compare time-activity curves with the description provide by the model. In Figure 3.8 there are some examples in different ROIs of one of our subjects. The graphs show that the fit is not completely good: the data are underestimated (from 25 to 50 minutes) or overestimated (from 60 to 90 minutes) in all the cases. This behavior is typical of the homogenous kinetic model and characterizes all the studied regions. To give an idea about the different accuracy in the estimates we report in Figure 3.9 the volumes of the ROIs. From the volume information we can understand the size of the region and so the noise level associated to it. In fact if the ROI is very small, like the hypothalamus, the noise in the ROI time-activity curve is high. Conversely, if the region is large, through the average the time-activity curve results are very smooth. This

[2]This information will be useful when we will discuss other kind of compartmental model for the [^{11}C]leucine system.

ROI	K1	Vb	λ	rCPS
	(mL/g per min)	--	--	*(nmol/g per min)*
Cerebellum	0.062 ± 0.007	0.082 ± 0.012	0.75 ± 0.03	2.19 ± 0.12
Vermis	0.060 ± 0.007	0.059 ± 0.012	0.74 ± 0.04	2.16 ± 0.12
Frontal	0.048 ± 0.005	0.068 ± 0.008	0.70 ± 0.03	2.13 ± 0.13
Temporal	0.042 ± 0.004	0.063 ± 0.011	0.69 ± 0.03	1.99 ± 0.13
Occipital	0.058 ± 0.005	0.072 ± 0.013	0.73 ± 0.04	2.25 ± 0.20
Parietal	0.049 ± 0.005	0.069 ± 0.010	0.71 ± 0.03	2.12 ± 0.19
SupraorbitalGyrus	0.045 ± 0.004	0.070 ± 0.012	0.70 ± 0.04	2.00 ± 0.14
PreCentralGyrus	0.050 ± 0.006	0.061 ± 0.011	0.72 ± 0.03	2.16 ± 0.21
PostCentralGyrus	0.052 ± 0.005	0.057 ± 0.008	0.73 ± 0.03	2.12 ± 0.17
Thalamus	0.046 ± 0.003	0.067 ± 0.014	0.74 ± 0.03	1.67 ± 0.10
Putamen	0.047 ± 0.006	0.055 ± 0.006	0.78 ± 0.02	1.43 ± 0.10
Caudate	0.032 ± 0.004	0.048 ± 0.007	0.74 ± 0.02	1.15 ± 0.10
Hippocampus	0.032 ± 0.004	0.087 ± 0.014	0.65 ± 0.04	1.82 ± 0.14
Amygdala	0.029 ± 0.002	0.065 ± 0.014	0.65 ± 0.03	1.63 ± 0.12
Hypothalamus	0.038 ± 0.005	0.053 ± 0.009	0.74 ± 0.03	1.37 ± 0.21
CoronaRadiata	0.025 ± 0.006	0.035 ± 0.004	0.73 ± 0.03	0.97 ± 0.07

Figure 3.7: NLLS applied to Homogenous kinetic model estimates. Results are means ± SD for 9 subjects.

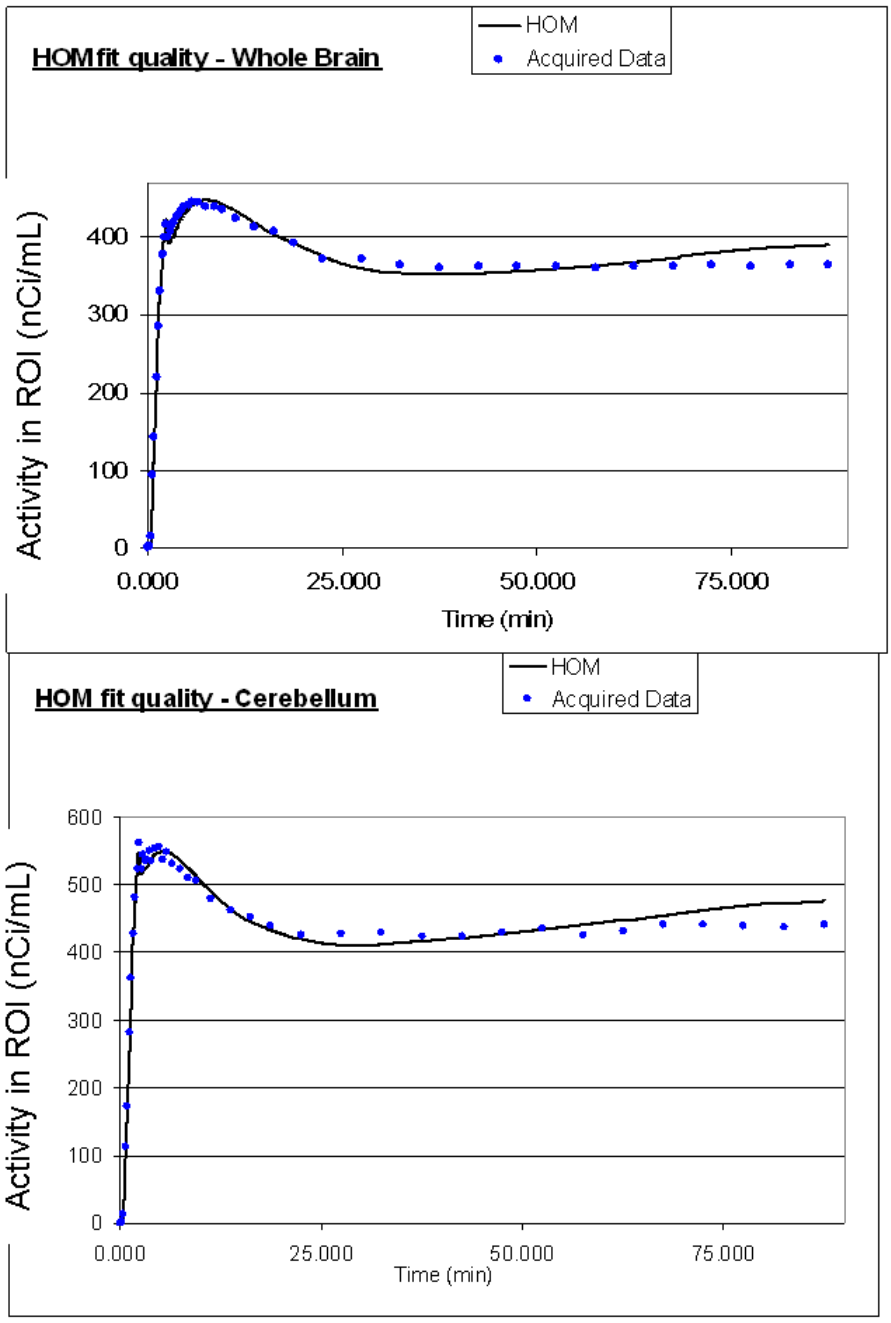

Figure 3.8: Model fit and measured data in two different ROI: whole Brain and cerebellum. As we can see in all the graphs the behavior of the curves referred to the model underestimate the data from 25 to 50 minutes and overestimate the data at the end of the experiment time (around 60 to 90 minutes).

ROI	Volume (cc)	ROI	Volume (cc)
Cerebellum	116.4 ± 15	PostCentralGyrus	1.7 ± 0.3
Vermis	5.7 ± 1.3	Thalamus	15.4 ± 0.7
Frontal	114.6 ± 24.6	Putamen	8.8 ± 1.2
Temporal	59.2 ± 10.9	Caudate	8.2 ± 1.0
Occipital	30.5 ± 8.4	Hippocampus	4.2 ± 1.3
Parietal	16.4 ± 4.4	Amygdala	4.6 ± 0.7
SupraorbitalGyrus	4.1 ± 1.1	Hypothalamus	0.5 ± 0.2
PreCentralGyrus	2.6 ± 0.4	CoronaRadiata	45.5 ± 4.5

Figure 3.9: ROI volumes. Each number is the mean ± SD for 9 subjects.

information may in part justify why for regions very small like hypothalamus or the postcentralgyrus the averaged estimates present a SD very high compared with the other ROIs.

3.5 The problem of the HOM: the tissue heterogeneity

3.5.1 The reasons of the poor fit

In light of the results shown in the previous section we can say that the homogenous kinetic model is characterized by some defects and so it may not be completely reliable for the rCPS quantification. Probably the causes of these are related to some hypotheses that are not completely satisfied. In fact, the assumption of tissue homogeneity may not always be a good approximation for a given region. Rates of blood flow, transport, metabolism, and incorporation of amino acids into protein, and therefore also the values of rate constants for each of these processes, vary regionally throughout the brain and are particularly different in gray and white matter tissue. Due to the limited spatial resolution of even the high resolution PET scanner ($\sim$ 2.6 mm FWHM), the thinness of the cerebral cortex ($\sim$ 3-4 mm), and the white matter tracts that course through subcortical areas, it is likely that activity measured in most ROIs, and possibly also in many voxels, derives from a heterogeneous mixture of gray and white matter.

3.5.2 The heterogeneous model

We, therefore, consider a new model, which we will refer to as the heterogeneous tissue model (HET) (Figure 3.10), that assumes that each tissue is composed of two homogenous subregions, e.g., gray and white matter. The activity in the tissue as a whole can be expressed as convex linear combination of the activity in its subregions (a and b), so that the total activity in the volume is

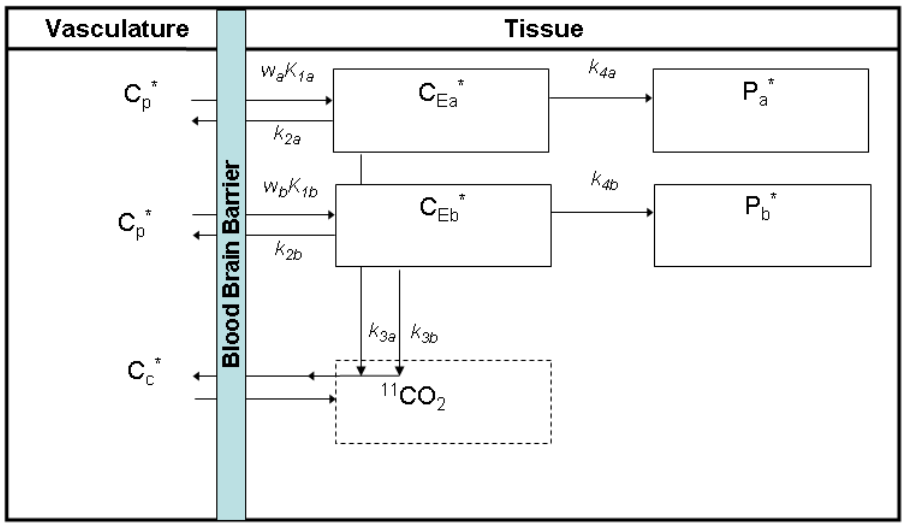

Figure 3.10: Compartmental representation for the heterogeneous kinetic model (HET).

given by

$$\begin{aligned} C_T^*(t) &\simeq (1-V_b)[w_a(C_{Ea}^*(t)+P_a^*(t))+w_b(C_{Eb}^*(t)+P_b^*(t))+ \\ &+ V_D(t)C_c^*(t)] + V_bC_b^*(t) \end{aligned} \tag{3.9}$$

with

$$w_a \geq 0, w_b \geq 0 \text{ and } w_a + w_b = 1 \tag{3.10}$$

where V_b is the fraction of the region's volume occupied by blood and w_i is the fraction of the region's volume occupied by the tissue i. If subregions a and b are characterized by the parameter sets $[K_{1a}, (k_{2a}+k_{3a}), k_{4a}]$ and $[K_{1b}, (k_{2b}+k_{3b}), k_{4b}]$, respectively,

then

$$\begin{aligned} C_T^*(t,\rho) &= (1-V_b)[\tfrac{w_aK_{1a}(k_{2a}+k_{3a})}{k_{2a}+k_{3a}+k_{4a}} \int_0^t C_p^*(\tau)e^{-(k_{2a}+k_{3a}+k_{4a})(t-\tau)}d\tau \\ &+ \left(\tfrac{w_bK_{1b}(k_{2b}+k_{3b})}{k_{2b}+k_{3b}+k_{4b}}\right) \int_0^t C_p^*(\tau)e^{-(k_{2b}+k_{3b}+k_{4b})(t-\tau)}d\tau \\ &+ \left(\tfrac{w_aK_{1a}k_{4a}}{k_{2a}+k_{3a}+k_{4a}} + \tfrac{w_bK_{1b}k_{4b}}{k_{2b}+k_{3b}+k_{4b}}\right) \int_0^t C_p^*(\tau)d\tau \\ &+ V_DC_c^*(t)] \\ &+ V_bC_b^*(t). \end{aligned} \tag{3.11}$$

For this model the parameter vector $\rho = [w_aK_{1a},\ w_bK_{1b},\ k_{2a} + k_{3a},\ k_{2b} + k_{3b}, k_{4a}, k_{4b}\ ,\ V_b]$. From Equation 3.11, it is clear that only six parameters can be estimated with this model - three coefficients of the integrals, two exponents, and V_b. (Recall that V_D is assumed to be known *a priori*). The single constraint that $\lambda_a = \lambda_b$, motivated by the observation that regional variation in λ is small [2], was made to allow the seven (non-independent) parameters to be estimated. Low regional variation in λ is also seen in our data (Figure 3.7). Weighted average rCPS in the region can be calculated as

$$\text{rCPS} = K_{Patlak}\frac{C_p}{\lambda} = \left(\frac{w_aK_{1a}k_{4a}}{k_{2a}+k_{3a}+k_{4a}} + \frac{w_bK_{1b}k_{4b}}{k_{2b}+k_{3b}+k_{4b}}\right)\frac{C_p}{\lambda} \tag{3.12}$$

where K_{Patlak} is the net uptake rate constant for [^{11}C]leucine. The fraction of unlabeled leucine in the precursor pool for protein synthesis derived instead from arterial plasma as

$$\lambda = \frac{k_{2a}+k_{3a}}{k_{2a}+k_{3a}+k_{4a}} = \frac{k_{2b}+k_{3b}}{k_{2b}+k_{3b}+k_{4b}} \tag{3.13}$$

The weighted average influx rate constant for the mixed tissue, K_1, can also be determined as $w_aK_{1a}+w_bK_{1b}$, but weighted aver-

ages of the rate constants k_2+k_3 and k_4 are not identifiable from the estimated parameters since the weights w_a and w_b are not known. To estimate the rate constants and thus other variables of interest from the HET, the same NLLS algorithm with the same weight data law was used. Possibly due to the large number of parameteres with HET, however, NLLS did not always converge. In fact, the NLLS applied to the heterogeneous model provides different estimates depending of the initial conditions with which the algorithm is set up and so we obtained different estimates for different starting points. Even trying different set up conditions the presence of a large number of parameters produces solutions with the same fit of the data but very different from each other and no criterion can be used to decide which estimate has to be selected as the true solution. In light of this we cannot be sure of the results provide with the NLLS applied to the HET: whether they are the true solution for the estimation, the consequences of convergence to local minimum or a wrong combinations of parameters that provide a good fit with the data.

To overcome the limits of the homogenous kinetic model and to have a corrected instrument for the quantification of rCPS from L-[1 $-^{11}$ C]leucine PET data, a new method is necessary. Our goal is an algorithm that is able to describe the leucine physiology and at the same time to consider the tissue heterogeneity. The next chapters will refer to this attempt.

Chapter 4

The Spectral Analysis

4.1 Definition of Spectral Analysis

In this section we define the principles of Spectral Analysis in order to analyze and quantify PET data. This approach represents an alternative and potentially better method for the quantification of rCPS.

Spectral Analysis (SA) is an input-output model to identify kinetic components of the tissue tracer activity without specific model assumptions, like the presence or absence of homogeneity in the tissue. This technique was introduced by Cunningham and Jones in 1993 [8] in order to determinate local metabolic rate of glucose in the brain [36], but now SA is commonly used with various PET tracers to study physiological systems other than brain e.g. liver, heart, kidneys, etc ... ([21]; [20]; [19]).

In SA, the measure of the radioactivity in the tissue at the time t, $C_{tiss}(t)$, is modeled as a convolution of the plasma activity curve $C_p(t)$ with a sum of $M+1$ distinct exponential terms:

$$C_{tiss}(t) = \sum_{j=0}^{M} C_p(t) \otimes \alpha_j \cdot e^{-\beta_j t} \tag{4.1}$$

i.e.

$$C_{tiss}(t) = \sum_{j=0}^{M} \alpha_j \cdot \int_0^t C_p(\tau) e^{-\beta_j (t-\tau)} d\tau \tag{4.2}$$

where α_j and β_j ($\beta_1 < \beta_2 < ... < \beta_{M+1}$) are assumed positive or zero. This constraint derives from the assumption that the SA is modeling a first order compartmental system. The upper limit, $M+1$, represents the maximun numbers of terms to be included in the model and this is, in general, set to a large number to be established, usually 100. The values of β_j are predetermined and fixed in order to cover an appropriate spectral range. For the studies in vivo involving short lived positron emitting isotopes this range needs to extend to the slowest possible event of the tracer in the tissue up to a value appropriate to transient phenomena (e.g. the passage of activity through the tissue vasculature).

In general the corresponding term for $\lim \beta_j \to \infty$ (i.e. β_j with a very large value) is proportional to $C_p(t)$ via α_j, and can be seen as a "high-frequency"component. In the same way the corresponding term with a $\beta_j = 0$ or very close is proportional to $\int Cp$ via α_j and can be viewed as a "low-frequency"component, i.e., accounting for trapping of the tracer. Lastly, the components corresponding to the intermediate values β_j (intermediate frequency components) will reflect the uptake of the tracer within the tissue with their number corresponding to the number of identificable tissue compartments within the ROI exchanging with plasma. This number is very important because it gives an indication of tissue heterogeneity. In light of these particular features is very common to define SA model equation explicitly showing the trapping in the following way

$$C_{tiss}(t) = \alpha_0 \cdot \int_0^t C_(\tau) d\tau + \sum_{j=1}^{M} \alpha_j \cdot \int_0^t C_p(\tau) e^{-\beta_j (t-\tau)} d\tau \tag{4.3}$$

To implement the SA model the first step is to define a grid of β_j. The range of the β_j, $j = 1, 2, , M$ can be chosen in different ways, using, e.g., a uniform or logarithmic distribution of values. In general the "traditional"SA grid follows the Di-Stefano distribution [18] used for the first time in SA with the [^{18}F]Fluorodeoxyglucose PET data [36]. The lower limit of this distribution is defined as $\beta_1 = (1/3T_{end})$ where T_{end} is the end time of the experiment. The upper limit is provided by $\beta_M = (3/T_{in})$ where T_{in} is the duration of the first scan (for our specific case 15 sec). The spacing of the β_j is fixed as

$$\beta_j = \frac{1}{T_j} \tag{4.4}$$

and

$$T_j = T_{j-1} \cdot \left(\frac{T_{end}}{T_{in}}\right)^{\frac{1}{M-1}} \tag{4.5}$$

with $j = 1, 2, , M$ and $M = 100$. The $M + 1$ unknown values of the various kinetic components α_j are estimated via nonnegative linear weighted least squares algorithm. For our study this operation has been done using the *lsqnonneg.m* function included in Matlab®(*Copyright 1984-2008, the MathWorks, Inc*). The computational time is higher than a linear estimation but the method is still very fast compared to a non linear approach. The result of the estimation is called "spectrum"and is represented in Figure 4.1. In the estimation of the spectrum it is possible to use a weighted data approach. The choice of the weights depends on the specific features of analyzed data and not on the estimation algorithm itself.
The precision of α_j is determined from the inverse of the Fisher Information matrix [1] which, from the Cramer-Rao Theorem, gives a lower bound on the standard deviation (Cramer-Rao Theorem in [6]).

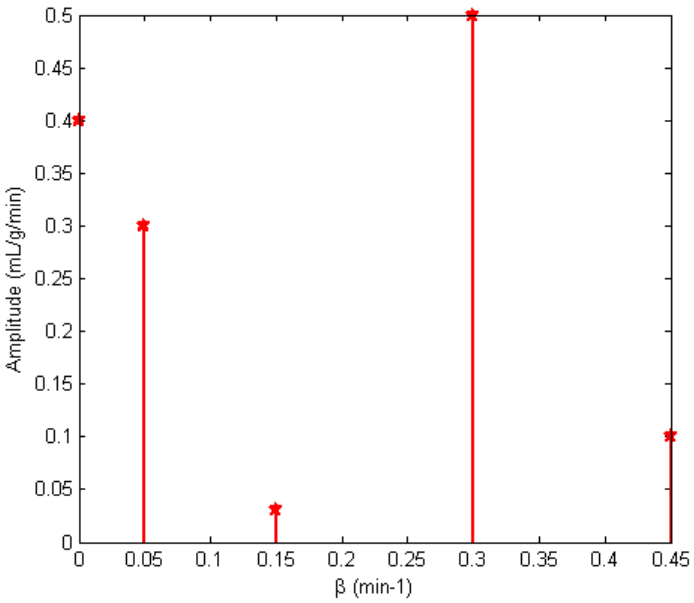

Figure 4.1: Example of a possible SA spectrum.

4.2 The equivalence with to compartmental models

The standard approach for the modeling PET tracers is based on compartmental models. Spectral Analysis seems to be a completely alternative method to this formulation, but this is not true. The idea behind SA, used by Cunningham in its definition, was to represent with this new formulation a "generic"compartmental model and for this reason there is a very strong correlation between the two techniques. The purpose of this section is to show this link.

4.2.1 From the compartmental model to the equivalent spectrum

To show the relation between the various compartment models and the SA spectrum we introduce some examples. This approach for the explanation is a less formal to desribe the equivalences between the equations of SA and the equations of the generic compartmental model, but is simpler and faster. To further simplify the equations we initially exclude V_b (the fraction of the volume occupied by blood) and C_b (concentration of activity in whole blood) from the model equation. Given our interest in PET we also adopt the typical conventions of the tracer, e.g., the initial concentration in the tissue equals to zero.

First example: a one tissue compartmental model (Figure 4.2A)

In this model, K_1 and k_2 denote the unidirectional clearance of tracer from blood to tissue and the rate constant for the transfer of tracer from tissue to blood, respectively. The equations of the model are

$$\begin{cases} \frac{C_1(t)}{dt} &= K_1 C_p(t) - k_2 C_1(t) \\ y(t) &= C_1(t) \end{cases} \tag{4.6}$$

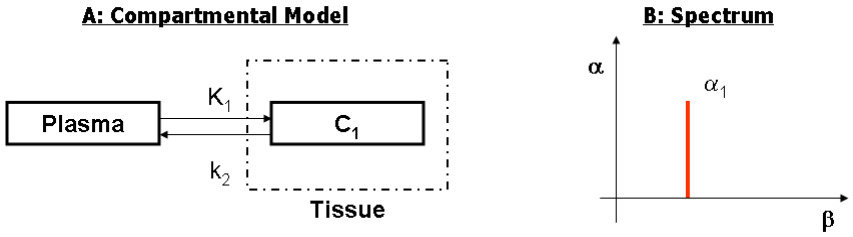

Figure 4.2: (A) One-Compartmental model and (B) its relative spectrum

Solving the differential system we obtain

$$y(t) = K_1 \int_0^t C_p(\tau) \cdot e^{-k_2(t-\tau)} d\tau \tag{4.7}$$

The SA solution equivalent to the compartmental model defines a spectrum with only one component (Figure 4.2B). The equation related at this spectrum is

$$y(t) = \alpha_1 \int_0^t C_p(\tau) \cdot e^{-\beta(t-\tau)} d\tau \tag{4.8}$$

that equals to Equation 4.7 in which K_1 is α and k_2 is β. If there is no transfer of the tracer from the tissue of the blood, i.e. $k_2 = 0$, the solution of the model is provided simply by the equation

$$y(t) = K_1 \int_0^t C_p(\tau) d\tau \tag{4.9}$$

equivalent to the SA equation

$$y(t) = \alpha_1 \int_0^t C_p(\tau) d\tau \tag{4.10}$$

This is the typical when in the model a trapping compartment is present (Figure 4.3). The associated spectrum is still defined by only one component but the line is located at $\beta = 0$. At this point of the work, it is useful to introduce some terminology, very common in SA works: when the component is located at

$\beta = 0$ it is called trapping component to indicate the equivalent trapping compartment; when the component refers instead for a $\beta \neq 0$ it is called equilibrating component and it is related to a reversible compartment.

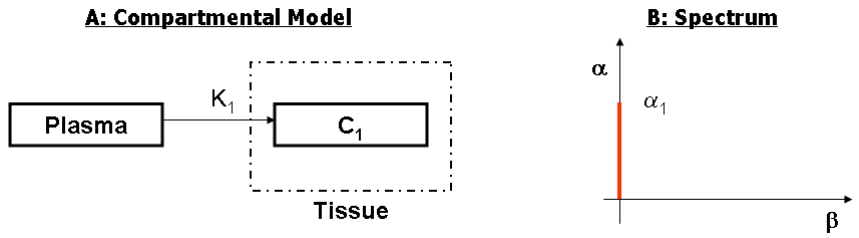

Figure 4.3: (A) Compartmental model with trapping and (B) its relative spectrum

Second example: a two-compartmental model (Figure 4.4A)

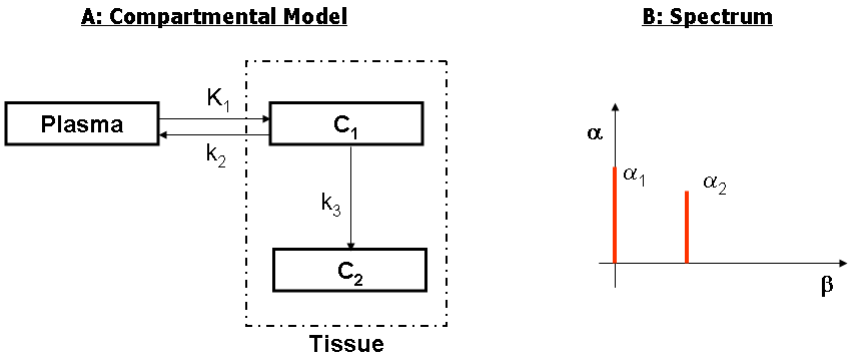

Figure 4.4: (A) Two-Compartmental model with trapping and (B) its relative spectrum

This example is very interesting because it is equivalent to the homogeneous tissue model for leucine (without the CO_2 compartment). With some renumbering the equations of the model

are

$$\begin{cases} \frac{C_1(t)}{dt} &= K_1 C_p(t) - (k_2 + k_3) C_1(t) \\ \frac{C_2(t)}{dt} &= k_3 C_1(t) \\ y(t) &= C_1(t) + C_2(t) \end{cases} \tag{4.11}$$

And from this differential system the solution is

$$y(t) = \frac{K_1 k_3}{k_2 + k_3} \int_0^t C_p(\tau) d\tau + \frac{K_1 k_2}{k_2 + k_3} \int_0^t C_p(\tau) \cdot e^{-(k_2+k_3)(t-\tau)} d\tau \tag{4.12}$$

In this case the spectrum provided by the SA consists of two components, a trapping component and an equilibrating component (Figure 4.4B). The associated SA equation is

$$y(t) = \alpha_0 \int_0^t C_p(\tau) d\tau + \alpha_1 \int_0^t C_p(\tau) \cdot e^{-\beta_1 (t-\tau)} d\tau \tag{4.13}$$

where

$$\begin{cases} \frac{K_1 k_3}{k_2 + k_3} &= \alpha_0 \\ \frac{K_1 k_2}{k_2 + k_3} &= \alpha_1 \\ k_2 + k_3 &= \beta_1 \end{cases} \tag{4.14}$$

If in the model we include a rate constant for the transfer of the tracer from C_2 to C_1, k_4, the spectrum changes its configuration and what was the trapping component becomes a new equilibrating component (Figure 4.5B). This behavior is consistent with the change in the model (Figure 4.5A). Obviously the relationship between the α and β of the new spectrum with the rate constants is different from the one expressed in Equation 4.14. The new equivalence can be defined from the solution of the new model.

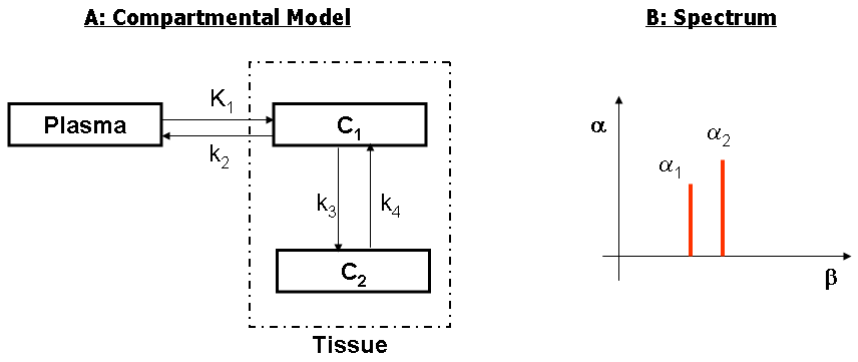

Figure 4.5: (A) Two-Compartmental model and (B) its relative spectrum

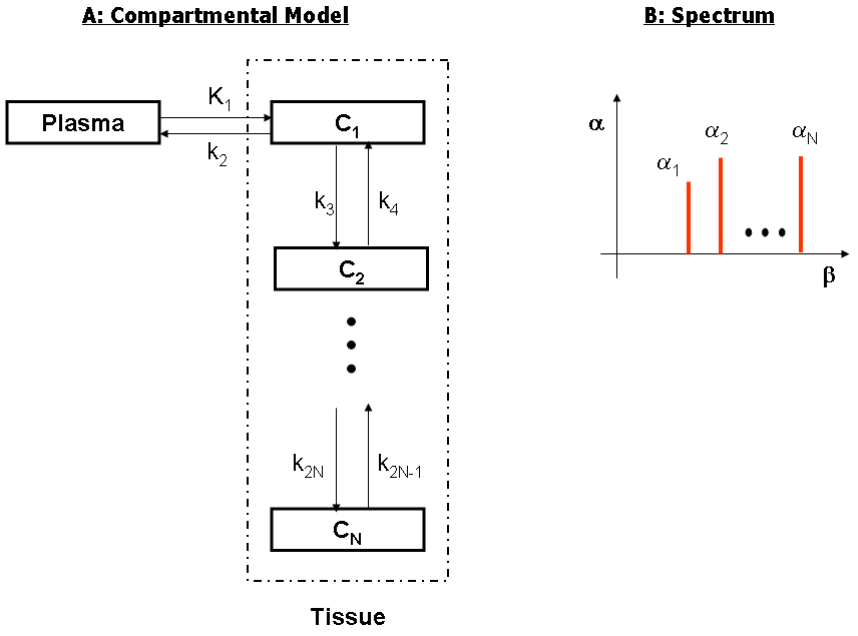

Figure 4.6: (A) N compartmental model and (B) its relative spectrum

Third example: N-compartmental catenary model (Figure 4.6A)

This model, with N compartments to describe the processes in the tissue and one for the blood, is translated in SA with a spectrum of N components. Each component refers to a specific compartment. To understand the relationship between compartment and component in the two representations we have to consider the speed of the different processes: the fastest physiological events are associated to the high frequency components (with the bigger values of betas); the slowest processes instead correspond to the low frequency components, indicated by a beta value very close to zero. In general to define the mathematical relationship from a compartmental model and its equivalent SA spectrum, the solution of the differential equation system is required. From this it is very easy to identify the number of components and the expressions for αs and βs of the spectrum. But can every model have an equivalent formulation in spectral analysis? The answer is no. In fact, it has been demonstrated that the spectral analysis technique can not be used with all linear compartmental systems [27]. There is in fact a set of conditions that must be fulfilled for it to be applied. Strongly connected systems that contain no cycles and for which the exchange of material with the environment is confined to a single compartment are shown to meet the conditions necessary for application of spectral analysis. Certain weakly connected systems that include traps as well as non-interconnected collections of such systems are also shown to meet the conditions. For what concerns this work, the leucine models meet the criteria for application of SA.
Considering the contribution of V_b and C_b in the system, the measurement equation of the examples defined as

$$y(t) = C_{tissue}(t) \tag{4.15}$$

becomes

$$y(t) = (1 - V_b) \cdot C_{tissue}(t) + V_b C_b \tag{4.16}$$

The way in which $C_{tissue}(t)$ is described, does not change. In fact, if we substitute $C_{tissue}(t)$ with the equation of the compartmental model or its corresponding SA expression, the equivalence between the two method remains the same as described above.

4.2.2 From the spectrum to the compartmental model

In the previous paragraph we have shown how a compartmental model can be translated into its equivalent in SA. In this paragraph instead we do the contrary, i.e. understand what are the models associated with different spectrums. What we know about SA is that each component refers at least to one compartment. In this way from the number of lines in a spectrum we can understand the minimum number of compartments which are necessary to model a system.
The problem is that the spectrum can not say how the compartments are linked each other. This uncertainty about the connection knowledge can be shown by an example. Let us consider a very simple spectrum with only two components: a trapping and an equilibrating component. The compartmental models compatible with this situation are two (Figure 4.7) with a completely different meaning: so what is the model corresponding to the original spectrum? It's impossible to answer. The example is a very simple situation but the problem becomes more complicated with increasing numbers of components.
In light of this, without any information about the physiological system that we are describing it is impossible to determine an unequivocal correspondence between a spectrum and its equivalent model. Therefore, for each spectrum we can only associate a class of equivalent compartmental representations which have

in common the same number of compartments.

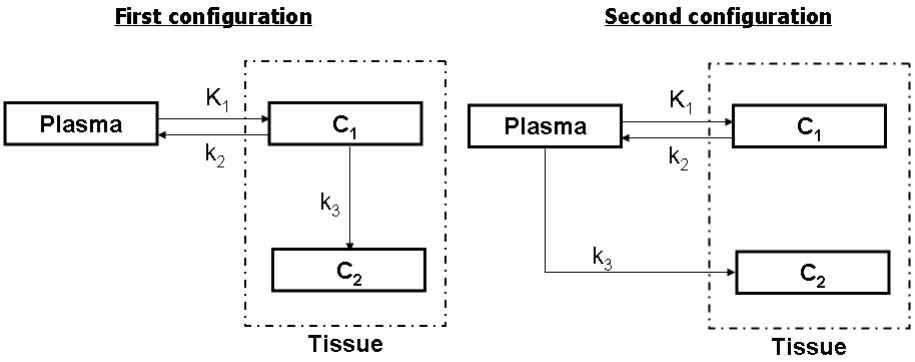

Figure 4.7: Two compartmental models. Although they have different configurations, they are both compatible with the same spectrum defined by a trapping and an equilibrating component.

4.3 The features of SA method

In this section we present the most important features of SA. As we have seen this technique does not require that the number of compartments be fixed before the elaboration, but rather it provides an estimate of the minimum number of compartments necessary to describe the kinetics of the system. The SA technique applies to heterogeneous as well as the homogenous tissues: this makes it particularly useful for the analysis of tracer kinetics in brain with PET because the limited spatial resolution of the scanner assures that most, if not all, measurements include activities form a heterogeneous mixture of gray and white matter. Furthermore the SA does not require steady state conditions for the tracer, unlike the multiple-time graphical analysis technique [24]. The SA also provides an estimate of the rate constant of trapping tracer in the tissue as well the amplitudes and decay constants of reversible components. This information can be used for subsequent specification of a kinetic model, or it can be used to estimate selected parameters of the system that do not depend on the specific model configuration, such as the total volume of distribution of the tracer [8].
However, as we have explained in the previous section, the spectrum provides only the minimum number of compartments and eventually the presence of trapping, but can not say anything about the configuration of these compartments in the system.
Another important characteristic of the SA method is that it provides a very good fit between its model description and the data. This feature is in agreement with the approach that SA uses for the estimation. In fact only the data, without any prior compartmental model design of the system, is used to provide the spectrum and the results are in perfect correlation with it. The problem is that SA fits the data so well that it tracks the noise as well, and the results can be corrupted by the pres-

ence of noise. The consequences of this directly influence the shape of the spectrum. The presence of noise in the data usually shifts the components from their true positions and sometimes can produce non-realistic components called "phantom components". The problem of phantom components in SA is not only due to the noise, but it also may depend on other factors such as the distortion present in the arterial plasma signal and the incapacity of algorithm to clearly distinguish the blood component. The effects of these elements in the spectrum are not as yet completely quantifiable.

About the accuracy, the SA technique has lower precision in parameter estimates than the compartmental model approach (Chapter 9). This is due to the large number of parameters of the SA model equation, number exactly equals to the number of betas in the fixed grid (~ 100). The SA precision is also conditioned by the fixed grid. In fact, the position of the components of the spectrum is limited by the choice of the betas. When the grid can not adequately approximate the position of the true components, the algorithm adapts by providing the double components. This effect is visible when there are two consecutive components detected in the spectrum (Figure 4.8). Due to the discrete nature of the grid, the algorithm can not place all the components in their correct positions, but only at betas defined by the grid. Sometimes to improve the fit of the data the algorithm splits the components in two parts placed in the closest possible positions of the best-fitting value. To resolve the problem we defined a very simple correction. In case of double components as $Comp_j(\beta_j; \alpha_j)$ and $Comp_{j+1}(\beta_{j+1}; \alpha_{j+1})$, a new component $Comp_{NEW}(\beta_{NEW}; \alpha_{NEW})$ is calculated to replace $Comp_j$ and $Comp_{j+1}$ in the spectrum. Following a weighted average approach β_{NEW} and α_{NEW} are defined as

$$\alpha_{NEW} = \alpha_j + \alpha_{j+1} \tag{4.17}$$

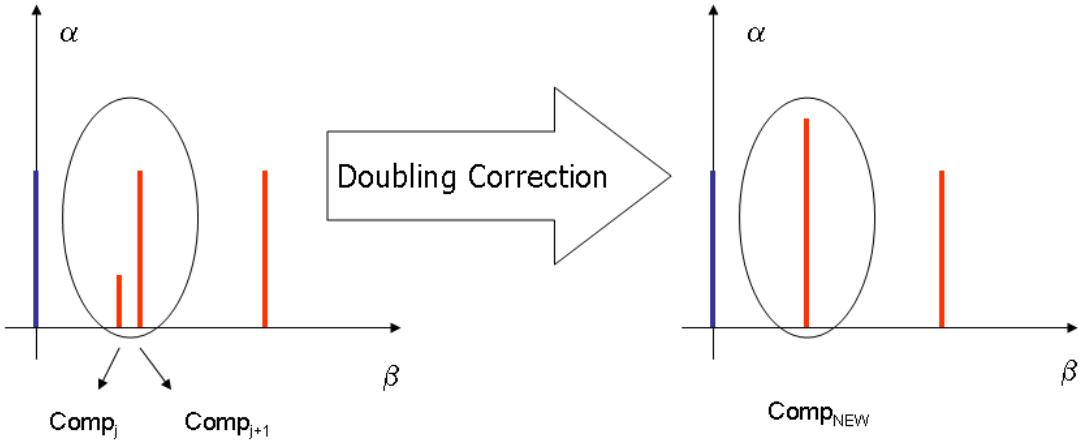

Figure 4.8: Double effect correction

$$\beta_{NEW} = \frac{\beta_j \cdot \alpha_j + \beta_{j+1} \cdot \alpha_{j+1}}{\alpha_j + \alpha_{j+1}} \tag{4.18}$$

The original spectrum and its corrected spectrum are obviously different but the curves, which they refer to, are so close that can not distinguished. In Figure 4.9 we can have an idea of how this kind of correction influences the signals trend.

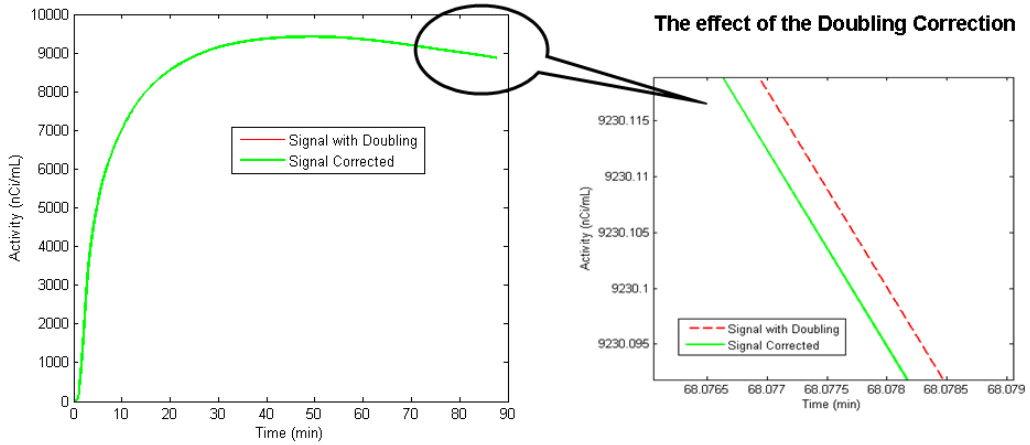

Figure 4.9: Signal with (Red line) and without (Green line) the double effect correction.

The last relevant characteristic of SA is related to the computational time. The SA model is linear, so in theory the spectrum can be easily evaluated by a linear estimation method with a very high computational efficiency. But, for the non-negativity restriction of the α_s, this is not possible to do and only minimization algorithms that implement this condition can be used with a consequent increase of computational time. However, these methods still have a very good efficiency and are extremely fast compared to the non linear methods. The non-negativity restriction is fundamental for the SA method. In fact, without this condition, we will obtain for a single estimation hundreds of different equivalent solutions with the same fit of the data. In all these spectra the negative components will eliminate the effects of positive ones and *vice versa* and so we will not have the typical spectrum of SA in which only the real components of the data are visible because they are different from zero. In Figure 4.10 we report an example.

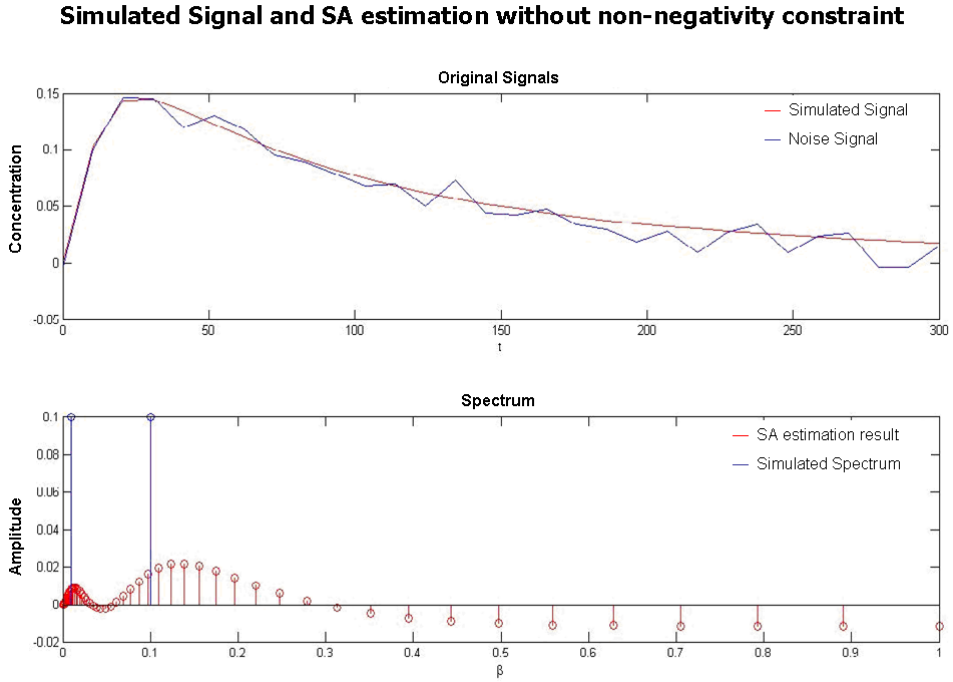

Figure 4.10: An example of SA estimation without non-negativity constraint.

4.4 Quantification and Choice of model

Depending on the information that we want extract from the data, the Spectral Analysis can be used in two different ways. The first approach is related to the quantification of the variables of interest and consists of the arrangement of the spectrum lines. Different examples of PET SA quantification have been used in different organs and for different tracers ([21]; [20]; [19]; [37]). To do this, a mathematical expression that explains the link between the variables of interest and the spectrum components is necessary. Usually this expression is defined using the relationship between the variables and the compartmental model, and the relationship between the compartmental model and SA. The system of equivalences is shown in Figure 4.11. Another way to use SA is for the definition of the most ap-

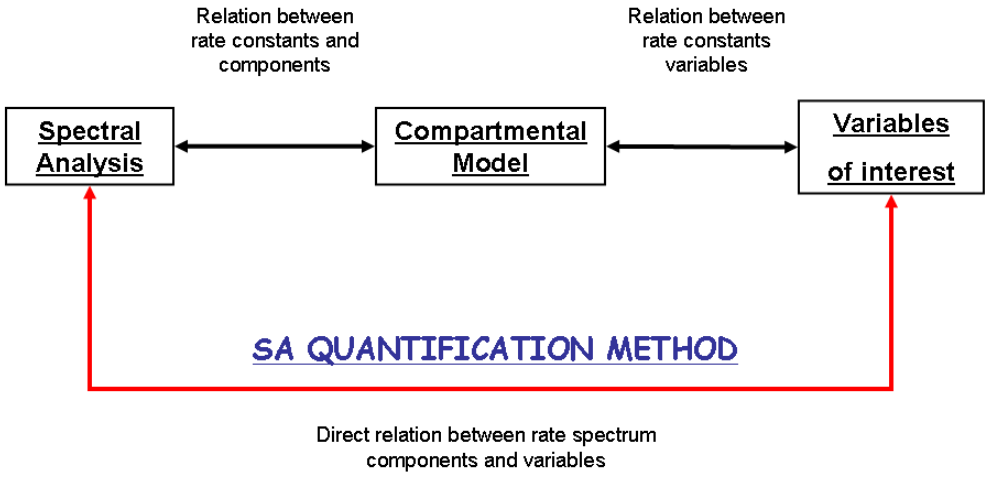

Figure 4.11: In this scheme the relationships between SA and compartmental model, compartmental model and variables of interest, and between SA and variables of interest, are shown. In particular, the red arrow indicates the relation used for the SA quantification.

propriate compartmental model to describe a set of data. In particular, SA is useful to determine the number of compartments present in a system, because as we explained previously

it can not say anything about their connections. This kind of approach could resolve the problem in leucine modeling. In fact, without any reliable results for the heterogeneous model identification, the SA could demonstrate if HET is better or worse than the homogenous model. In this way we could also quantify a measure of the heterogeneity in the tissue. To use the SA with this purpose a different approach to the standard SA implementation method is required. In fact, if the aim of SA is to find the number of exponential components of the system impulse response without having to define a structure beforehand, defining a grid of eigenvalues β_j and estimating only the relative amplitudes α_j is not necessary. The right approach to follow is simply to estimate M the number of exponentials necessary for the SA equation (Section 4.3, Equations 4.1- 4.3) to give a good fit to the data by using models of increasing order. For instance, one can start first with a one-exponential model

$$C_T(t) = \alpha_1 \cdot C_p(t) \otimes e^{-\beta_1 t} \tag{4.19}$$

and estimate by Weighted NLLS the parameters. Then trying a two-exponential order, with one trapping component

$$C_T(t) = \alpha_1 \cdot \int C_p(t) + \alpha_2 \cdot C_p(t) \otimes e^{-\beta_2 t} \tag{4.20}$$

and then with two equilibrating components

$$C_T(t) = \alpha_1 \cdot C_p(t) \otimes e^{-\beta_1 t} + \alpha_2 \cdot C_p(t) \otimes e^{-\beta_2 t} \tag{4.21}$$

and so on. The standard model parsimony criteria techniques [13] can be used to choose the best model. This way of applying SA has as an additional bonus: not only the standard deviation error of the αs estimates, but also the precision of the βs are provided. In fact, if the betas are selected from a predetermined grid, as in the standard SA approach, it is impossible to obtain a measure of their precision. Finally, estimation of the β_j avoids

the problem of the doubling.
In light of these considerations, this new SA approach provides a statistically model-independent information which can guide the selection of the most appropriate among the potential compartmental candidate structures. For our specific case, about the leucine PET data the candidate models are represented in part from the homogenous and heterogeneous models, but SA may find other solutions. As we know, the SA is extremely helpful to discriminate among potential compartmental models, but it does not give a unique answer and more than one structure may be compatible. To select the correct solution we will use known information about the leucine kinetics.

Chapter 5

The SA fixed model approach

5.1 The choice of the model for leucine PET data

In this section we apply the Spectral Analysis method to understand what compartmental representation is the best to describe the leucine PET data. To do this we used the SA approach for the choice of the model described in (Section 4.4). Six SA fixed models were selected as possible solutions: 3 with the trapping component and 3 without. The six equations of these models are reported below:
Model 1 (1 Equilibrating Component):

$$C_T(t) = \alpha_1 \cdot C_p(t) \otimes e^{-\beta_1 t} \tag{5.1}$$

Model 2 (1 Equilibrating Component +1 Trapping Component):

$$C_T(t) = \alpha_1 \cdot \int C_p(t) + \alpha_2 \cdot C_p(t) \otimes e^{-\beta_2 t} \tag{5.2}$$

Model 3 (2 Equilibrating Components):

$$C_T(t) = \alpha_1 \cdot C_p(t) \otimes e^{-\beta_1 t} + \alpha_2 \cdot C_p(t) \otimes e^{-\beta_2 t} \tag{5.3}$$

Model 4 (2 Equilibrating Components +1 Trapping Component):

$$C_T(t) = \alpha_1 \cdot \int C_p(t) + \alpha_2 \cdot C_p(t) \otimes e^{-\beta_2 t} + \alpha_3 \cdot C_p(t) \otimes e^{-\beta_3 t} \tag{5.4}$$

Model 5 (3 Equilibrating Components):

$$C_T(t) = \alpha_1 \cdot C_p(t) \otimes e^{-\beta_1 t} + \alpha_2 \cdot C_p(t) \otimes e^{-\beta_2 t} + \alpha_3 \cdot C_p(t) \otimes e^{-\beta_3 t} \quad (5.5)$$

Model 6 (3 Equilibrating Components +1 Trapping Component):

$$C_T(t) = \alpha_1 \cdot \int C_p(t) + \alpha_2 \cdot C_p(t) \otimes e^{-\beta_2 t} + \alpha_3 \cdot C_p(t) \otimes e^{-\beta_3 t} + \alpha_4 \cdot C_p(t) \otimes e^{-\beta_4 t} \quad (5.6)$$

All these models have been estimated through NLLS applied to leucine PET data. All the available ROIs for all the subjects have been examined. In the next paragraphs we report the results of this estimation.

5.1.1 The fit of the data

In Figure 5.1 we compare the differences between the measured data and the descriptions provided by the different models in the whole brain. Some of the models are not able to explain the data. These ineffective models (Fig 5.1A and 5.1E) do not include the trapping for the tracer. The others (Figure 5.1B, 5.1C, 5.1D and 5.1F), seem to show the same goodness of fit even though in Figure 5.1B and 5.1D the tails of the model-estimated curves do not fit as well as 5.1C and 5.1F.

5.1.2 The weighted residual trends

In Figure 5.2 we report the weighted residual trends for the whole brain PET data. The six pictures refer to the 6 models. The weighted residuals are obtained from the multiplication of the residuals with the data weights. If the estimation is good, the difference between the model-estimated and the measured data should be a representation of a white noise process[1], that

[1] White noise is a random signal (or process) with a flat power spectral density. In other words, the signal contains equal power within a fixed bandwidth at any center frequency.

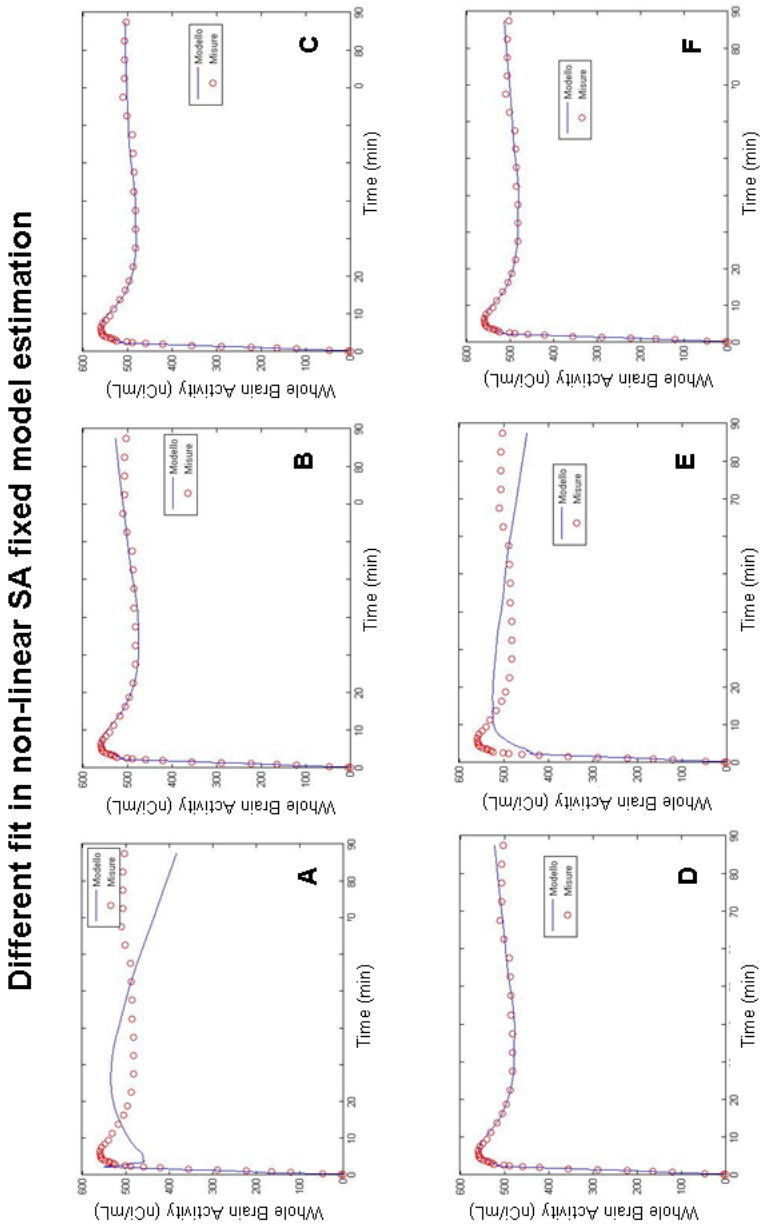

Figure 5.1: Different fit for different SA fixed model estimation. From Figure 5.1A to Figure 5.1G, we have in order the fit of the data with 1 eq model, 1 eq + trap model, 2 eq model, 2 eq + trap model, 3 eq model, 3 eq + trap model. We can see that only the presence of trapping compartment in the model can explain the data. In particular the graphs A and E show how the models that lack this feature fail completely to describe the measured data.

means that the residuals should be random and in the range $[-1; 1]$. The models associated at the pictures A and E do not present this behavior, and like Figure 5.1, do not agree with a good estimation. The others, instead, seem to be consistent with the expected trend.

5.1.3 The distribution of the components

In Figure 5.3, we report the distribution of the components detected in 9 subjects for the whole brain. Each picture refers to a different model. What we can see is that every distribution reports the presence of the trapping for all the subjects, even in those models in which is not explicitly defined. Also looking at the three distributions below we can see more or less the same trend, namely, it appears that one trapping an two equilibrating components are required.

5.1.4 Comparison through the Akaike Index

In Figure 5.4 we provide a comparison between the Akaike Information Criterion (AIC) indexes calculated from the different models. The values are the average between the subjects, defined for all the ROIs and for all the chosen models. As we can see, the best results come from the models with a trapping compartment and one or two reversible compartments. Considering the kinetics of leucine, these spectra are compatible with the homogenous (Section 3.1) and heterogeneous (Section 3.5) kinetic models, respectively. It's important to emphasize that in some regions (corona radiata and cerebellar white matter) the best solution coincides with the model with two equilibrating com-

White noise draws its name from white light in which the power spectral density of the light is distributed over the visible band in such a way that the eye's three color receptors (cones) are approximately equally stimulated. In statistics white noise is referred to a random process with $mean = 0$ and $SD = 1$.

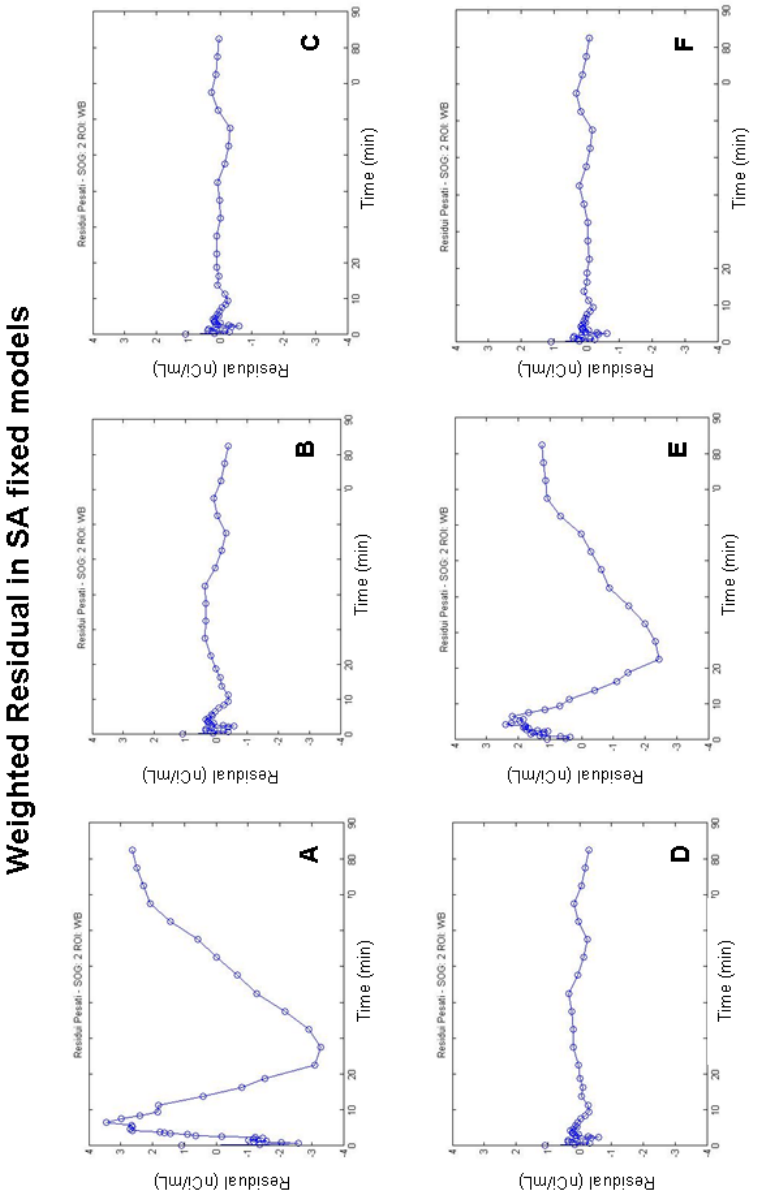

Figure 5.2: Weighted residuals in SA fixed model estimation. From figure A to figure G, we have in order the weighted residuals trend about 1 eq model, 1 eq + trap model, 2 eq model, 2 eq + trap model, 3 eq model, 3 eq + trap model. This kind of representation adds information about the goodness of the estimations. In fact, if the estimation is good, the trend of weighted residual should be random and between $[-1; 1]$. In particular we see that graphs A and E do not have this characteristic to underline again that the quality of estimation with these two models is very poor. The other ones have the expected trend.

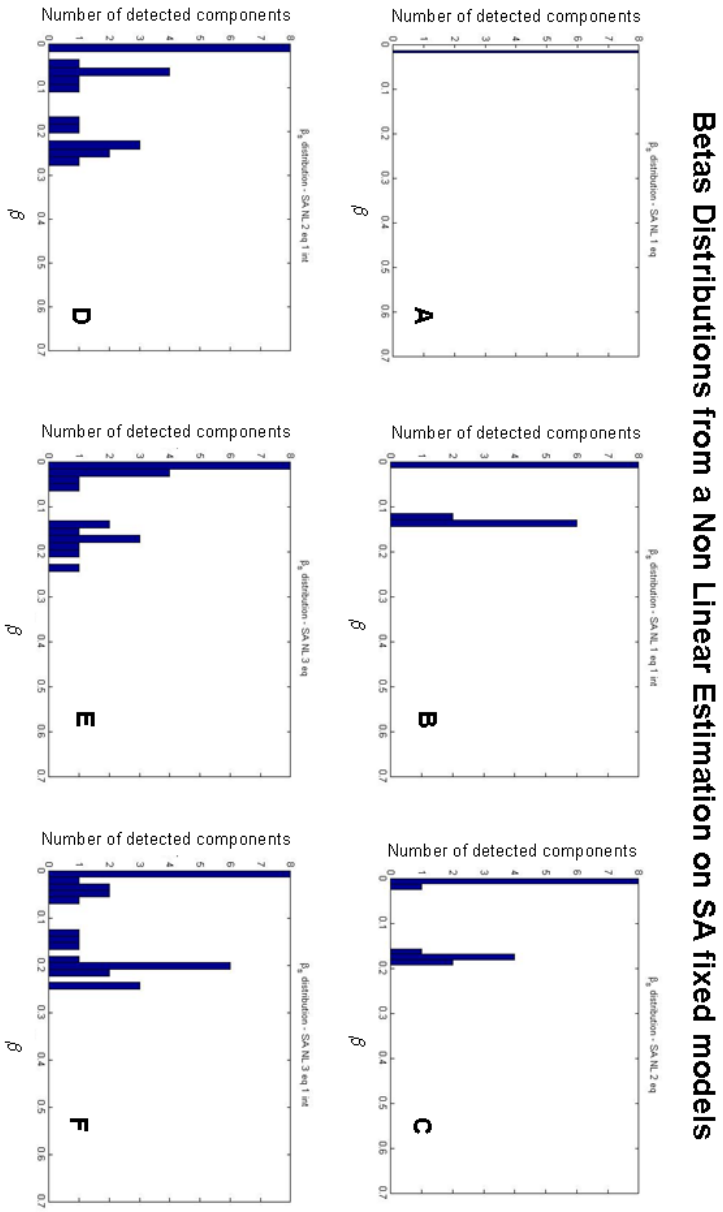

Figure 5.3: Different distributions of components in SA fixed model estimation. The histograms represent the distribution of the betas in 9 subjects. The picture shows how the trapping is necessary to explain the data. In fact there's always an important presence at $\alpha = 0$ or very close to it even when the model does not explicitly include trapping. The two last graphs on the bottom have a behavior very similar to the model 2eq + trap even though they have the freedom to assume other forms. This suggests that a model with a trapping and two reversible compartments may be the best solution.

ponents but, for these cases, the slowest component is so close to zero that it can be considered a trapping compartment. Also sometimes the differences between the models are very small, and more than one choice can be selected.

5.1.5 The Final Choice

Considering all the results shown above, we can conclude that the presence of trapping is necessary to explain the behavior of L-[1 $-^{11}$ C]leucine PET data. In fact, without it, unrealistic trends of residual and incompatible fits of the measured data are provided. When the trapping is not specified in the model, in the spectrum the slowest component shifts very close to zero, indicating that this component is required to describe the data. This feature is fundamental because it suggests that the behavior of the L-[1 $-^{11}$ C]leucine is consistent with our purpose to study protein synthesis. In fact, if the trapping were not included in the model of L-[1 $-^{11}$ C]leucine kinetics it would indicate that the tracer would be unsuitable for rCPS quantification.
Looking to the distribution trends and the Akaike comparison we can see that the best model requires the presence of heterogeneity in the tissues. However, in some few regions HOM is selected as the best data representation. This does not mean that for these ROIs we can exclude the presence of the tissue heterogeneity but some reasons (probably the small size of the ROI) may allow a homogenous representation as well as a heterogeneous one. In fact, for these particular regions the AIC for HOM is very similar to AIC for the HET.
Sometimes several models have an equivalent capacity to describe the same data and the choice of a best model is not so simple, but in light of the considerations about heterogeneity, and the results that we have shown the heterogeneous kinetic

model seems to be more reliable to describe the time curses of measured activity.

ROI	1 eq		1 eq + trap		2 eq		2 eq + trap		3 eq		3 eq + trap		BEST CHOICE
	mean	SD	mean	SD	mean	SD	mean	SD	mean	SD	mean	SD	
WholeBrain	225	9	138	47	141	65	123	123	157	67	124	70	2 eq + trap
Cerebellum	241	7	157	36	220	25	146	50	157	56	150	60	2 eq + trap
Vermis	250	27	184	58	217	73	182	182	207	51	188	63	2 eq + trap
FrontalCortex	229	8	144	42	212	34	136	136	168	49	137	59	2 eq + trap
TemporalCortex	220	11	136	50	152	65	130	130	154	49	133	61	2 eq + trap
OccipitalCortex	238	8	157	41	205	55	146	146	159	52	149	56	2 eq + trap
ParietalCortex	289	164	222	195	246	191	215	215	252	184	217	203	2 eq + trap
SupraorbitalGyrus	275	129	218	154	242	149	219	219	229	153	223	156	1 eq + trap
PreCentralGyrus	246	30	194	55	228	44	192	192	205	58	195	59	2 eq + trap
PostCentralGyrus	237	10	173	26	223	38	167	167	177	36	170	31	2 eq + trap
Thalamus	232	8	153	37	160	39	148	148	170	34	151	45	2 eq + trap
Putamen	254	39	186	71	199	69	190	190	207	65	194	71	1 eq + trap
Caudate	292	172	247	195	248	196	251	251	261	190	254	196	1 eq + trap
Hippocampus	316	309	285	323	285	323	287	287	291	323	291	324	1 eq + trap
Amygdala	204	19	169	31	169	31	171	171	178	29	175	31	1 eq + trap
Hypothalamus	238	11	212	14	212	16	215	215	216	17	218	16	1 eq + trap
CoronaRadiata	205	13	134	52	132	57	136	136	136	57	139	58	2 eq > 1 eq+ trap
CentrumSemiovale	320	306	259	335	275	329	263	263	264	335	266	335	1 eq + trap
CerebellarWhiteMatter	234	18	166	38	159	44	161	161	176	70	192	109	2 eq > 1 eq+ trap

Figure 5.4: Akaike Information Criterion (AIC). The results are the means ± SD for the 9 subjects.

5.2 The delay estimation with SA fixed model

Using different SA models (Equations 5.1 to 5.6) we re-estimated the time delay between tracer arrival in the brain and at the arterial sampling site. Our purpose was to understand if there are some correlations between the models used for describing the data and the estimates of the tracer delay. For the quantification of tracer delay, we used the same approach with fixed grid that was utilized for the homogeneous tissue model (Section 3.3). In Figure 5.5 we report the results of the tracer delay

	Tracer Delays (sec) with different models					
Subject	Homogenous model	1 Eq	2 Eq	3 Eq	1 Eq + trap	2 Eq +trap
1	14	8	14	16	13	13
2	5	1	5	6	4	6
3	4	0	4	4	4	4
4	1	0	1	1	1	1
5	5	0	5	5	4	5
6	11	0	11	12	11	13
7	14	6	15	14	14	14
8	9	0	9	9	7	8
9	13	1	13	12	10	13

Figure 5.5: Tracer arrival delays estimated with different models. For each subject the results are in very good agreement, except for the model with only one reversible compartment (1 Eq).

estimation. We can see a good agreement between the different approaches for each subject, except for the values provided by the model with only one reversible compartment (1 Eq). We know, in fact, that this model is not feasible to describe the data (Section 5.1). It is interesting to emphasize that different models, the heterogeneous as well as the homogeneous, give comparable delay estimates. This feature is true for all the subjects. Therefore, the tracer delay estimation can be considered model independent for all the model representations with a sufficiently good fit of the measured data.

Chapter 6

The Standard SA approaches

6.1 The mathematical relationship between the spectrum and variables of interest

In this section we present the relationship that exists between the components provided by SA in the analysis of L-[1 $-^{11}$ C]-leucine PET data and the variables of interest, in particular, λ and rCPS. To do this we show how each possible evaluated spectrum can be linked with its corresponding compartmental model and through this equivalence we describe the mathematical expressions that relate the αs and βs to the variables of interest.

6.1.1 First example: A spectrum with one trapping and one equilibrating component

As we have shown in previous chapters this kind of spectrum, in the particular case of L-[1 $-^{11}$ C]leucine PET data, refers to the HOM (Section 3.1). From this model we know that rCPS can be calculated from the rate constants as

$$\text{rCPS} = \left(\frac{K_1 k_4}{k_2 + k_3 + k_4}\right)\frac{C_p}{\lambda} = K_{Patlak}\frac{C_p}{\lambda} \tag{6.1}$$

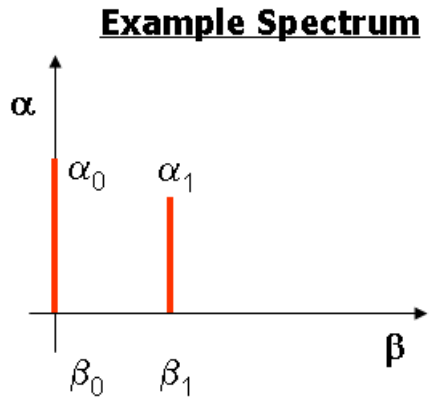

Figure 6.1: A spectrum with two components: one trapping and one equilibrating component.

where C_p is the arterial plasma concentration of unlabeled leucine, K_{patlak} is the net uptake rate constant for [^{11}C]leucine and λ is defined as

$$\lambda = \frac{k_2 + k_3}{k_2 + k_3 + k_4} \tag{6.2}$$

From the relationship between the homogenous model and SA (Section 4.2) we know also that

$$\frac{K_1 k_4}{k_2 + k_3 + k_4} = \alpha_0 = K_{Patlak} \tag{6.3}$$

and

$$\frac{K_1(k_2 + k_3)}{k_2 + k_3 + k_4} = \alpha_1 \text{ and } k_2 + k_3 + k_4 = \beta_1 \tag{6.4}$$

Equations 6.3, 6.4 define the equivalence between the spectral components and the model for the trapping and the reversible compartment respectively. There are some notation differences between the leucine homogenous model (Chapter 3) and the standard homogenous model (Chapter 4). The equivalence of the parameters is provided by the following table.

Homogenous leucine model	Standard homogenous model
K_1	K_1
$k_2 + k_3$	k_2
k_4	k_3

Table 6.1: Equivalence between Homogenous leucine model and Standard homogenous model.

Using this relationship we translated the equations for equivalence between SA and the homogeneous standard model (Equations 4.11-4.14) to the ones for the equivalence between SA and HOM (Equations 6.3- 6.4).
We can observe that from the sum of the αs we have

$$\alpha_0 + \alpha_1 = \frac{K_1 k_4}{k_2 + k_3} + \frac{K_1(k_2 + k_3)}{k_2 + k_3 + k_4} = K_1 \tag{6.5}$$

Substituting Equation 6.2 for λ into Equation 6.4 we have

$$\alpha_1 = \frac{K_1(k_2 + k_3)}{k_2 + k_3 + k_4} = K_1 \frac{k_2 + k_3}{k_2 + k_3 + k_4} = K_1 \cdot \lambda \tag{6.6}$$

Combining Equation 6.6 with 6.5 we have

$$\lambda = \frac{\alpha_1}{K_1} = \frac{\alpha_1}{\alpha_0 + \alpha_1} \tag{6.7}$$

Therefore Equation 6.1 can be written in terms of SA variables as

$$\text{rCPS} = K_{Patlak} \frac{C_p}{\lambda} = \alpha_0 \frac{C_p}{\lambda} = \frac{\alpha_0 \cdot (\alpha_0 + \alpha_1)}{\alpha_1} C_p \tag{6.8}$$

Equation 6.8 shows the relationship between the spectrum and the parameters of interest that we were looking for.

6.1.2 Second example: A spectrum with one trapping and two equilibrating components

Among all the possible compartmental models compatible with the considered spectrum, we can easily observe that for the characteristics of the tracer only HET (Section 3.5) is consistent with

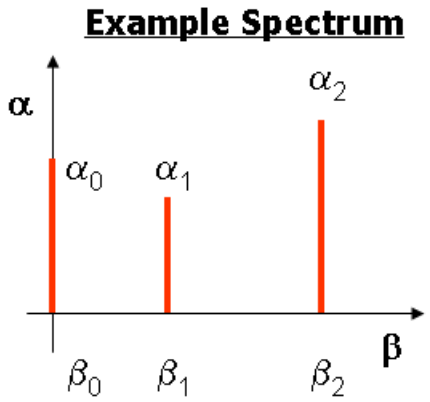

Figure 6.2: A spectrum with three components: one trapping and two equilibrating components.

this SA solution. In this case the variables of interest are defined as

$$\begin{aligned} \text{rCPS} &= K_{Patlak}\frac{C_p}{\lambda} \\ &= \left(\frac{w_a K_{1a} k_{4a}}{k_{2a}+k_{3a}+k_{4a}} + \frac{w_b K_{1b} k_{4b}}{k_{2b}+k_{3b}+k_{4b}}\right)\frac{C_p}{\lambda} \end{aligned} \tag{6.9}$$

and

$$\lambda = \frac{k_{2a}+k_{3a}}{k_{2a}+k_{3a}+k_{4a}} = \frac{k_{2b}+k_{3b}}{k_{2b}+k_{3b}+k_{4b}} \tag{6.10}$$

Considering Equation 3.11 we can formulate the link between the spectrum and the model as

$$\alpha_0 = K_{Patlak} = \left(\frac{w_a K_{1a} k_{4a}}{k_{2a}+k_{3a}+k_{4a}} + \frac{w_b K_{1b} k_{4b}}{k_{2b}+k_{3b}+k_{4b}}\right) \tag{6.11}$$

$$\alpha_1 = \left(\frac{w_a K_{1a}(k_{2a}+k_{3a})}{k_{2a}+k_{3a}+k_{4a}}\right) \text{ and } \beta_1 = k_{2a}+k_{3a}+k_{4a} \tag{6.12}$$

$$\alpha_2 = \left(\frac{w_b K_{1b}(k_{2b}+k_{3b})}{k_{2b}+k_{3b}+k_{4b}}\right) \text{ and } \beta_2 = k_{2b}+k_{3b}+k_{4b} \tag{6.13}$$

with

$$w_a \geq 0, w_b \geq 0 \text{ and } w_a + w_b = 1 \tag{6.14}$$

Now if we sum α_0, α_1 and α_2 we obtain through the simplifications

$$\sum_{j=0}^{2} \alpha_j = \alpha_0 + \alpha_1 + \alpha_2 = w_a K_{1a} + w_b K_{1b} = K_1^* \tag{6.15}$$

where K_1^* is the weighted average of K_1. Defining

$$\lambda_a = \frac{k_{2a} + k_{3a}}{k_{2a} + k_{3a} + k_{4a}} \tag{6.16}$$

$$\lambda_b = \frac{k_{2b} + k_{3b}}{k_{2b} + k_{3b} + k_{4b}} \tag{6.17}$$

if we make the assumption that

$$\lambda_a = \lambda_b = \lambda \tag{6.18}$$

we obtain

$$\begin{aligned} \textstyle\sum_{j=1}^{2} \alpha_j &= \alpha_1 + \alpha_2 = w_a K_{1a} \lambda_a + w_b K_{1b} \lambda_b = \\ &= (w_a K_{1a} + w_b K_{1b}) \lambda = K_1^* \lambda \end{aligned} \tag{6.19}$$

Furthermore

$$\lambda = \frac{\alpha_1 + \alpha_2}{K_1^*} = \frac{\alpha_1 + \alpha_2}{\alpha_0 + \alpha_1 + \alpha_2} \tag{6.20}$$

With this value of λ rCPS becomes

$$\text{rCPS} = K_{Patlak} \frac{C_p}{\lambda} = \alpha_0 \frac{C_p}{\lambda} = \frac{\alpha_0 \cdot (\alpha_0 + \alpha_1 + \alpha_2)}{\alpha_1 + \alpha_2} C_p \tag{6.21}$$

6.1.3 Third example: A spectrum with one trapping and N equilibrating components

Let us consider a spectrum with one trapping and N-equilibrating components. This spectrum is consistent with leucine PET data in which we have N different tissues mixed together, and each tissue contains one trapping and one equilibrating component.

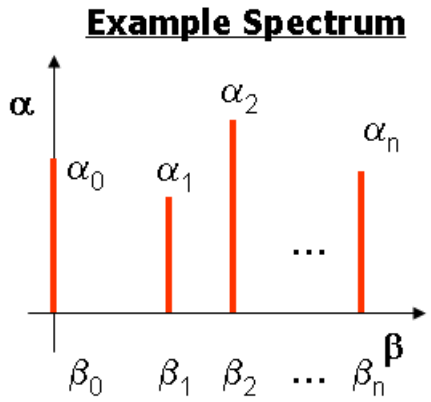

Figure 6.3: A spectrum with (N+1) components: one trapping and N-equilibrating component.

A possible compartmental representation, therefore, can be defined by generalizing the heterogeneous model (Figure 6.4). To calculate the expression for the rCPS and λ depending on the αs and βs of the spectrum we can repeat the same procedure of the previous example.

1. The variables of interest are expressed from the compartmental model rate constants as:

$$\begin{aligned} \text{rCPS} &= K_{Patlak}\frac{C_p}{\lambda} = \\ &= \left(\frac{w_a K_{1a} k_{4a}}{k_{2a}+k_{3a}+k_{4a}} + \frac{w_b K_{1b} k_{4b}}{k_{2b}+k_{3b}+k_{4b}} + \cdots + \frac{w_N K_{1N} k_{4N}}{k_{2N}+k_{3N}+k_{4N}}\right)\frac{C_p}{\lambda} \end{aligned} \tag{6.22}$$

$$\begin{aligned} \lambda &= \frac{k_{2a}+k_{3a}}{k_{2a}+k_{3a}+k_{4a}} = \frac{k_{2b}+k_{3b}}{k_{2b}+k_{3b}+k_{4b}} = \\ &= \frac{k_{2N}+k_{3N}}{k_{2N}+k_{3N}+k_{4N}} \end{aligned} \tag{6.23}$$

2. The parameters of the spectrum are related to the rate

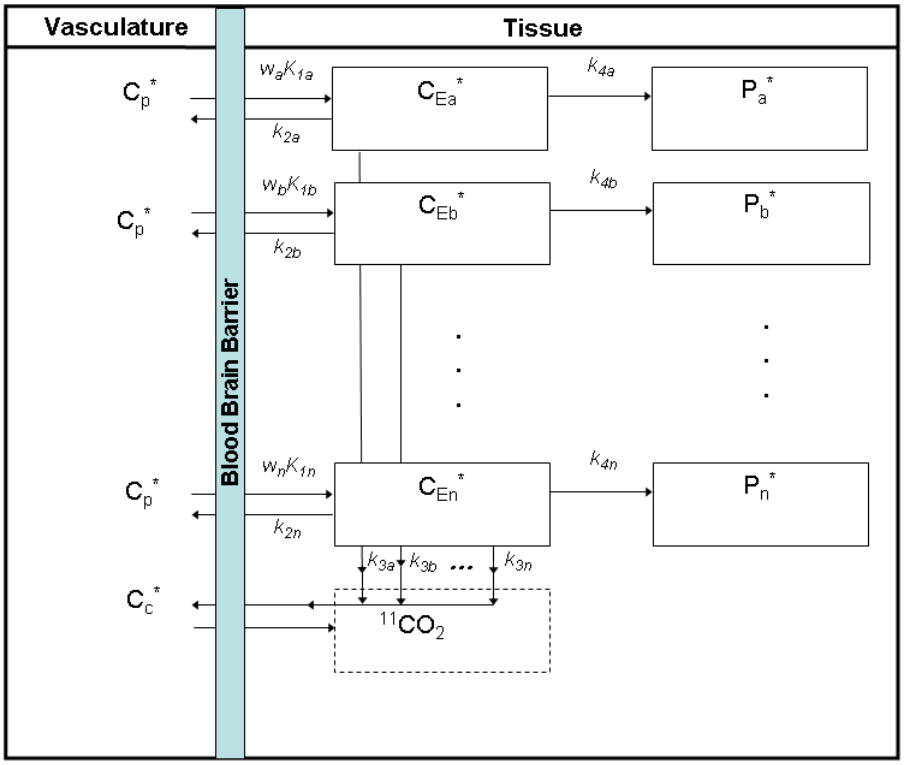

Figure 6.4: The generic heterogeneous model for the L-[$1-^{11}C$]leucine PET.

constants as

$$\begin{aligned}\alpha_0 &= K_{patlak} = \\ &= \left(\frac{w_a K_{1a} k_{4a}}{k_{2a}+k_{3a}+k_{4a}} + \frac{w_b K_{1b} k_{4b}}{k_{2b}+k_{3b}+k_{4b}} + \cdots + \frac{w_N K_{1N} k_{4N}}{k_{2N}+k_{3N}+k_{4N}}\right)\end{aligned} \tag{6.24}$$

$$\alpha_1 = \left(\frac{w_a K_{1a}(k_{2a}+k_{3a})}{k_{2a}+k_{3a}+k_{4a}}\right) \text{ and } \beta_1 = k_{2a}+k_{3a}+k_{4a} \tag{6.25}$$

$$\alpha_2 = \left(\frac{w_b K_{1b}(k_{2b}+k_{3b})}{k_{2b}+k_{3b}+k_{4b}}\right) \text{ and } \beta_2 = k_{2b}+k_{3b}+k_{4b} \tag{6.26}$$

$\ldots$

$$\alpha_N = \left(\frac{w_N K_{1N}(k_{2N}+k_{3N})}{k_{2N}+k_{3N}+k_{4N}}\right) \text{ and } \beta_N = k_{2N}+k_{3N}+k_{4N} \tag{6.27}$$

with

$$w_a \geq 0, w_b \geq 0, \ldots, w_N \geq 0 \text{ and } w_a + w_b + \ldots w_N = 1 \tag{6.28}$$

3. We define

$$\lambda_j = \frac{k_{2j}+k_{3j}}{k_{2j}+k_{3j}+k_{4j}} \text{ with } j = a, b, \ldots, N. \tag{6.29}$$

and note that

$$\sum_{j=0}^{N} \alpha_j = \sum_{j=0}^{N} w_j K_{1j} = K_1^* \tag{6.30}$$

4. We furthermore assume that λ is the same in all tissues in the mixture, i.e.,

$$\lambda_j = \lambda \forall \text{ with } j = a, b, \ldots, N. \tag{6.31}$$

5. The sum of all α's corresponding to the equilibrating components is given by

$$\begin{aligned}\textstyle\sum_{j=1}^{N} \alpha_j &= w_a K_{1a}\lambda_a + w_b K_{1b}\lambda_b + \cdots + w_N K_{1N}\lambda_N = \\ &= (w_a K_{1a} + w_b K_{1b} + \cdots + w_N K_{1N})\lambda = K_1^*\lambda\end{aligned} \tag{6.32}$$

6. Finally combining the equations above we have the solutions

$$\lambda = \frac{\sum_{j=1}^{N} \alpha_j}{K_1^*} \tag{6.33}$$

$$\text{rCPS} = K_{Patlak}\frac{C_p}{\lambda} = \alpha_0 \frac{C_p}{\lambda} = \frac{\alpha_0 \cdot (\sum_{j=0}^{N} \alpha_j)}{\sum_{j=1}^{N} \alpha_j} C_p \tag{6.34}$$

6.1.4 Solutions for a generic spectrum

The last expressions of the previous paragraph (Equations 6.33, 6.34), give a powerful mathematical tool to calculate rCPS and λ from every spectrum estimated from leucine PET data. To arrive at these equations, it's important to emphasize two assumptions that were made.

The first is the presence of the trapping component. In fact, as we have seen in Chapter 5, in the analysis of the leucine PET data, the trapping is indispensable for describing the data. Without this feature the estimated data provided by the model is unrealistic, compared with the measured data. If the trapping is not present in the spectrum, it is possible that the presence of noise and some other errors in the data shift this component into a nonzero position. For this reason, when this happens we consider the lowest frequency component as trapping.

The second assumption concerns the equivalence of lambda in the different tissues. This hypothesis, even though reasonable, may not be completely true. In fact, we know that the variability of λ in the different regions is low [2], but we must keep in mind that these estimates of λ were based on a homogenous tissue model which may not adequately describe the data. However, without a measure of the heterogeneity in the tissues that allows to measure the weights w_i, this simplification is necessary to provide the relationship between the spectrum and the variables of interest.

In light of these considerations, however, the Equations 6.33, 6.34 provide a reasonable mathematical tool to relate every kind of spectrum with the variables of interest. We will use this approach to estimate rCPS and λ, from each spectrum provided by each of the SA techniques that we present in this and the following chapters.

6.2 The Cunningham SA Method

6.2.1 The method

The first Spectral Analysis approach that we used for the quantification of the variables of interest is the Cunningham method [8]. This approach consists of applying the SA as it is defined without any filtering of the data or of the spectrum. Considering the context of leucine PET data, we adapted the equation of SA model (Section 4.1) to the equation of the total activity in the ROI (Equation 3.2). In fact, if the total radioactivity detected by the PET scanner can be expressed as

$$C_{measured}(t) = (1 - V_b) \cdot [C_{tissue}(t) + V_D \cdot C_c(t)] + V_b \cdot C_b(t) \quad (6.35)$$

then using the SA equation we can write 6.35 as

$$C_{measured}(t) = (1 - V_b) \cdot [\sum_{j=0}^{M} \alpha_j \cdot C_p(t) \otimes e^{-\beta_j t} + V_D \cdot C_c] + V_b \cdot C_b \quad (6.36)$$

where

$$\beta_0 = 0. \quad (6.37)$$

From 6.36 we estimated directly the values of αs and V_b using the *lsqnonneg.m* Matlab function, and from the results we calculated rCPS and by Equations 6.33, 6.34.
It is useful to emphasize that to apply *lsqnonneg.m* function the measurement equation expressed in 6.36 has to be arranged in a different way. This is due to the presence of the term $V_D \cdot C_c(t)$, whose value is known, between the unknown parameters. To resolve this problem we defined

$$\alpha_j^* = (1 - V_b) \cdot \alpha_j \quad (6.38)$$

And Equation 6.36 becomes

$$\begin{aligned} C_{measured}(t) &= [\sum_{j=0}^{M} \alpha_j^* \cdot C_p(t) \otimes e^{-\beta_j t}] + \\ &+ (1 - V_b) \cdot V_D \cdot C_c(t) + V_b \cdot C_b(t) \\ &= [\sum_{j=0}^{M} \alpha_j^* \cdot C_p(t) \otimes e^{-\beta_j t}] + \\ &+ V_D \cdot C_c(t) + V_b \cdot [C_b(t) - V_D \cdot C_c(t)] \end{aligned} \tag{6.39}$$

Subtracting the $V_D \cdot C_c(t)$ known value from the data we can write a new equation from which it is now possible to apply directly the estimation function

$$\begin{aligned} C_{measured}(t)^* &= C_{measured}(t) - V_D \cdot C_c(t) = \\ &= [\sum_{j=0}^{M} \alpha_j^* \cdot C_p(t) \otimes e^{-\beta_j t}] + V_b \cdot [C_b(t) - V_D \cdot C_c(t)] \end{aligned} \tag{6.40}$$

From the values of α^*s and V_b we can compute the values of the αs as

$$\alpha_j = \frac{\alpha_j^*}{1 - V_b} \tag{6.41}$$

Without this arrangement, which does not violate the principles of SA methods, it is not possible to evaluate directly the values of αs and V_b using the *lsqnonneg.m* function.

6.2.2 Results

We report the rCPS results provided with Cunningham SA and compared with the NLLS-HOM estimates (Figure 6.5). The values are in complete disagreement. The rCPS estimates are very different and also the SA intersubject variability, expressed by the SD or the CV, is not reasonable (CV is about 50% for all the regions). In Figure 6.6 we have a graphic representation of the results. We can see again that there is no correspondence between the Cunningham SA estimates and the ones calculated

with the HOM approach. In particular, the rCPS values measured with SA are largely underestimated, and even including the SD, there is no match between the methods. The same observations can be formulated from Figures 6.7 and 6.8 in which the specific estimates in one of the 9 subjects provided by the two methods are compared. As for the averages, rCPS is underestimated with the Cunningham approach.

6.2.3 Considerations

In light of the results, the Cunningham SA approach for the quantification of rCPS can not be considered a valid instrument. There is necessarily something wrong in the procedure of estimation. The first thing to check is the capacity of the SA to explain the data. In Figure 6.9 we report the fit between the SA model and the data in the noisiest region (hypothalamus) and in the least noisy ROI (wholebrain). According with the different levels of noise the trends provided by the SA model are good and explain the data very well. Probably, the causes of the failure of the Cunningham SA in the analysis of leucine PET data are due to something uncorrected in the spectrum. In fact, the values for the trapping components are not what we expected from the NLLS-HOM estimates. For these reasons, the application of a filter in the spectrum, as defined by the Turkheimer SA, may improve the quality of the results.

rCPS (nmol/g/min)

ROI	Cunningham SA			HOM method		
	mean	SD	CV (%)	mean	SD	CV (%)
WholeBrain	0.67	0.33	48.76	1.85	0.10	5.48
Cerebellum	0.63	0.29	46.19	2.20	0.12	5.46
Vermis	1.12	0.57	50.62	2.18	0.12	5.51
FrontalCortex	0.64	0.35	54.73	2.16	0.13	6.03
TemporalCortex	1.06	0.66	61.99	2.01	0.13	6.47
OccipitalCortex	0.97	0.78	80.06	2.33	0.20	8.60
ParietalCortex	0.66	0.53	80.53	2.14	0.19	8.88
SupraorbitalGyrus	1.00	0.67	67.47	2.01	0.14	6.96
PreCentralGyrus	1.41	0.42	30.17	1.93	0.21	10.87
PostCentralGyrus	1.40	0.39	27.79	1.90	0.17	8.96
Thalamus	0.56	0.37	66.53	1.72	0.10	5.83
Putamen	0.74	0.54	73.07	1.45	0.10	6.92
Caudate	0.50	0.40	80.50	1.16	0.10	8.65
Hippocampus	0.98	0.53	54.00	1.82	0.14	7.70
Amygdala	0.83	0.36	43.30	1.63	0.12	7.38
Hypothalamus	1.03	0.57	55.24	1.37	0.21	15.28
CoronaRadiata	0.55	0.33	60.35	0.98	0.07	7.14
CentrumSemiovale	0.70	0.30	42.22	1.09	0.09	8.68
CerebellarWhiteMatter	0.84	0.23	27.56	1.37	0.12	9.15

Figure 6.5: rCPS (nmol/g/min) estimated by the Cunningham SA method and NLLS fitting of the data with HOM. Values are means ± SD for the 9 subjects.

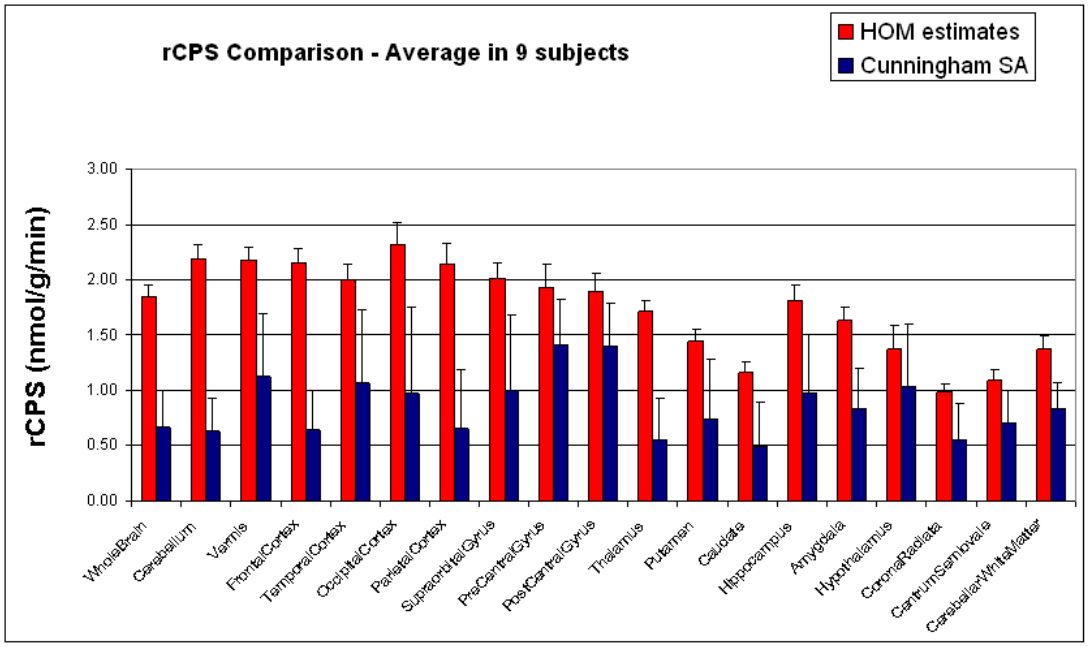

Figure 6.6: Bar graph of the rCPS averages in all ROIs quantified with NLLS-HOM method (red bars) and Cunningham SA (blue bars).

ROI	Cunningham SA					NLLS-HOM
	α_0	SMALLEST beta	Vb	λ	rCPS	rCPS
Whole Brain	0.0029	0.0000	0.061	1.00	0.37	1.69
Amygdala	0.0029	0.0000	0.049	1.00	0.37	1.49
Caudate	0.0085	0.0000	0.036	0.99	1.09	1.06
CentrumSemiovale	0.0028	0.0000	0.000	1.00	0.35	1.11
CerebellarWhiteMatter	0.0066	0.0038	0.033	0.99	0.85	1.28
Cerebellum	0.0072	0.0000	0.070	0.99	0.93	2.03
CoronaRadiata	0.0081	0.0000	0.100	0.99	1.05	1.00
Frontal	0.0015	0.0000	0.049	1.00	0.19	1.93
Hippocampus	0.0082	0.0000	0.052	0.98	1.05	1.70
Hypothalamus	0.0093	0.0000	0.050	0.98	1.20	1.22
Occipital	0.0055	0.0000	0.054	0.99	0.71	1.99
Parietal	0.0071	0.0000	0.068	0.99	0.92	1.79
PostCentralGyrus	0.0022	0.0000	0.056	1.00	0.28	1.82
PreCentralGyrus	0.0006	0.0000	0.064	1.00	0.08	1.78
Putamen	0.0067	0.0000	0.072	0.99	0.86	1.32
SupraorbitalGyrus	0.0017	0.0055	0.045	1.00	0.21	1.81
Temporal	0.0050	0.0000	0.028	0.99	0.65	1.81
Thalamus	0.0062	0.0000	0.000	0.98	0.81	1.72
Vermis	0.0039	0.0000	0.060	0.99	0.50	1.97

Figure 6.7: Comparison of the rCPS (nmol/g/min) estimates for NLLS-HOM method and Cunningham SA. The results refer to one of the 9 subjects of the study.

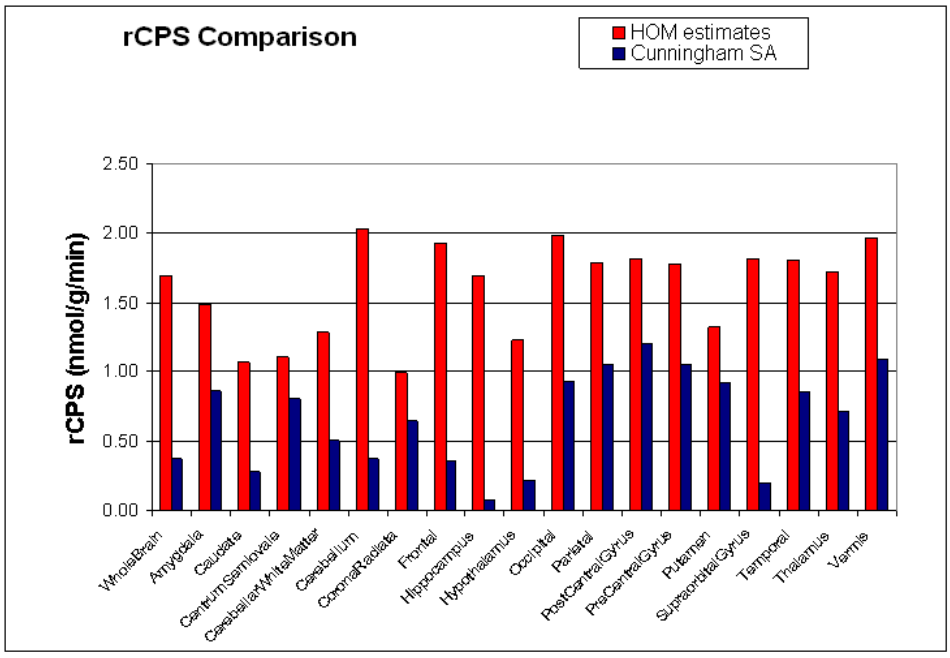

Figure 6.8: Bar graph of the rCPS distribution in all ROIs quantified with NLLS-HOM method (red bars) and Cunningham SA (blue bars). The values refer to one of the subjects.

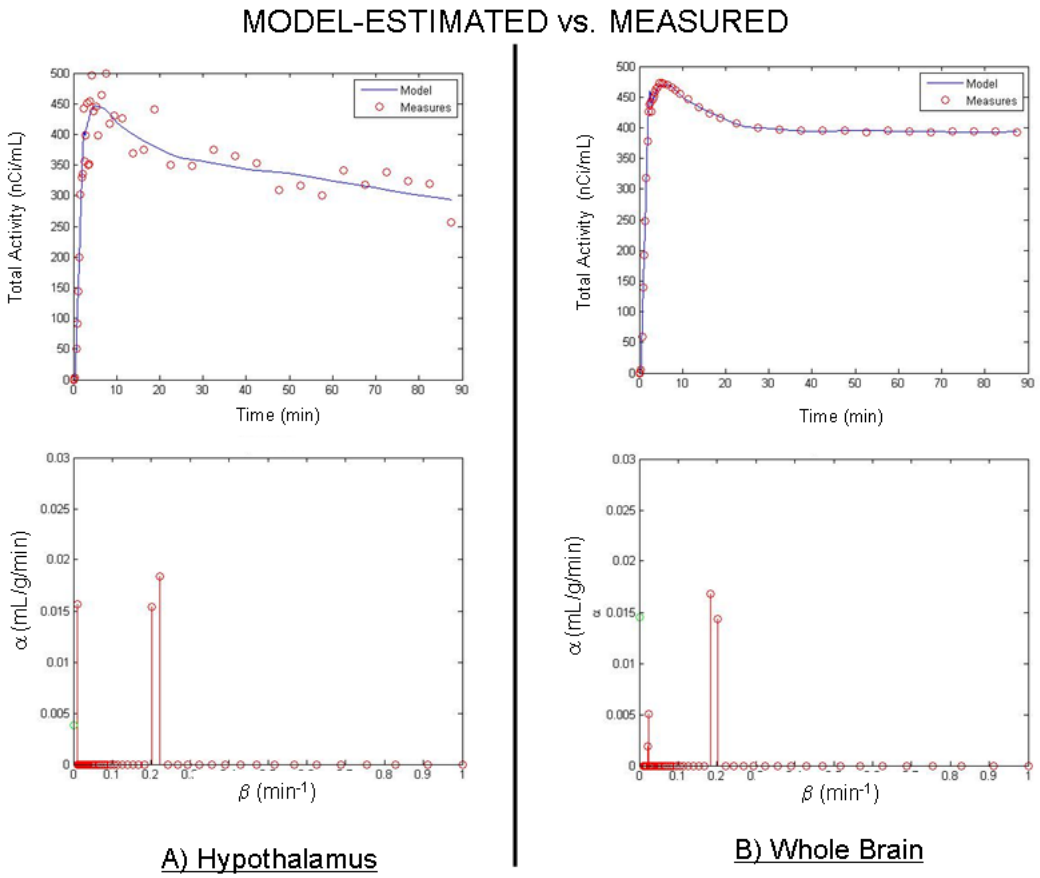

Figure 6.9: The graphs report the fit and the spectrum provided with Cunningham SA in one subject. The group A is related to the hypothalamus, the group B to the whole brain region.

6.3 Turkheimer SA

6.3.1 The method

In order to overcome the limits of Cunningham SA technique for the quantification of λ and rCPS in leucine PET data we seek to improve the Spectral Analysis estimation algorithm with the Turkheimer filter. This approach consists of the application of a simple numerical filter for the spectrum provided with the Cunningham SA. With this method, all the identified components, with exponents greater than zero but less than $\beta_{cut-off}$ are assumed to have been shifted from β_0 due to noise in the data, and the remaining components with exponents greater than $\beta_{cut-off}$ are assumed to correspond to real equilibrating processes in the system. To compute α_0 with this filter, the blood component and all the identified equilibrating components whose exponents are higher than $\beta_{cut-off}$ are subtracted from the total radioactivity data to obtain the integrated component, $\alpha_0 \int C_p^*(t)dt$, plus noise. A linear least squares procedure is then used to estimate α_0 as the slope of the graph of the integrated component versus $\int C_p^*(t)dt$.
The first consequence of the Turkheimer filter is to "clean"the spectrum from the influence of noise, in particular for what concerned the low frequency components and the trapping, and so to obtain a better solution than the no-filter SA. The role of $\beta_{cut-off}$ is fundamental because it decides where the noise ends and the real components start.
Although the improvement provided by the Turkheimer SA is important, this filter can not be sufficient for the particular case of rCPS quantification in leucine PET data as will be shown in this section. In fact, unlike the common SA application for estimation of the rate of regional cerebral glucose utilization (rCMRglu), in which only the value of the trapping was used

for quantification of the variables of interest (i.e. no correction for blood in the brain was made), we have seen that for the evaluation of λ and rCPS all the components of the spectrum are required (Section 6.1). For this reason, the entire spectrum has to be corrected for the noise effect, the high frequency components as well as the low ones. Therefore, we have elaborated a double Turkheimer filter to make this kind of spectrum correction in the entire range of frequencies.
The double Turkheimer filter uses the same approach as the simple one but with two $\beta_{cut-off}$, a low and a high value, that identify what is called the cut-off interval. The goal of the method is to eliminate all the components outside this interval and thereby improving the quality of estimation for the trapping component, in the low side of the spectrum, and for the V_b, which does not belong properly to the spectrum but can be confused with high-frequency components. To do this, the double filter Turkheimer method uses the same simple filtering: the contribution of the components located inside the cut-off interval is subtracted from the measured data; from the result new values of α_0 and V_b are estimated through a linear least squares algorithm. This change sounds reasonable and robust with the particular characteristics of the data: reasonable because in this way we corrected the spectrum at low and high frequencies; robust because the α_0 and V_b have so different influences in the data that cannot be confused in the filtering estimation process. The cut-off interval has the same importance as the single $\beta_{cut-off}$ in the simple filtering. It selects what part of the spectrum is consistent with true kinetic processes and what is not, and for this reason choice of the interval is very critical for the final results.

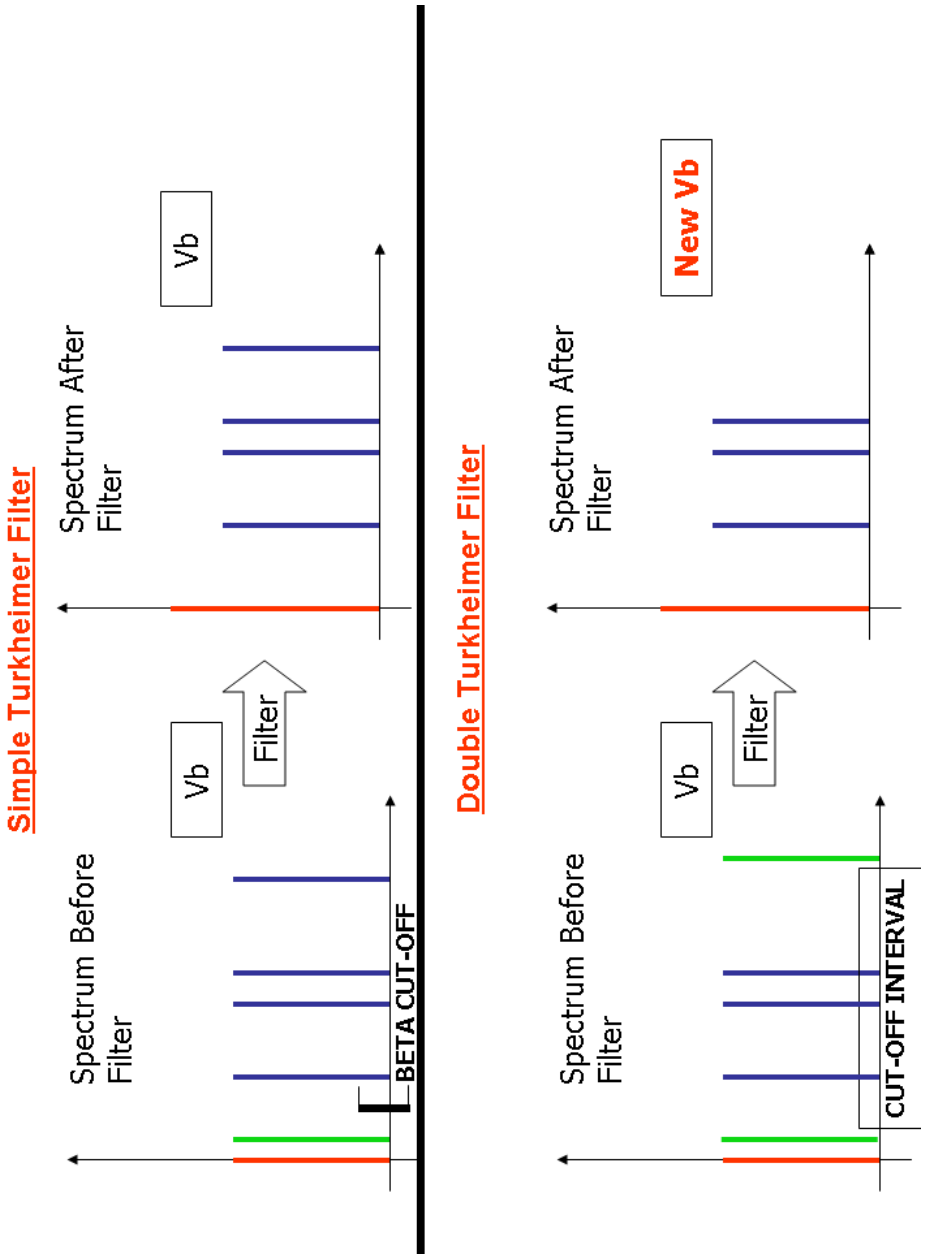

Figure 6.10: A graphical representation of the simple and the double Turkheimer filtering

6.3.2 The simulation experiment

Before applying the SA with the Turkheimer double filter to the measured data we have tested the characteristics of the algorithm in simulation studies. The idea that we followed was to define a dataset as realistic as possible, and for this data understand the behavior of the double filter under different conditions. The spectrum from which we generated the simulated signals was chosen from the previous analyses of the HOM and HET results. From these estimates we selected a spectrum with two equilibrating components, one trapping component and $V_b = 0.05$ (Figure 6.11). For these values, αs, βs and the corresponding variables of interest have been calculated the Equations 6.33, 6.34 (Figure 6.12). Then 1,000 realizations of

Component	Beta (min^{-1})	Alpha ($mL\ g^{-1}\ min^{-1}$)
Trapping	0.00	0.01
Slow equilibrating	0.05	0.01
Fast equilibrating	0.20	0.04

Figure 6.11: Simulated spectrum

Variables	Value
K patlak - ($mL\ g^{-1}\ min^{-1}$)	0.010
K1 ($mL\ g^{-1}\ min^{-1}$)	0.060
Lambda	0.833
rCPS ($nmol\ g^{-1}\ min^{-1}$)	0.887

Figure 6.12: Simulated variables of interest

noisy signals have been generated using for the arterial plasma, the $^{11}CO_2$ and the whole blood activity from blood samples measured in one of the subjects of the study, and for noise the same

statistical description that as was used to weight the data (Chapter 3).
From this dataset we estimated the variables of interest under the following conditions as:

- Different numbers of βs on the grid (to evaluate phantom components)
- Different grid choices (DiStefano or Logarithmic)
- Different cut-off values
- Different noise levels
- Different signal lengths (60, 75, or 90 mins)

The estimates among all the simulated signals have been compared with the simulated values of Figure 6.12 in order to understand the quality of the results and the characteristics of the algorithm. We used as performance indexes:

- The Averages of variables of interest compared with simulated values (to understand Bias)
- The Parameter distribution (histogram shape, standard deviation)
- The Component distribution (histogram shape compared to the simulated spectrum)

6.3.3 The simulation results

In this part we report the results for the SA with double Turkheimer filter for the different simulated conditions.

Different numbers of betas on the grid

We tested 3 grids with 50, 100 and 200 betas, respectively, but we did not see any difference in the estimates and in the distributions of the parameters. We could only see a slightly more accurate component distribution for the 200-beta grid that, however, had a higher computational time cost. We decided to use 100-beta grid because it represents a good compromise between results and processing time.

Different grid choices

In Figure 6.13 we show the different distribution of betas with DiStefano and two logarithmic grids. For the low frequency betas the grids have the same density of samples and it is impossible to distinguished one from the others. In the high frequencies side, instead, the grids present different beta distributions. However, this difference does not influence the detection of the spectrum because the components of the simulated data belong to the low frequency side. Therefore they can be detected with the same accuracy with all the three kind of tested grids. We finally decided to apply always in this work the DiStefano distribution to follow the standard convention typical of SA studies.

Different values for the cut-off interval

This is the most interesting part of the simulation study because it links the filter bounds with the final results of the estimation. In particular, we are interested in finding the optimal choice for the cut-off interval, i.e. the filter that provides the best estimates, i.e., those with low bias and a low standard error. This choice is fundamental for our study because the value selected based on the simulation experiment will be applied to the anal-

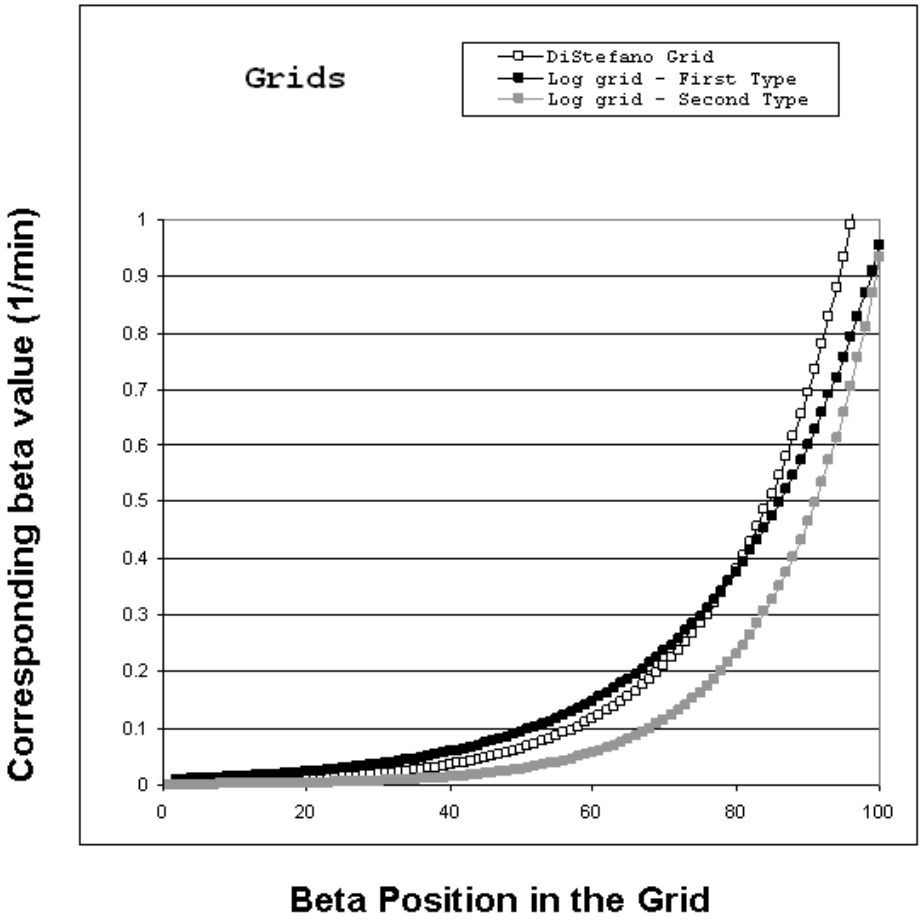

Figure 6.13: Comparison between different grid distributions. The first 50 components of grids represent quite similarly the same range of spectrum and so for the SA estimations are equivalent.

ysis of the measured data, as we have no other basis on which to decide the best cut-off value to use. To determine this best solution we tried different bound values for both the sides of the filter interval. These values were chosen taking into consideration the frequency of the blood sampling and the duration of the experiment in order to define the slowest and the fastest component detectable from the data.

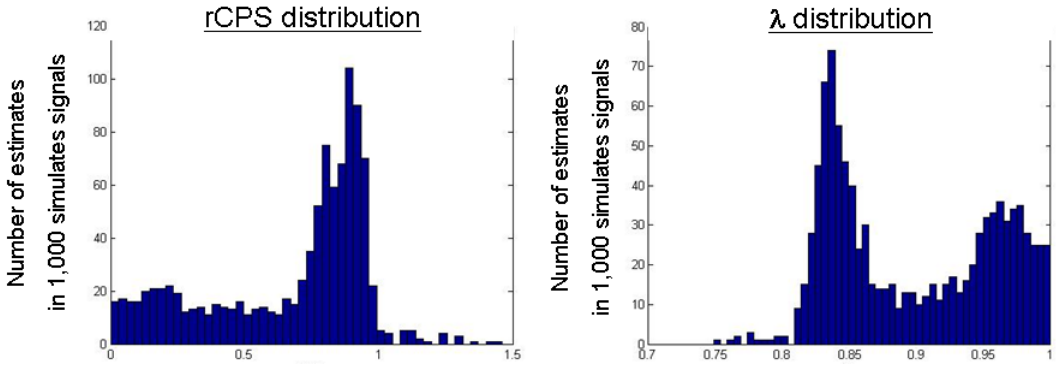

Figure 6.14: The histograms represent rCPS and λ distributions for one of the selected cut-off intervals. The quality indexes for the estimates have to take in account the bias as well as the distribution of the results. In the shown cases, in fact, the average bias is very low but the distributions have high variance.

Different noise levels

In this section we report the results of the simulations with different levels of noise. The signals were defined using the same expression used for the description of the data error (refer to the law of the error). The range of the noise was modulated through the scale factor N. For the other simulations this value was set to 0.5 comparable to a mid level for a ROI, but, in this particular case, N was changed in a range comparable with the lowest to highest possible noise level present a ROI. The results, as we expected, show that the bias and the standard deviation in

estimates of the variables of interest are inversely related to the level of the noise, but even for the nosiest signals they assumed acceptable values.

Different Data Acquisition lengths

This simulation provides information regarding the minimal time of data acquisition necessary to obtain accurate estimates for our variables of interest. The question that we want to answer is if we can obtain the same quality of estimates with a shorter duration of the PET data acquisition: shorter data acquisition would be an obvious advantage for the comfort of the patient. For this reason the algorithm has been applied to signals of 60, 75 and 90 minutes length using as cut-off interval the optimal choice selected from the simulation.
The results provided by the SA with the double Turkheimer filter show that without a length of 90 minutes the bias of the estimates became quite high (Figure 6.15).

	λ		rCPS (nmol/g/min)		
Data Acquisition lengths	mean	SD	mean	SD	BIAS (%)
SIMULATED VALUES	0.833	^^	0.887	^^	^^
60 minutes	0.799	0.057	0.817	0.32	7.9
75 minutes	0.842	0.038	0.845	0.21	4.5
90 minutes	0.835	0.023	0.892	0.13	0.6

Figure 6.15: λ and rCPS estimates in different data lengths. The results are the mean $\pm$ SD for 1,000 simulated signals.

6.3.4 The application of the SA with double Turkheimer filter in measured data

The results obtained from the simulations with the Turkheimer double filter are not as good as expected, but, with the optimal value of the cut-off interval, this method can provide acceptable

values for the estimates. This behavior justifies its application for the quantification of the variables of interest in measured data. In Figures 6.16,6.17 and 6.19 we report the results for our 9 subjects. The data represent mean and SD for the 9 subjects. Even though the means are be generally consistent with the NLLS-HOM results, the SD, in particular for the rCPS and λ, is extremely high (the inter-subject variability is more than 100% of the mean). To acquire more information about the Turkheimer SA behavior, as we have done for the NLLS-HOM and for the Cunningham SA, we considered the fit of the model with the data. An example is shown in Figure 6.18: what was a perfect agreement with the data in the Cunningham SA is now completely lost. We have, in fact, an underestimation and an overestimation of the measured that is similar to a HOM fit. In light of these results we can say that the application of SA with the double Turkheimer filter for the leucine PET data is not a useful method.

6.3.5 Considerations

The results provided by the Spectral Analysis with the double Turkheimer filter are unacceptable as were the Cunningham SA estimates. Although the Cunningham SA method does not provide correct estimates for the variables of interest, the fit of the data was very good. With the Turkheimer filter, instead, we lose this characteristic. The reason may be related to some facet of filtering process. In particular, the fit with the data seems to suggest that there is something similar to the HOM model behavior. In fact, in the trend of the Turkheimer SA estimated signal (Figure 6.18) there is the same under and overestimation typical of the homogenous tissue kinetic model. Looking at the spectrum before and after the filtering we observed that the correction made by the algorithm changes the number of

	Kpatlak (mL/g/min)		k1(mL/g/min)		Vb		Fit
ROI	mean	SD	mean	SD	mean	SD	WRSS
WholeBrain	0.00730	0.008	0.0521	0.037	0.070	0.05	2.2
Cerebellum	0.01031	0.012	0.0643	0.045	0.091	0.06	112.8
Vermis	0.01072	0.012	0.0643	0.045	0.085	0.06	73.7
FrontalCortex	0.00993	0.011	0.0551	0.039	0.078	0.05	77.0
TemporalCortex	0.00838	0.010	0.0505	0.036	0.075	0.05	7.2
OccipitalCortex	0.01089	0.013	0.0637	0.045	0.082	0.06	112.4
ParietalCortex	0.00972	0.011	0.0546	0.039	0.081	0.06	124.2
SupraorbitalGyrus	0.00956	0.011	0.0537	0.038	0.070	0.05	86.9
PreCentralGyrus	0.00905	0.010	0.0655	0.046	0.069	0.05	41.4
PostCentralGyrus	0.01025	0.012	0.0604	0.043	0.077	0.05	255.8
Thalamus	0.00729	0.008	0.0534	0.038	0.062	0.04	13.6
Putamen	0.00736	0.008	0.0563	0.040	0.057	0.04	40.8
Caudate	0.00560	0.006	0.0399	0.028	0.044	0.03	32.5
Hippocampus	0.00580	0.007	0.0372	0.026	0.103	0.07	85.8
Amygdala	0.00628	0.007	0.0330	0.023	0.085	0.06	75.9
Hypothalamus	0.00956	0.006	0.0528	0.037	0.049	0.03	162.7
CoronaRadiata	0.00430	0.005	0.0302	0.021	0.036	0.03	10.2
CentrumSemiovale	0.00497	0.006	0.0313	0.022	0.038	0.03	13.1
CerebellarWhiteMatter	0.00548	0.006	0.0393	0.028	0.000	0.00	278.3

Figure 6.16: SA with double Turkheimer filter. The results are the mean $\pm$ SD for 9 subjects.

	λ		rCPS(nmol/g/min)	
ROI	Mean	SD	mean	SD
WholeBrain	0.720	0.509	1.497	1.06
Cerebellum	0.679	0.480	2.244	1.59
Vermis	0.667	0.471	2.376	1.68
FrontalCortex	0.639	0.452	2.296	1.62
TemporalCortex	0.668	0.472	1.855	1.31
OccipitalCortex	0.658	0.465	2.447	1.73
ParietalCortex	0.644	0.455	2.229	1.58
SupraorbitalGyrus	0.644	0.455	2.194	1.55
PreCentralGyrus	0.724	0.512	1.847	1.31
PostCentralGyrus	0.661	0.467	2.294	1.62
Thalamus	0.727	0.514	1.482	1.05
Putamen	0.738	0.522	1.472	1.04
Caudate	0.719	0.509	1.150	0.81
Hippocampus	0.688	0.487	1.246	0.88
Amygdala	0.619	0.438	1.498	1.06
Hypothalamus	0.768	0.543	1.177	0.83
CoronaRadiata	0.716	0.506	0.888	0.63
CentrumSemiovale	0.682	0.483	1.076	0.76
CerebellarWhiteMatter	0.721	0.510	1.125	0.80

Figure 6.17: SA with double Turkheimer filter. The results are the mean ± SD for 9 subjects.

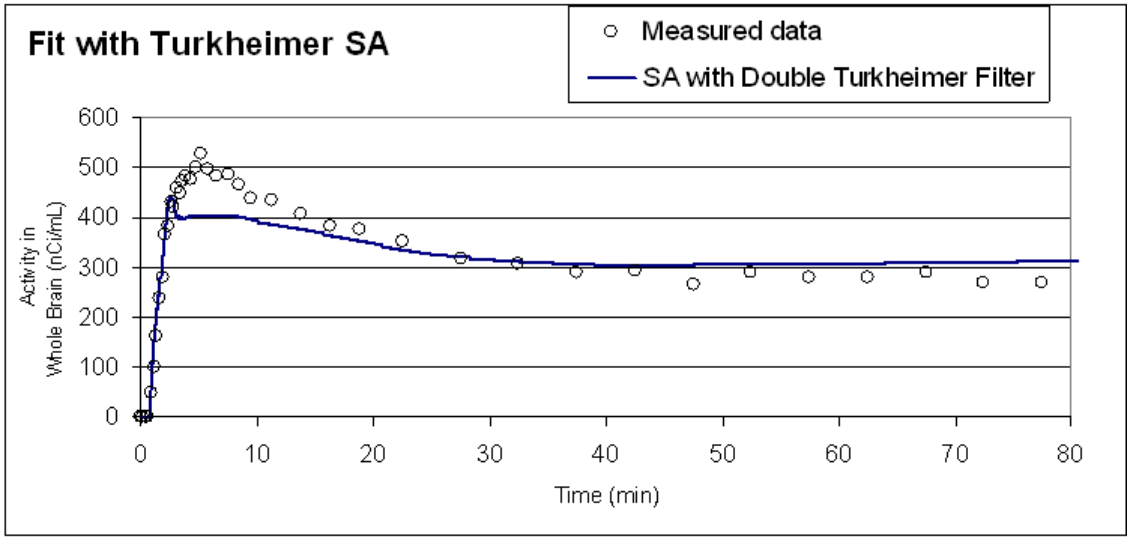

Figure 6.18: SA with double Turkheimer filter. Fit of the Whole Brain measured data of one subject.

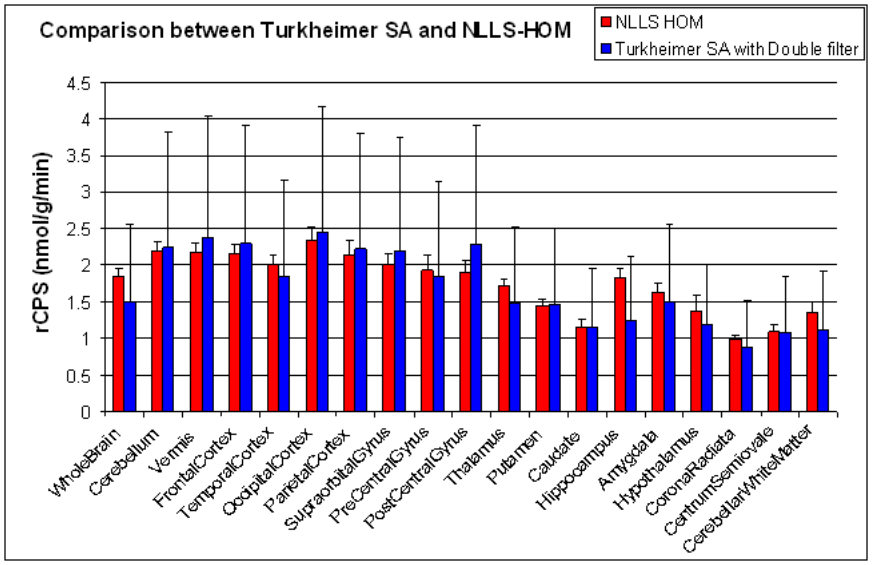

Figure 6.19: Bar graph of the rCPS averages in all the ROI quantified with NLLS-HOM method (red bars) and Turkheimer SA (blue bars). Lines show inter-subject standard deviation.

the equilibrating components. In most of the simulated cases in which the pre-filtered spectrum was comparable with a heterogeneous representation, we finally obtained after the filtering a spectrum equivalent to a homogenous representation (Figure 6.20). The cause of this problem is related at the filter imple-

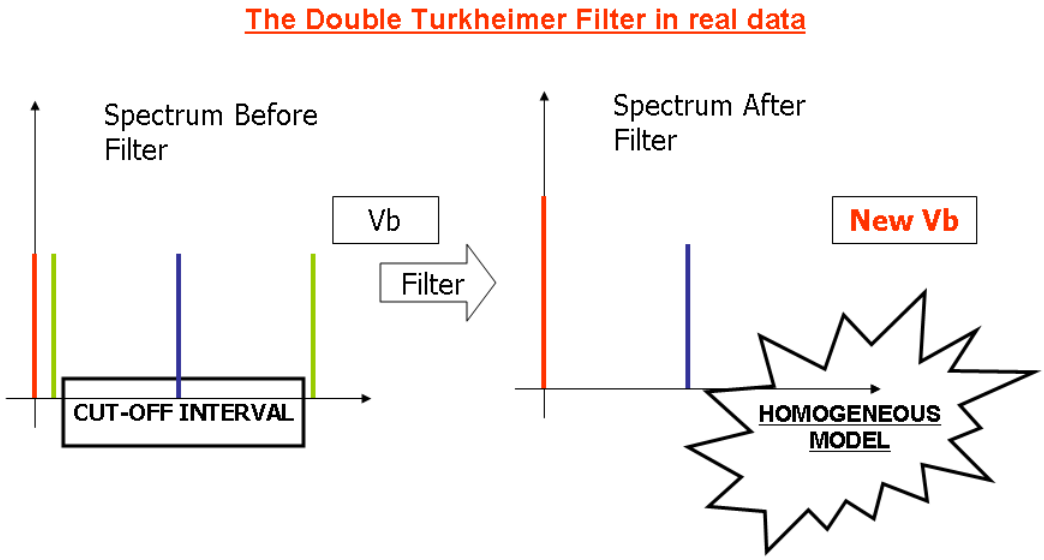

Figure 6.20: Representation of the SA with the Turkheimer double filter effect in the fitting of measured data.

mentation (Figure 6.20). In fact, with the approach that it uses the components outside the cut-off interval are eliminated for a new value of the trapping and V_b. But this is not completely correct. In fact the presence of these components is, in part, due to the presence of noise, in part due to the trapping and V_b, but for another part due to real equilibrating components

that we have to take in account if we want to describe the data correctly. This mistake will be resolved with the introduction of a new SA approach described in the next chapter.

Chapter 7

A new Spectral Analaysis algorithm

7.1 The Spectral Analysis Iterative Filter (SAIF)

7.1.1 Introduction

To overcome the limits of the "standard" Spectral Analysis techniques such as the Cunningham method and the Turkheimer double filter approach, we developed a new Spectral Analysis algorithm with the purpose of providing good quality estimates of rCPS and λ from leucine PET data. Our starting point for the definition of this new method was the Turkheimer SA method and its limitations. As we have seen in the previous chapter (Section 6.3) the components that we eliminated from the original spectrum with the filtering were due to a mixture of effects:

1. the presence of noise and errors into the input function signal[1];

2. the trapping and the blood volume that could not be clearly detected;

[1]The input function used for the quantification of the variables of interest is an approximation of the true plasma signal. Even though we corrected the blood samples for the tracer arrival delay we did not take in account other phenomena as the *"distortions"* introduced by the vessels geometry.

3. the presence of real equilibrating components of the system.

The Turkheimer SA, instead, does not consider for the slowest components the third possibility[2] and this may be the origin of the strange fit between the model estimated curves and uncorrected estimation of the variables of interest. The new method takes into account all these contributions that influence the spectral component detection in the normal SA. To accomplish this, we defined a correction filtering composed of two parts. In the first, using the same procedure as the double Turkheimer filter: we remove the equilibrating components and new values of the trapping component and V_b are estimated. In the second part the trapping and the blood volume are removed from the data and the method re-estimates the equilibrating components. These two steps are repeated until a stabilization of the WRSS is reached. For the presence of this iterative cycle in the correction of the spectrum we have called this method Spectral Analysis Iterative Filter (SAIF).

7.1.2 Details

In the previous paragraph we have introduced the idea on which the SAIF algorithm is based. Now, let us explain the details of the method. Firstly, the data were processed with the Cunningham SA in order to provide the spectrum for the filtering process. Then, after the selection of the cut-off interval, the cycle of iteration for the correction of the spectrum is applied. The procedure can be divided in the following points:

1. **The double Turkheimer filter:** The components inside the cut-off interval are subtracted from the data and new values of the trapping compartment and the fraction of volume occupied by the blood (V_b) are estimated (*1st filtering*);

[2]Because the Turkheimer SA is interesting principally in the trapping component estimate, it does not require an accurate evaluation of the other components of the spectrum.

2. **The new estimation of the equilibrating components:** Using the same principle as the *1st filtering* the new values of trapping and blood contribution are subtracted from the original data. From the results the components inside the cut-off interval are re-estimated using a nonnegative estimation algorithm (*2nd filtering*);

3. **Stop Criterion:** The difference between the WRSS before and after the filter correction is calculated: if it is less than 0.1% the algorithm stops. Otherwise the algorithm restarts from point 1.

In Figure 7.1 we illustrate the operative mechanism of the SAIF (Details of the SAIF algorithm are in Appendix C). The role of the cycle is fundamental: through this the algorithm we attempt to strike a balance between the equilibrating components and the limit components (the trapping and V_b) by eliminating those components which are outside the cut-off interval.
The choice of WRSS variation as index for stop criterion is very important in the SAIF. In fact, with this strategy we do not need to define *a priori* the number of iterations, but the characteristics of the analyzed data determine when the iterations are stopped. In practice, with a mid level of noise in the data, the number of iterations ranges from 1 to 50. In the case in which all equilibrating components estimated from standard SA are inside the cut-off interval, no additional iterations are made by SAIF.
Like the SA Turkheimer method, the cut-off choice represents the prior information about the data. This knowledge, used for the algorithm to provide better estimates, greatly influences the final spectrum, and therefore also the estimates of the variables of interest. For these reasons it is very important to find an optimal value to apply in the algorithm. As with the Turkheimer SA approach we used a simulation to find an optimal value for

the cut-off interval; the same value was then applied to the measured data.

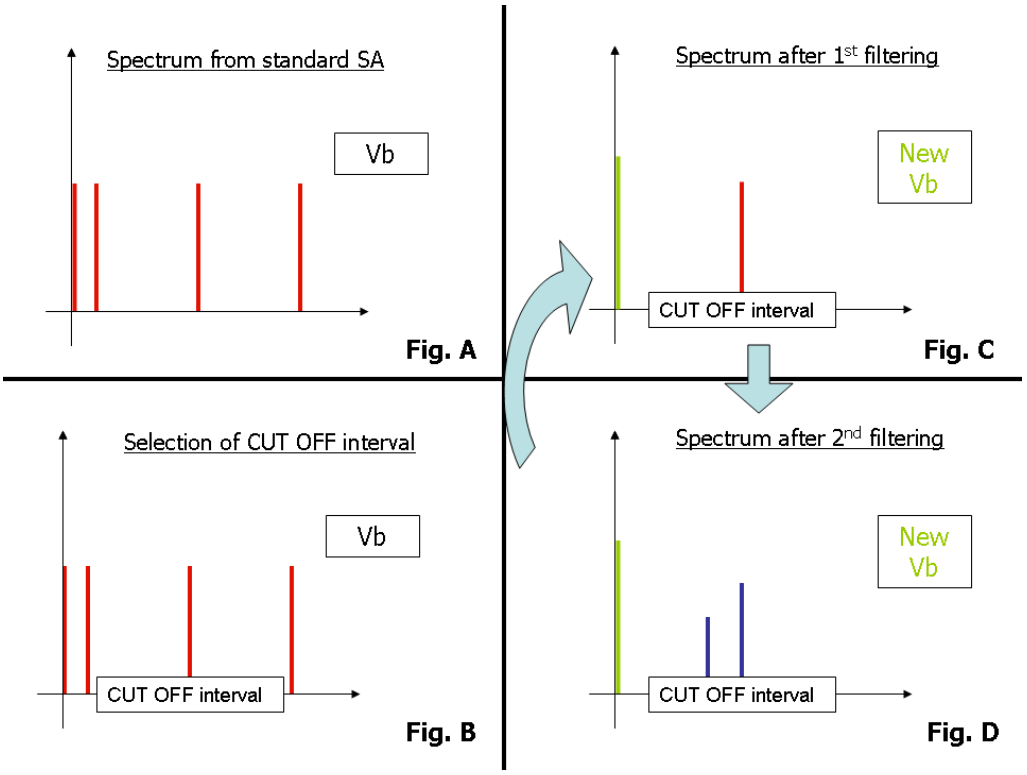

Figure 7.1: The SAIF. (A) The spectrum provided by Cunningham SA method; (B) The choice of the cut-off interval on the evaluated spectrum; (C) *1st filtering:* The contributions of components inside the cut-off interval are subtracted from the data and new values of the trapping and V_b are estimated; (D) *2nd filtering:* The contributions of the trapping and blood volume are subtracted from the data and new values for the components inside the cut off interval are estimated. The iteration cycle is the repetition of the last two points. The WRSS variation provides the stopping criterion.

7.2 The simulation for the SAIF

Before applying the SAIF to acquired data we tested the quality of the algorithm in simulation studies in order to understand its behavior under different conditions. The approach that we used was exactly the same as utilized for the SA with the Turkheimer double filter (Section 6.3). The principal idea on which the simulations were based was to define a dataset as realistically as possible, even though it is impossible to reproduce exactly all the events that contribute to the acquired data.
As in the Turkheimer simulations, the same spectrum, the same variables of interest, the same condition and the same performance indices were used for the tests. We report the results for SAIF simulations in different conditions in the following sections.

7.2.1 Different values for the cut-off interval

As we know from the simulation for the Turkheimer SA this point is crucial for the application of the algorithm in measured data. Our goal is, in fact, to select the cut-off interval that provides the lowest bias and the best distribution of the parameters of interest. To determinate the best solution we used a discrete approach in which we tested different values for the both the endpoints of the cut-off interval. The values were chosen looking for the sampling interval in order to define the slowest and the fastest component detectable from the data. In Figures 7.2, 7.3 and 7.4, and in Figures 7.5, 7.6 and 7.7, we report the estimates for λ and rCPS respectively for different choices of cut-off interval endpoints. As we can see from the results and the graphs, the optimal choice coincides with the narrowest cut-off interval [0.03; 0.3]. A distribution of the components detected with the optimal cut-off choice is reported in Figure 7.8. We can distin-

guish very well the trapping the two equilibrating components of the simulated spectrum. The fastest component is instead due to the presence of the blood that the algorithm is not completely able to separate from true equilibrating components.
We have also tested the SAIF with values for the cut-off interval that do not include the simulated components to understand what happens. The results are better than expected: the algorithm adapts the results to the range of the cut-off interval (Figure 7.9).

Lambda BIAS (%)										
BETA LOWER CUT-OFF (1/min)	BETA UPPER CUT-OFF (1/min)									
	0.1	0.15	0.2	0.25	0.3	0.35	0.4	0.45	0.5	0.6
0.005	5.361	0.518	0.642	0.972	0.981	1.248	1.178	1.309	0.994	1.204
0.010	5.528	0.989	0.176	0.329	0.497	0.447	0.661	0.719	0.761	1.036
0.015	5.527	0.952	0.060	0.233	0.352	0.552	0.559	0.609	0.732	0.727
0.020	5.530	1.221	0.074	0.111	0.174	0.420	0.457	0.466	0.518	0.681
0.025	5.564	1.523	0.204	0.193	0.241	0.357	0.365	0.485	0.471	0.571
0.030	5.519	1.855	0.269	0.057	0.237	0.223	0.352	0.441	0.479	0.495
0.035	5.567	2.194	0.361	0.107	0.088	0.152	0.289	0.361	0.315	0.522
0.040	5.466	2.425	0.455	0.068	0.020	0.020	0.254	0.195	0.298	0.328
0.050	5.507	2.902	0.902	0.292	0.160	0.171	0.045	0.008	0.153	0.111
0.060	5.472	3.151	1.325	0.456	0.293	0.256	0.145	0.140	0.005	0.010

Figure 7.2: λ estimates for the different values of cut-off intervals. The results are means for the 1,000 simulated signals.

7.2.2 Different numbers of betas on the grid

We tested 3 grids with 50, 100 and 200 betas respectively but, as with the Turkheimer method, there were no differences in the means values of the estimates. The grids differ, however, in the distributions of the components that they provide, in the variance in the parameters of interest and in the processing time that they required. We chose 100 as a good compromise between computational time and precision.

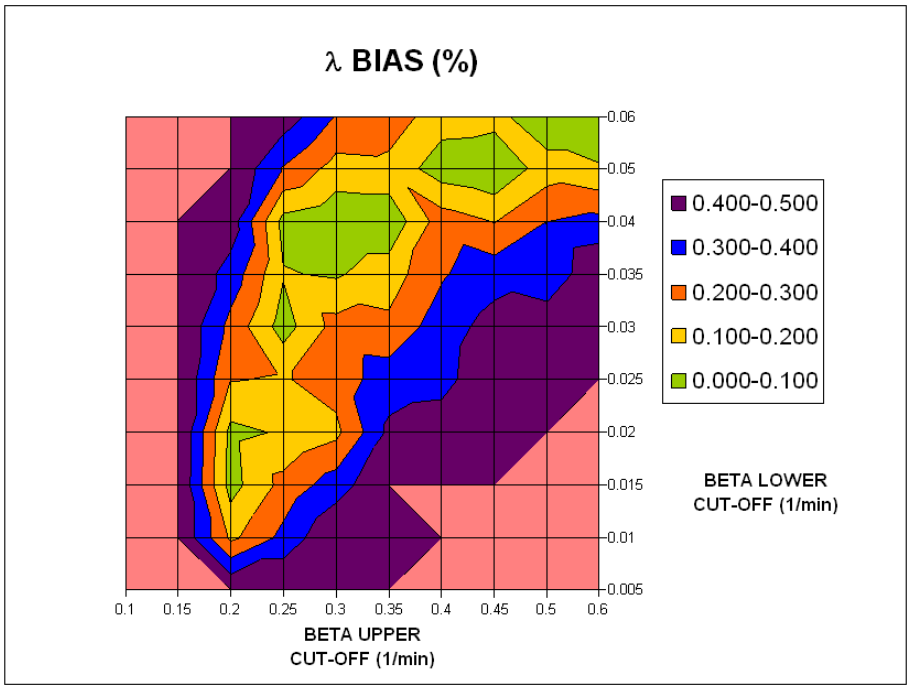

Figure 7.3: Map of λ bias for different cut-off interval choices.

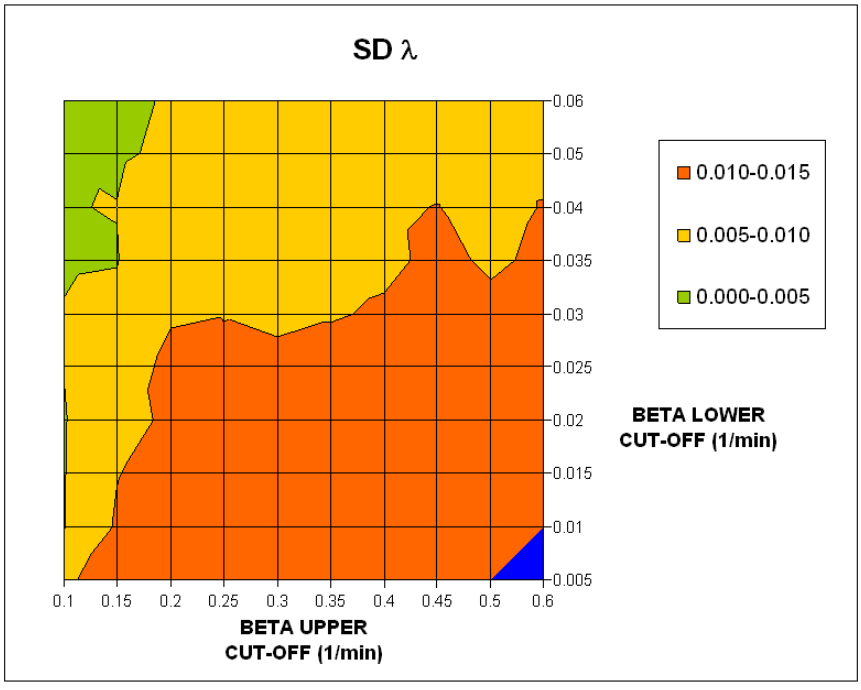

Figure 7.4: Map of λ SD estimates for different cut-off interval choices.

rCPS BIAS %										
BETA LOWER CUT-OFF (1/min)	BETA UPPER CUT-OFF (1/min)									
	0.1	0.15	0.2	0.25	0.3	0.35	0.4	0.45	0.5	0.6
0.005	5.82	3.57	4.96	4.95	4.30	5.53	4.43	4.97	3.67	4.02
0.010	6.65	1.41	2.74	1.69	1.86	1.43	2.23	2.34	2.37	3.32
0.015	6.64	1.42	2.05	1.00	1.10	1.43	1.48	1.29	1.96	1.71
0.020	6.69	0.04	1.40	0.36	0.12	1.32	1.13	1.11	1.16	1.62
0.025	6.79	1.76	0.63	0.87	0.64	0.58	0.60	0.65	0.83	1.10
0.030	6.60	3.43	0.18	0.08	0.47	0.03	0.35	0.57	0.80	0.28
0.035	6.76	5.20	0.22	0.91	0.51	0.56	0.29	0.17	0.39	0.35
0.040	6.44	6.44	0.84	0.79	1.01	1.31	0.25	0.89	0.49	0.54
0.050	6.56	9.19	3.14	2.31	2.12	2.36	2.04	1.93	1.73	1.82
0.060	6.46	10.39	5.32	3.37	3.10	3.31	3.24	3.04	2.74	2.91

Figure 7.5: rCPS estimates for the different values of cut-off intervals. The results are means for the 1,000 simulated signals.

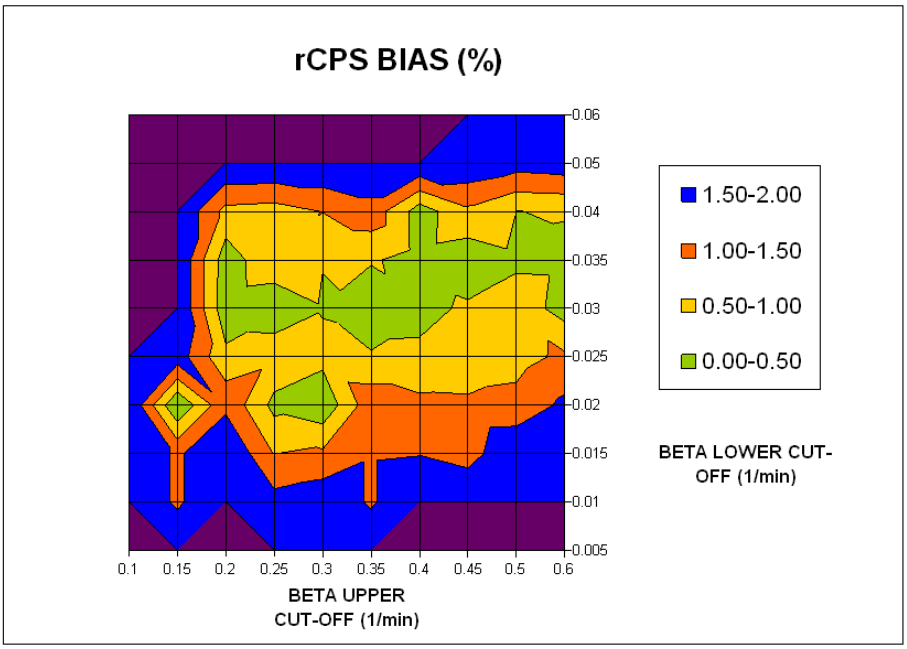

Figure 7.6: Map of rCPS bias for different cut-off interval choices.

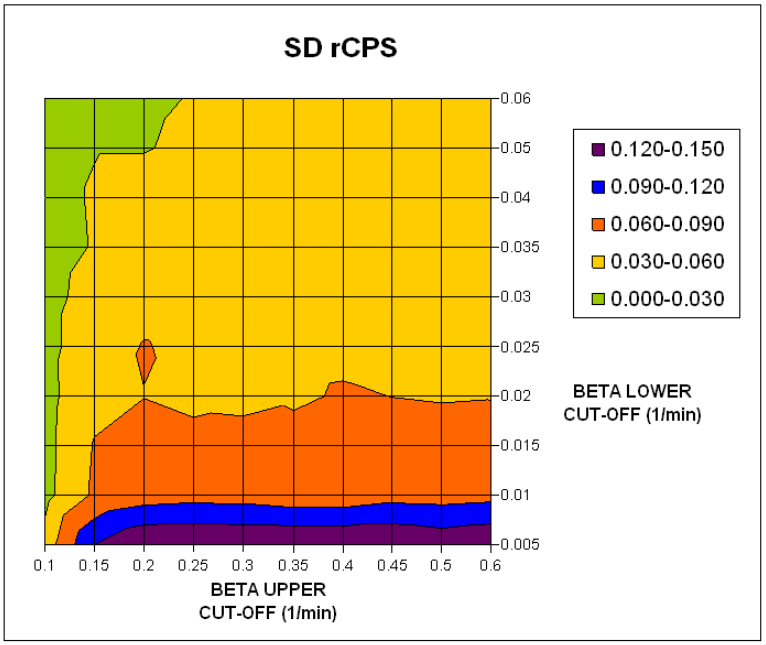

Figure 7.7: Map of rCPS SD estimates for different cut-off interval choices.

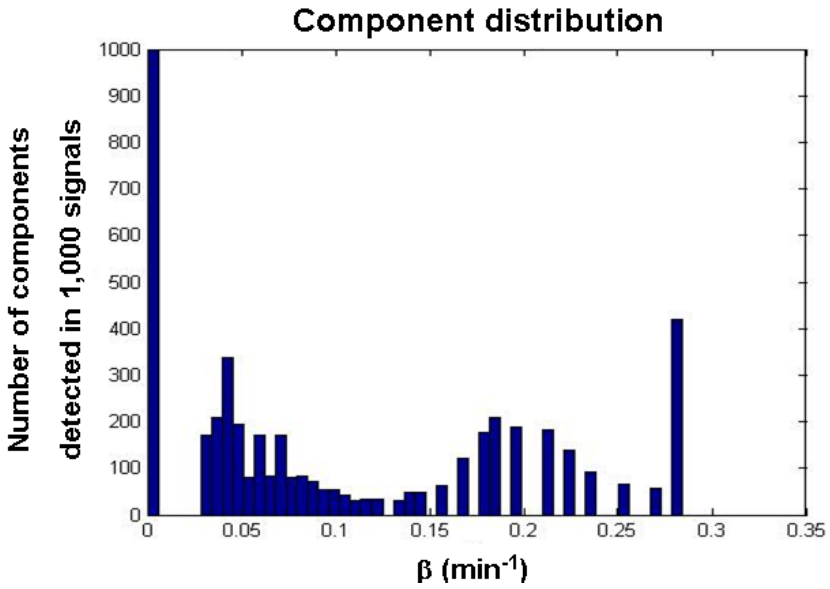

Figure 7.8: Distribution of the spectral components with the optimal choice of the cut-off interval. The simulated components are $[\alpha_0 = 0.01\ ;\ \beta_0 = 0.00]$, $[\alpha_1 = 0.01\ ;\ \beta_1 = 0.05]$, $[\alpha_2 = 0.04\ ;\ \beta_2 = 0.20]$ and $V_b = 0.05$.

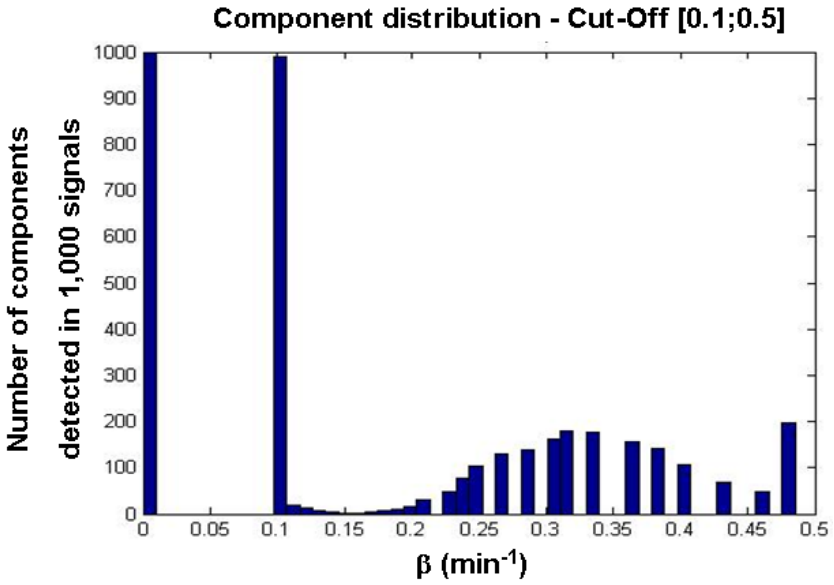

Figure 7.9: Distribution of the spectral components with bad choice of the cut-off. In this case one of the equilibrating components (the slowest $\beta = 0.05$ min^{-1}) is not included in the cut-off interval and the algorithm reacts detecting in each simulation the slowest possible equilibrating component located at $\beta = 0.1$ min^{-1}.

7.2.3 Different noise levels

In Figure 7.10 we report the estimates using a 100-betas grid and the optimal choice for the cut-off interval. The results provide acceptable bias for all noise levels (Equation 3.5) consistent with those estimated for ROIs in the human brain (range N=0.15 to N=1.0), and are indeed better than the ones provided with the Turkheimer filter. We tried also a very high scale for variance for the noise, N=15, to simulate noise which approaches to the noise in voxel data, but the results were unsatisfactory (bias $> 100\%$). It is our opinion that to apply SAIF with high noise levels something has to be changed, for example, introducing a data pre-filtering in order to smooth the signals.

	λ		rCPS (nmol/g/min)			FIT	Computation al time
Scale for Variance	mean	SD	mean	SD	BIAS (%)	WRSS	
SIMULATED VALUES (N)	0.833	^^	0.887	^^	^^	^^	
0.15	0.833	0.004	0.893	0.024	0.7	0.8	9.90 min
0.30	0.834	0.006	0.892	0.032	0.6	3.2	12.4 min
0.50 (mid level of noise)	0.835	0.009	0.887	0.050	0.1	8.6	14.0 min
0.80	0.837	0.015	0.878	0.074	0.9	22.2	14.0 min
1.00	0.837	0.018	0.872	0.083	1.7	34.6	13.5 min
1.50	0.841	0.027	0.845	0.120	4.7	78.7	12.2 min

Figure 7.10: λ and rCPS estimates for different noise values. The results are mean $\pm$ SD for the 1,000 simulated signals.

7.2.4 Considerations

Looking at the simulation results we find the following considerations:

- The number of betas used influences more the computational cost than the distribution of detected components. Although there is always the presence of very fast phantom components, these are due to the underestimation of V_b and not to the number of the betas in the grid. We obtained identical results for 50, 100, 200 betas.

- At the Noise level typical of ROI data, biases are small ($< 1\%$) and precision reasonable (CV $< 2\%$).
- The choice of cut-off interval is fundamental: the bias and accuracy of the parameters estimates depend on the cut-off choice. We found a set of cut-off values that provided high accuracy and very low bias in the parameter estimates.
- The new method leads to a good fit with reasonable increase of computational time (4-5 secs per estimation) compared to the standard SA techniques.

Even though the results of the simulation with SAIF are good, we must compare SAIF to the other SA algorithms in order to understand which is the best SA approach for quantifying rCPS.

7.3 The comparison among the SA algorithms

7.3.1 The comparison

To test the different capacity of SA for quantifying the variables of interest in the leucine PET data, we used the same simulation approach defined for the SAIF and the Turkheimer SA. 1,000 signals, generated from the same spectrum (Section 6.3), have been tested, with the following 5 different SA techniques:

1. Cunningham SA **(NFFG)**
2. Cunningham SA with the beta grid truncated so the upper and the lower bounds match the optimal cut-off interval for SAIF **(NFSG)**
3. Turkheimer double filter SA **(SF)**
4. SAIF without doubling correction **(RF)**
5. SAIF with doubling correction **(RFDC)**

The reasons for why we applied methods 2 and 4 were different. The NFSG was introduced to emphasize that truncating the beta grid without filtering the data is not a sufficient for obtaining good estimates. The RF, i.e. SAIF algorithm without the doubling correction, was used instead to show that the doubling correction has no influence on the estimates as we have explained (Section 4.3). In Figure 7.11 we compare the different fits of the simulated data. The weighted residual trends obtained from the curves of Figure 7.11 with the simulated data are reported in Figure 7.12. In Figure 7.13 and 7.14 we compare the estimates of the variables of interest K_{Patlak}, K_1, V_b, λ and rCPS. Figure 7.15 provides an idea of the variability of the parameters among the 1000 simulation cases with the different methods. In Figure 7.16 we report the bias of the estimated variables.

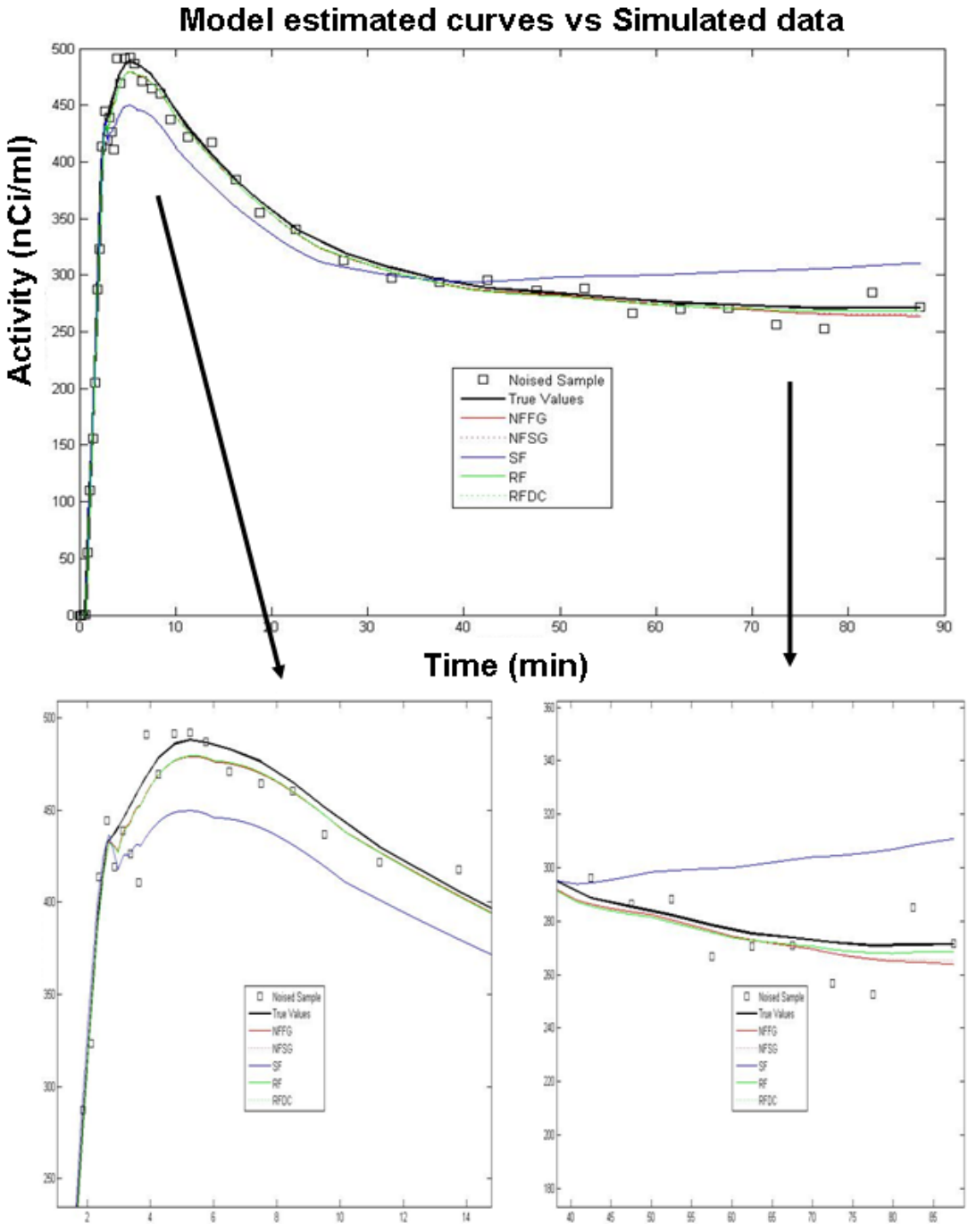

Figure 7.11: SA estimated curves compared with the simulated noise signals.

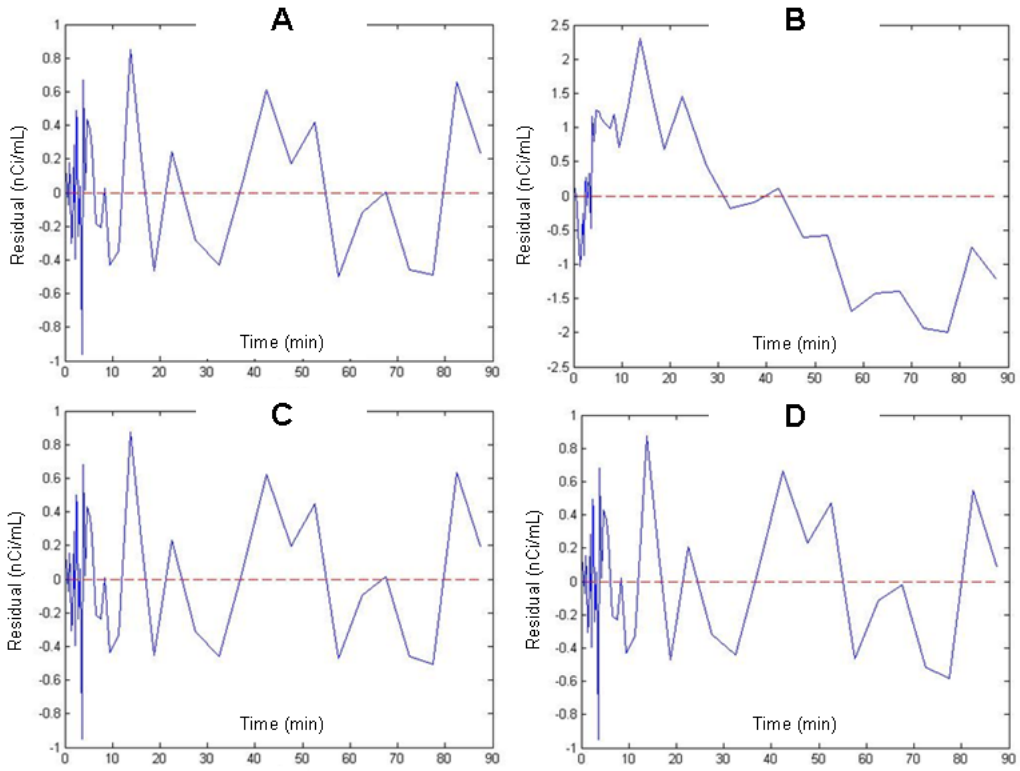

Figure 7.12: Weighted residual trends from the different SA methods: (A) Cunningham standard SA (NFFG); (B) Turkheimer SA (SF); (C) Cunningham SA with truncated beta grid (NFSG); (D) SAIF methods (RF and RFDC).

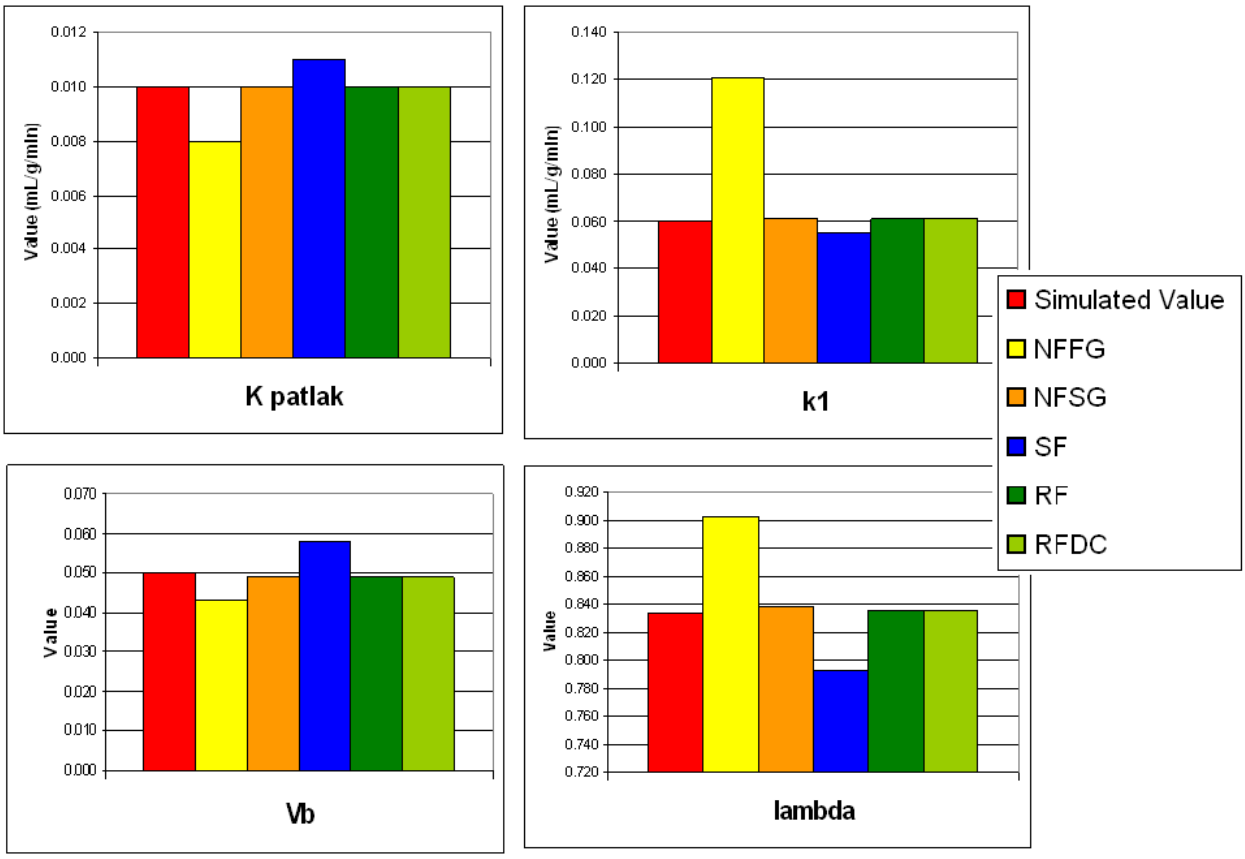

Figure 7.13: Estimate comparisons between the 5 SA methods and the simulated variables.

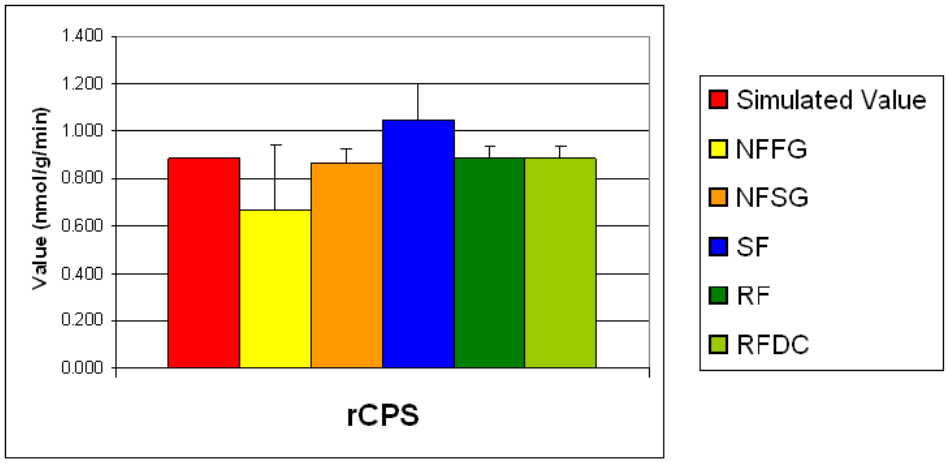

Figure 7.14: rCPS estimate comparisons between the 5 SA methods and the simulated variables.

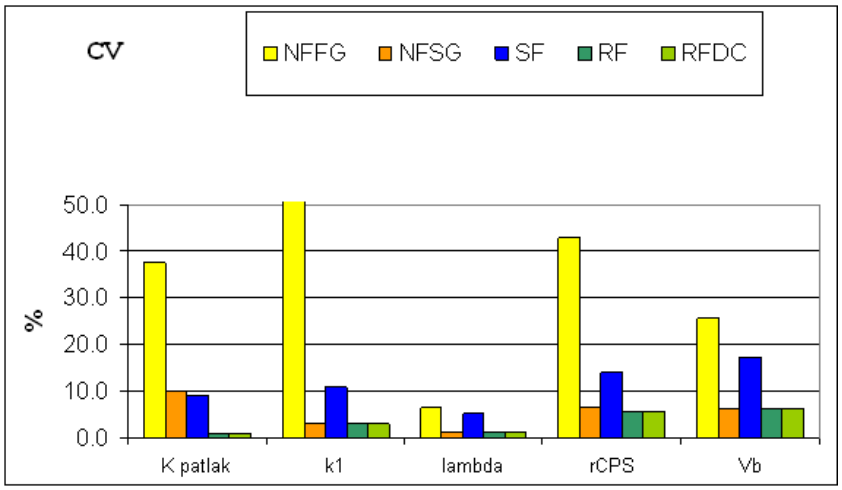

Figure 7.15: Coefficients of variation in all variables of interest for each the SA methods examined.

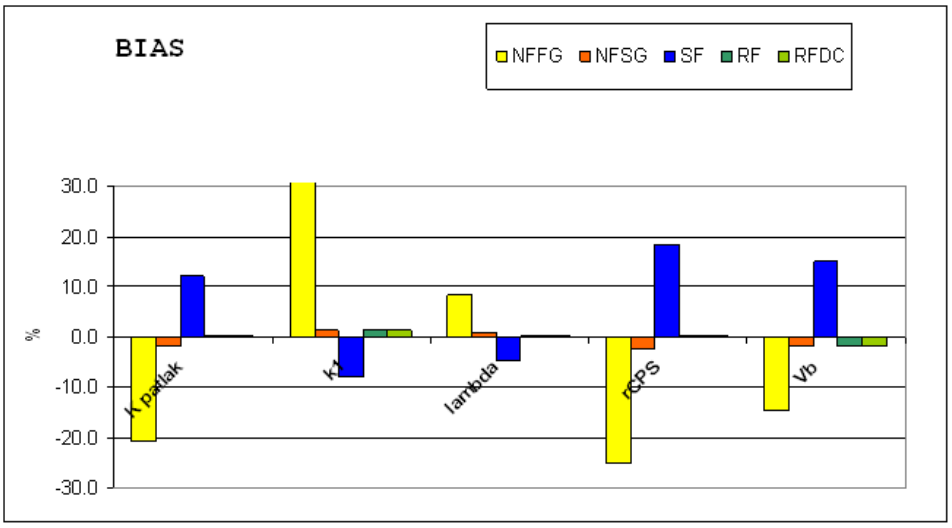

Figure 7.16: Bias in all variables of interest for each the SA methods examined.

7.3.2 The results of comparison

FIT

From Figure 7.11, we can see again the typical behavior of the different SA methods. In particular, the poor fit of the data by the Turkheimer SA method (blue line). The other approaches provide good descriptions of the simulated data, even though the SAIF-based method (RF and RFDC) are better than the Cunningham-based methods (NFFG and NFSG).

Weighted residual trends

As we have explained in Chapter 4, this representation provides an idea about the goodness of the estimation method. All SA techniques (Figure 7.12), except the Turkheimer approach, present the expected random behavior in the residuals.

The estimates for the variables of interest

In Figure 7.13 and 7.14 the orange bar (NFSH) and the green bars (RF and RFDC) have a very good match with the simulated values in all the variables of interest. In particular, for rCPS quantification, these three methods provide the same estimates with comparables errors. The yellow bar (NFFG) and the blue bar (SF) do not have this characteristic, and for all the variables they provide poor estimates. These methods correspond to the Cunningham SA and the Turkheimer SA with double filter and hence these results again confirm what we have reported in the previous chapters.

Variability in the estimates: The Coefficient of Variation

Figure 7.15 reports a graphic representation of the precision that the methods have in the examined variables. The worst results correspond to the Cunningham SA (NFFG) and Turkheimer method (SF). The best results are provided by the SAIF algorithms (the green bars) which are significantly better that the others. The orange bars related to the Cunningham SA with a truncated beta grid (NFSF) has comparable values with the SAIF for all variables except Kpatlak. This is a logical consequence of the lack of a correction of the trapping component in the Cunningham algorithm.

Bias in the estimates

Figure 7.16 represent the goodness of the estimates for the different methods by comparing the bias. As we can see from the bar graph, the Cunningham SA (NFFG) and Turkheimer SA (SF) provide the most underestimated and overestimated results, respectively. The others methods have low bias although the SAIF methods (RF and RFDC) are visibly better than the Cunning-

ham SA method define with a truncated beta grid (NFSG) for K_{Patlak}, λ and rCPS.

7.3.3 FINAL CONSIDERATIONS FROM THE COMPARISON

From the results that we conclude that the SAIF correction is the best of the five SA methods analyzed for the quantification of rCPS in leucine PET data. In fact, it is characterized by the lowest bias, the best fit of the simulated data, a reasonable residual trend and a good accuracy on the parameter estimation. The simulation studies also demonstrate that there are not any notable different in the estimates provided by the SAIF with and without the doubling correction. This means that our approach for the elimination of the double components works in the way that we wanted because it resolves the problem of the doubling without compromising the quality of the results.
Interesting are the results provided with the Cunningham SA method defined on a truncated grid of betas (NFSG). The results are considerably better than the standard Cunningham method (NFFG) but not as good as the SAIF (RF, RFDC). This suggests that the beta grid choice is very important for determining the quality of the results, but it is not the only feature to take into account.
The most important problem of SA is related to the absence of a criterion based on the data for the choice of cut-off interval. In the next section, we present the method that we used to set-up the SAIF algorithm for the analysis of our acquired data.

7.4 The choice of cut-off interval

The lack of a data-driven criterion for the choice of the cut-off interval could be an important limitation for the SAIF utilization. The method, as we have explained, consists of defining a dataset of simulated signals very close to the measured data, trying different cut-off values in order to decide the best solution, and finally applying the selected cut-off interval to the acquired data. But this strategy is dependent on having realistic knowledge of the kinetics of the measured data. As the underlying kinetics are not known we have had to rely on estimates of the kinetic parameters provided by other analysis methods.
To define a more data-driven method we considered whether the SD values of estimated parameters could help to make a decision on the optimal cut-off interval. First, however we had to solve the problem of finding a good method for SD evaluation. We know that the inverse of Jacobian Information matrix provides a lower bound for the variance of the matrix (Section 4.3). For the estimation of SD we compared, in a bootstrap simulation, three different approaches:

- SD "true value"estimated from the variables of interest distributions;
- Linear Approach[3]: Jacobian inversion in SA linear model;
- Non Linear Approach[4]: Jacobian inversion in SA non linear model (betas included);

The simulation was organized in this way: we defined a noisy TAC signal, and we estimated the parameters of interest with

[3]The linear approach refers to the SA model (Section 4.3) in which only the αs and V_b are the parameters of the model and the βs are fixed.

[4]The non linear approach refers to the same model as the linear approach but in this case βs are not considered fixed but variables of the models. In this way the equation associated with the model is a non linear function of the parameters (αs, βs, V_b).

SAIF as usual. Then, using the weighted residual difference between the estimated curve and the simulated data, we defined 1,000 realization of the same signal with a bootstrap[5] technique. Each signal was processed with SAIF and the SD with the linear and non linear approach was estimated. At the end of this elaboration we had three groups of values: 1000 estimated variables of interest, 1000 SD values from the linear approach and 1000 SD values from the non linear approach. The SD calculated from the distribution of the estimates represented what we called "the true value"and the averages from the other two groups were the SD with linear and non linear approach, respectively. In Figure 7.17 we report the comparison of these three groups for all the variables of interest. As we can see the linear approach underestimates the true values, and the non linear approach overestimates them to a considerably higher degree. In light of these results, we decided that the best way to define the precision for the estimates is through the inverse Jacobian matrix based on the linear model.
Even though this discussion about the best method to estimate SD is interesting, it was not found to be helpful for the problem of the cut-off interval choice as elaborated below. In fact, the optimal choice has to be a compromise between least bias and best precision for the parameter estimates. These two factors work in an opposite way, so if we consider only the SD for the cut off we will produce estimates with very good precision but very large bias.

[5]In statistics, bootstrapping is a modern, computer-intensive, general purpose approach to statistical inference, falling within a broader class of resampling methods. Bootstrapping is the practice of estimating properties of an estimator (such as its variance) by measuring those properties when sampling from an approximating distribution. One standard choice for an approximating distribution is the empirical distribution of the observed data. In the case where a set of observations can be assumed to be from an independent and identically distributed population, this can be implemented by constructing a number of resamples of the observed dataset (and of equal size to the observed dataset), each of which is obtained by random sampling with replacement from the original dataset [9].

Let us to consider for a moment the Bayesian estimation method. The results depend on a regularization parameter (γ) that weights *a priori* and *a posteriori* information on the variables that we want to estimate. It is not our interest now to explain how this algorithm works, but what is important is the role of γ. The choice of this regularization parameter is affected, as is the choice of the cut-off interval, by the problem of finding the optimal value that is the best trade-off between prior assumptions and data analysis. If γ is unbalanced towards one of these two sides, the estimates have too much bias or too much variability, respectively. The equation to determinate the best choice of γ takes into account the statistical distribution of the error in the data and the prior information about the data. If we consider the cut-off interval as the correspondent of γ in the SA, the criterion for its choice has to be defined in the same way. Thus we reasoned that we could not use SD for defining a data-driven choice of cut-off interval. For the moment the approach based on the simulation is the only method that we have for choosing the cut-off interval.

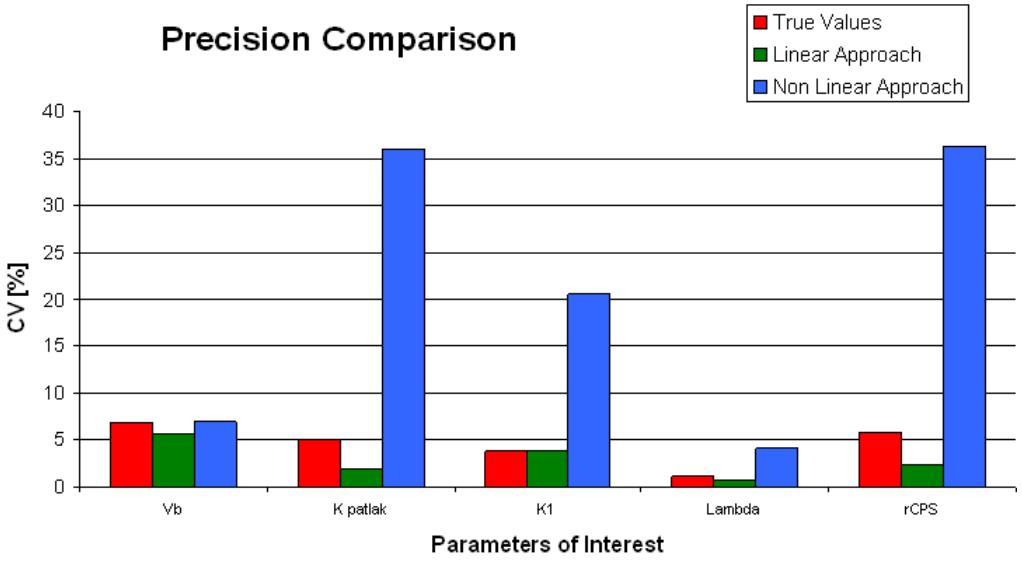

Figure 7.17: Different methods for the estimation of precision of the variables of interest. Instead of the SD the CV = SD/(simulated value) is reported here in order to have the same normalized view of all the parameters.

7.5 Final consideration about the SAIF

The Spectral Analysis Iterative Filtering, that we have defined and tested in simulation studies, seems to be the best Spectral Analysis algorithm for the quantification of rCPS in leucine PET data. Even though these preliminary results can not be completely sufficient to establish if SAIF is or is not a valid quantification method, we can conclude that the innovative features of the method, in particular the presence of the iterative cycle filter, improve the estimate quality compared to the other SA techniques.
The reason for this is due to a better estimation of the spectrum that the SAIF provides from the data. If we consider the spectrum estimated with the three principal SA methods (Cunningham SA, Turkheimer SA, SAIF) (Figure 7.18) we can see that the new algorithm gives a better approximation of the simulated spectrum. In particular, it conserves multiple equilibrating compartments that are due to the tissue heterogeneity, which are absent in Turkheimer SA or not consistent with the data assumptions[6] in Cunningham SA. We report a graphic representation of the spectrum in Figure 7.19. It is interesting to see that the lowest simulated equilibrating component is detected only by the SAIF even though the fastest one is better represented by the Cunningham and Turkheimer method. Also the sum of the estimated αs, which is equivalent to the parameter K_1^* (Equation 6.15), is better estimated by the SAIF method compared to the other methods.
Thus we can se that SAIF produces better estimates of the spectrum that Turkheimer SA or Cunningham SA methods. It is, therefore, not surprising that it provided better estimates of the

[6]In Cunningham SA the fastest component is located at $\beta = 1.26$ min^{-1}. This value is too high compared to the fastest detectable component in the leucine PET data and for this reason it is not realistic.

macro parameters of the system, i.e. rCPS and λ, as shown in the previous section. The SAIF presents also some disadvan-

Simulated		SAIF		Turkheimer SA		Cunningham SA	
beta	alpha	beta	alpha	beta	alpha	beta	alpha
0.00	0.010	0.00	0.010	0.00	0.012	0.00	0.012
0.05	0.010	0.04	0.004	0.15	0.042	0.15	0.042
0.20	0.040	0.14	0.032			1.26	0.019
		0.28	0.014				
Sum of α (K1)*	*0.060*		*0.060*		*0.054*		*0.073*

Figure 7.18: The spectra provided with SAIF, Turkheimer SA and Cunningham SA from a simulated signal.

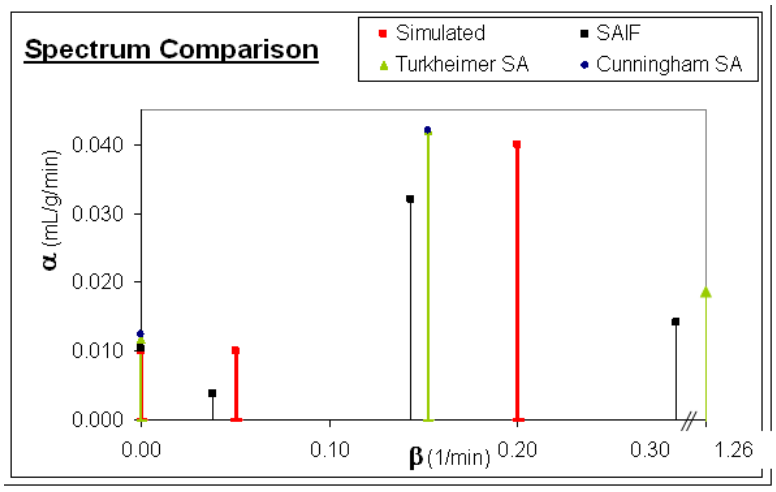

Figure 7.19: Three spectra estimated with Cunningham SA, Turkheimer SA and SAIF, respectively. The estimates are compared with the simulated value.

tages. The most important is related at the choice of the Cut-off interval that conditions directly the quality of the estimates. A data-driven criterion is lacking but for our data we have found a method to define it that provides useful results. The SAIF, as the other spectral techniques, is also characterized by a low estimate precision compared to the compartmental-model based method. This is most probably due to the high number of parameters that SA uses, and thus it is unavoidable when we apply

the method.
To finally evaluate the qualities of SAIF we tested it on measured data. The estimates were compared with the results of the other two methods previously used to analyze leucine PET data: using NLLS to estimate parameters of the homogenous tissue kinetic model at the ROI level [2] and using a Basis Function method to estimate parameters of the homogenous tissue kinetic model at voxel level [35]. The latter method is summarized in Chapter 8.

Chapter 8

The Basis Function Method (BFM)

8.1 A method for rCPS estimation at voxel level

In this section we describe the BFM and the way in which we used it to estimate rCPS at ROI level.

8.1.1 Introduction to the BFM

As we have seen (Section 3.4), the NLLS applied to HOM for the rCPS estimation from the leucine PET data is affected from the incapacity of the kinetic model to take in account the heterogeneity in the tissues. The application of the NLLS to the HET, instead, could represent better the mixture of the tissues present in the ROI but it has characterized by convergence problems. Additionally NLLS algorithms have a high cost that prevents their being used at voxel level. It is for this particular reason that BFM has been developed [35].
BFM is a very fast method defined to estimate the variables of interest, which, due to its speed, is practical to apply at voxel level. This approach is based on the same homogenous tissue kinetic model defined for the leucine (Equations 3.1, 3.2), but it

differs to the NLLS-HOM method in the algorithm that it uses for rate constant estimation. It is important to emphasize the differences between the NLLS-HOM and BFM because there are three aspects that interact:

1. the estimation algorithm;
2. the kinetic model used to represent the data;
3. the level to which the method is applied (ROI or voxels).

In light of these aspects the BFM can be also elaborated as BFM-HOM-VOXEL. This means that the Basis Function Method algorithm is applied with the HOM model to estimate the variables of interest from the voxel TACs. The NLLS-HOM is different. It applies a non linear estimation algorithm to estimate rCPS at ROI level through a homogenous kinetic model. So from these definitions it is easy to notice that BFM and NLLS-HOM differ for the estimation algorithm that they used and for the TACs to which they are applied.
From BFM-HOM-VOXEL it is also possible to calculate rCPS and at ROI level simply by averaging the results of the estimates among all voxels within the ROI. This approach is substantially different than applying BFM directly to estimate parameters from ROI time-activity curves because tissue heterogeneity is likely to be far greater within a ROI than within a voxel. Starting with BFM estimates at the voxel level and averaging to obtain values at the ROI level is an alternative approach to NLLS and SA for estimating rCPS in the different regions of the brain.

8.1.2 Fundamentals

To understand the BFM method let us to consider again the measurement equation associated with the HOM (Equation 3.2). This equation relates the total concentration of ^{11}C (C_T^*) in a

generic voxel at time t to the measured $[^{11}C]$leucine concentration in plasma (C_p^*), total ^{11}C in whole blood (C_b^*), and $^{11}CO_2$ concentration in tissue ($V_D C_c^*$) as follows:

$$\begin{aligned} C_T^*(t) &= (1 - V_b) \cdot [\left(\tfrac{K_1(k_2+k_3)}{k_2+k_3+k_4}\right) \int_0^t C_p^*(\tau) e^{-\beta(t-\tau)} d\tau \\ &+ \left(\tfrac{K_1 k_4}{k_2+k_3+k_4}\right) \int_0^t C_p^*(\tau) d\tau \\ &+ V_D C_c^*(t)] + V_b C_b^*(t) \end{aligned} \tag{8.1}$$

where

$$\beta = k_2 + k_3 + k_4 \tag{8.2}$$

Equation 8.1 can also be written as:

$$\begin{aligned} C_T^*(t) &= \Theta_1 \int_0^t C_p^*(\tau) e^{-\beta(t-\tau)} d\tau \\ &+ \Theta_2 \int_0^t C_p^*(\tau) d\tau \\ &+ \Theta_3 [C_b^*(t) - V_D C_c^*(t)] + V_D C_c^*(t) \end{aligned} \tag{8.3}$$

with

$$\Theta_1 = (1 - V_b) \left(\frac{K_1(k_2 + k_3)}{k_2 + k_3 + k_4}\right) \tag{8.4}$$

$$\Theta_2 = (1 - V_b) \left(\frac{K_1 k_4}{k_2 + k_3 + k_4}\right) \tag{8.5}$$

$$\Theta_3 = V_b \tag{8.6}$$

If the value of β were known, Equation 8.3 would linear in the parameter vector $\Theta = [\Theta_1, \Theta_2, \Theta_3]$ which could be quickly estimation using the standard linear estimation method, i.e. the Weighted Linear Least Squares (WLLS). The WLLS, unlike NLLS, doesn't require an iterative algorithm for the solution, but utilizes a direct formulation that reduces drastically the computational time for the estimation. The idea of the BFM

is to define a grid of values for β in the physiological range, β_1, β_2, ..., β_m, solve for each of them the corresponding linear problem expressed by Equation 8.3, and then select the value β^* which produces the smallest residual sum-of-squares[1]. Let $\Theta^* = [\Theta_1^*, \Theta_2^*, \Theta_3^*]$ be the estimated parameter vector at $\beta = \beta^*$. Equations 8.4-8.6 can then be solved to yield the final values of the rate constants (K_1, $k_2 + k_3$, k_4) and blood volume (V_b) as

$$K_1 = \frac{\Theta_1^* + \Theta_2^*}{1 - \Theta_3^*} \tag{8.7}$$

$$k_2 + k_3 = \frac{\Theta_1^* \beta^*}{\Theta_1^* + \Theta_2^*} \tag{8.8}$$

$$k_4 = \frac{\Theta_2^* \beta^*}{\Theta_1^* + \Theta_2^*} \tag{8.9}$$

$$V_b = \Theta_3^* \tag{8.10}$$

Unfortunately, Equations 8.7 - 8.10 may provide one or more negative parameter estimates for a given voxel, while all rate constants and V_b should be nonnegative. The introduction in the estimation algorithm of a non-negative constraint would increase substantially the computational time, and processing speed, which is the most important feature of BFM, would be lost. Rather than do this or exclude these voxels from the analysis, which would likely create problems when considering ROI/voxel correlation, doctor Giampaolo Tomasi, of Yale University, developed a strategy (Appendix D) to reanalyze each voxel that had one or more negative parameters after the initial BFM estimate. Only if non-negative parameter estimates could not be achieved after reanalysis was a voxel discarded from further considerations. For our dataset, 100 values equally spaced between 0.0001 min^{-1} and 0.5 min^{-1} were used as the predefined

[1]It is not necessary to use other kind of comparison indexes as the AIC to chose β^* with the model does not change. In this way the information of WRSS reflects exactly the information provided by AIC.

grid for β, as this widely covers the range of physiological values expected for $k_2 + k_3 + k_4$.
The choice of the number of βs in the fixed grid is an important parameter for the BFM algorithm. In fact, if the grid was very density populated of beta, the estimate result could be more accurate but in the same time the computational time would increase considerably. The determination of the number of betas is very similar problem to the decision of the length of the component grid in SA. The choice of 100 βs is a good compromise between the computational efficiency and estimate precision.

8.1.3 BFM for estimation at ROI level

Even though the BFM is based on the homogenous kinetic model in the same way as NLLS-HOM technique, the estimates provided by the two methods for the ROI level are different. The reasons of this behavior are due to the different approaches that BFM applied to the voxel level and NLLS applied to the ROI level use to calculate the variables of interest for the different regions. In Figure 8.1 a representation of the different paths used by the methods is shown. The NLLS-HOM method follows the direction indicated from the red arrows. Before the estimation, voxel time-activity curves are averaged in a single signal. This signal represents the time-activity curve associated with the ROI. From this the variables of interests are estimated through the NLLS based on the homogenous tissue kinetic model.
The BFM, instead, uses the opposite approach (violet line). Firstly the estimates of the variables of interest for all the voxels are provided using for each time-activity curve the BFM approach. Secondly by averaging the results the estimates at ROI level are calculated. Even though the red and the violet paths of Figure 8.1 both arrive a ROI-level estimates, the methods

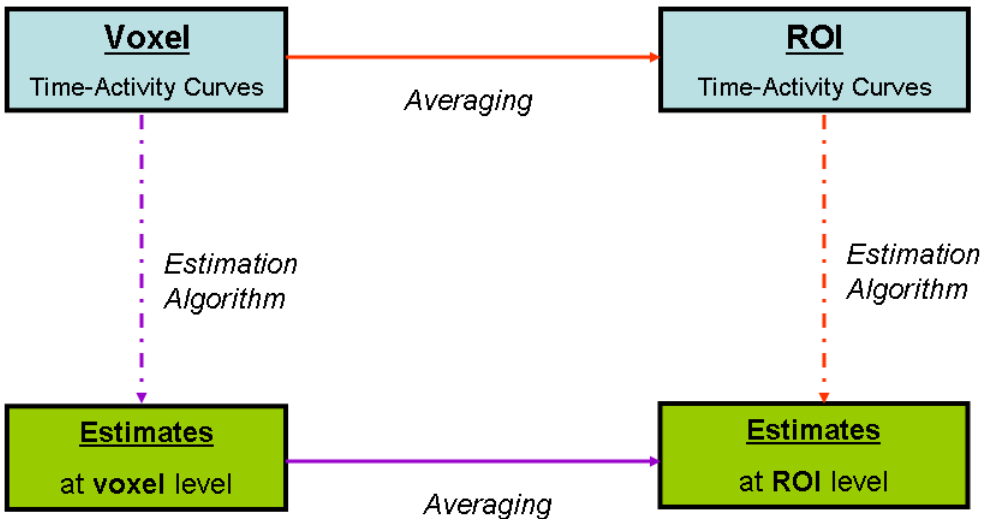

Figure 8.1: The estimation paths in NLLS-HOM-ROI (red line) and BFM-HOM-VOXEL (violet line).

that they represent are not equivalent. In fact, although BFM and NLLS use the same model we expect different results due to the heterogeneity contained inside the signals in which they are applied. To understand this let us to focus the attention on the different volumes that a voxel and a ROI refer to. Reconstructed voxels for scans conducted on the HRRT have a volume of $\sim$1.8 mm^3. A ROI instead is generally made up of thousands of these elements and so the volume that it represents is larger by several orders of magnitude. In accordance with this feature, the mixture of tissues that a voxel contains cannot be compare with the variability present in a ROI. If the heterogeneity is so different, it is evident that the descriptions of the systems, at the voxel and ROI levels, provided by the homogenous kinetic model can not be the same. Consequently we expect that the HOM works better where the system is more homogenous, i.e. at voxel level. From these considerations the BFM applied at the voxel level seems to be a better instrument to estimate the variables of interest. The fit of the TACs elaborated from the results of the estimations in measured data could suggest some-

thing about this hypothesis.
All these considerations are based on one of the two differences that BFM and NLLS-HOM have, i.e. the kind of TAC to which the methods are applied. The other difference, regarding the algorithms that BFM and NLLS used for the estimations, does not condition the estimates but only the speed of the algorithm [35]. In fact, simulation experiments showed that NLLS and the linear approach with the fixed grid of betas of BFM can be considered equivalent [35].

8.1.4 Application of BFM in simulation and real data

Before applying the method to the measured data, BFM was tested and compared with NLLS in simulation experiments at voxel and ROI level. The simulation [35] shows a good agreement when BFM and NLLS are applied to the voxel TACs. The results at ROI level, calculated by the two methods described above, are instead very different. In particular, what is different is the bias of the methods (Chapter 9). For the NLLS applied at the ROI level the range is 15-20% whereas the BFM bias range is 0-7%.
After these tests on simulated data, BFM was applied the acquired data of our subjects [35]. The results are reported in the next chapter where they are compared to the others provided by NLLS at the ROI level and spectral analysis.

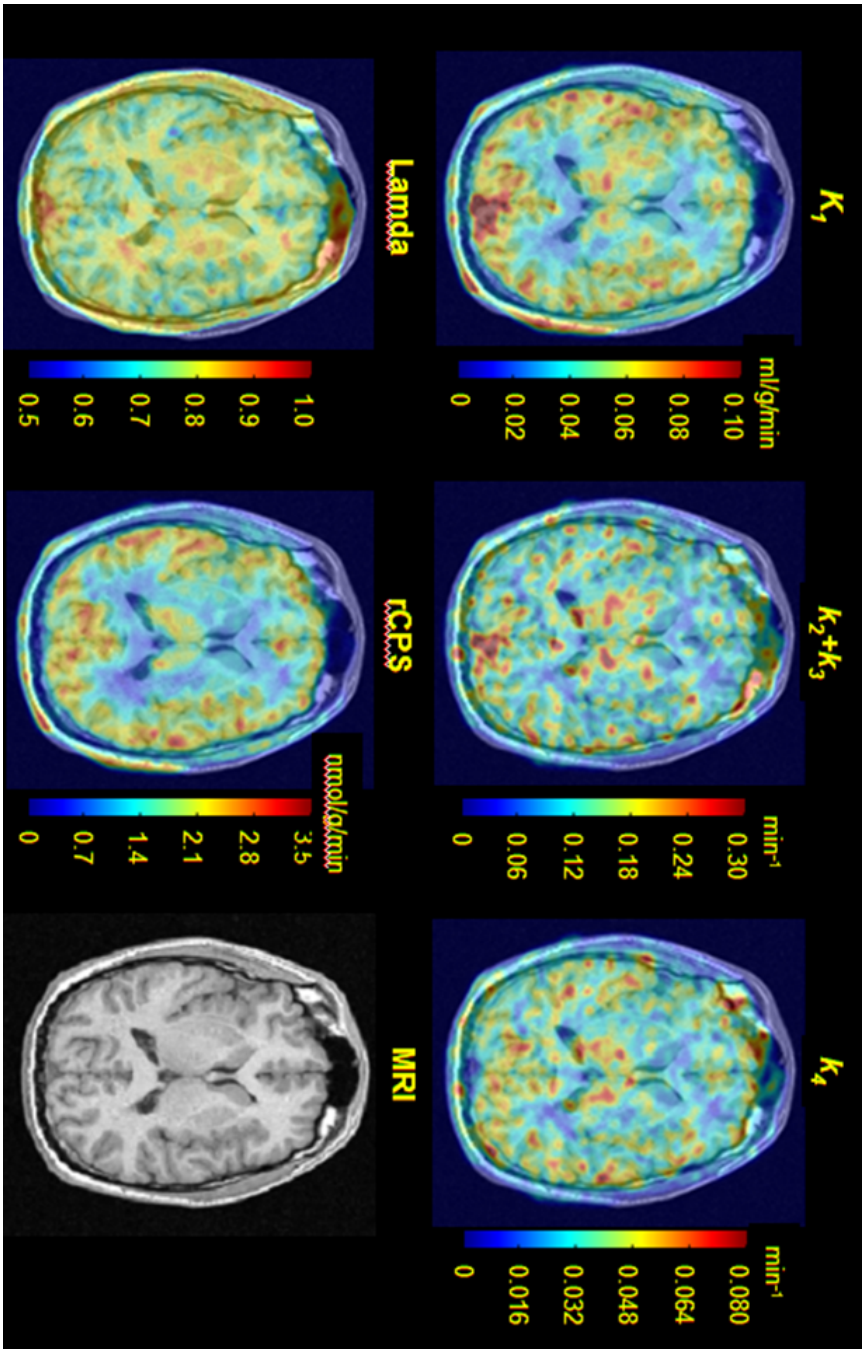

Figure 8.2: BFM estimates at voxel level. From these results the method can provide also the estimates at ROI level by averaging the parameters values among all the pixels of the ROI.

Chapter 9

Quantification in measured data - Comparison of the new Spectral Analysis algorithm SAIF with previously established methods

In this chapter we report the results for the rCPS estimation at ROI level using all the available quantification methods that we have discussed in the previous sections: the NLLS based on the homogenous tissue kinetic model and applied at the ROI level (Chapter 3), the Basis Function Method based on the homogenous tissue kinetic model and applied to voxel level (Chapter 8), and our Spectral Analysis algorithm SAIF (Chapter 7) applied to the ROI level.

In Figure 9.1 the rCPS averages among the 9 subjects are shown for all the regions of interest. The SD represents the intersubject variability. From these results we can see that BFM and SAIF are in good agreement, although SAIF values tend to be slightly lower. Values for NLLS-HOM are considerably higher. This is consistent with what we know about the bias of the methods. Recently studies [35] demonstrated that NLLS applied to HOM at the ROI level overestimates the rCPS by

about 15-20%. The BFM instead, tends to underestimate the data, but, the bias is lower (at most 5%), and for some ROIs, such as the white matter, it is very close to zero. Our simulation studies show that the SIAF has a behavior similar to the BFM. In fact, SAIF underestimates the rCPS, with an average value of 2-3%.

From Figure 9.1 we can also observe different SD between the methods. The SAIF has the highest values, BFM that is characterized the lowest. This is consistent with the different accuracy of the algorithms. SAIF has larger number of parameters and thus the larger standard errors in the estimates: this may influence the inter-subject variability.
Consider now the bar graph of Figure 9.2. The image provides a graphic representation of rCPS estimated with the different methods. We can see again the same considerations as in Figure 9.1, i.e. that the NLLS-HOM-ROI estimates are higher than the other two methods, that BFM and SAIF are more similar to each other and that the SAIF provides the highest inter-subject variability among all the analyzed methods. In Figure 9.3 and 9.4 we report the estimates of λ. The BFM and SAIF methods are in good agreement, but NLLS-HOM-ROI provides lower values. The SD is very similar for all three methods. In Figure 9.5 and 9.6 we report the estimates and the bar graphs for the K1 (mL/g/min). As with λ the BFM-HOM-VOXEL and SAIF-ROI are similar but the NLLS-HOM-ROI estimates are visibly lower. The SD is the same in all the methods. In Figure 9.7 and 9.8 we report the V_b estimates. NLLS-HOM-ROI provides visibly higher estimates than the other two methods. In summary we can see in estimates of all the parameters that BFM-HOM-VOXEL and SAIF-ROI provide results in good agreement with each other, but differ from those provided by NLLS-HOM-ROI.

Comparison between different methods								
rCPS (nmol/g/min)	NLLS-HOM-ROI		BFM-HOM-VOXEL		SAIF-ROI	
ROI	mean	SD	mean	SD	mean	SD
WholeBrain	1.85	0.10	1.61	0.08	1.59	0.13
Cerebellum	2.20	0.12	1.96	0.10	1.86	0.14
Vermis	2.18	0.12	1.97	0.09	1.89	0.15
Frontal	2.16	0.13	1.90	0.08	1.85	0.11
Temporal	2.01	0.13	1.74	0.11	1.76	0.16
Occipital	2.33	0.20	2.09	0.17	1.94	0.22
Parietal	2.14	0.19	1.88	0.20	1.81	0.28
SupraorbitalGyrus	2.01	0.14	1.77	0.10	1.75	0.14
PreCentralGyrus	1.93	0.21	1.89	0.23	1.78	0.30
PostCentralGyrus	1.90	0.17	1.89	0.18	1.74	0.17
Thalamus	1.72	0.10	1.54	0.09	1.49	0.06
Putamen	1.45	0.10	1.34	0.07	1.32	0.10
Caudate	1.16	0.10	1.01	0.07	1.05	0.09
Hippocampus	1.82	0.14	1.46	0.15	1.60	0.20
Amygdala	1.63	0.12	1.32	0.11	1.41	0.18
Hypothalamus	1.37	0.21	1.22	0.23	1.21	0.35
CoronaRadiata	0.98	0.07	0.84	0.06	0.88	0.08
CentrumSemiovale	1.09	0.09	0.92	0.09	0.98	0.12
CerebellarWhiteMatter	1.37	0.12	1.21	0.14	1.14	0.16

Figure 9.1: rates of cerebral protein synthesis (nmol/g/min) estimated with different algorithms in different regions of interest. The values are the mean ± SD for 9 subjects.

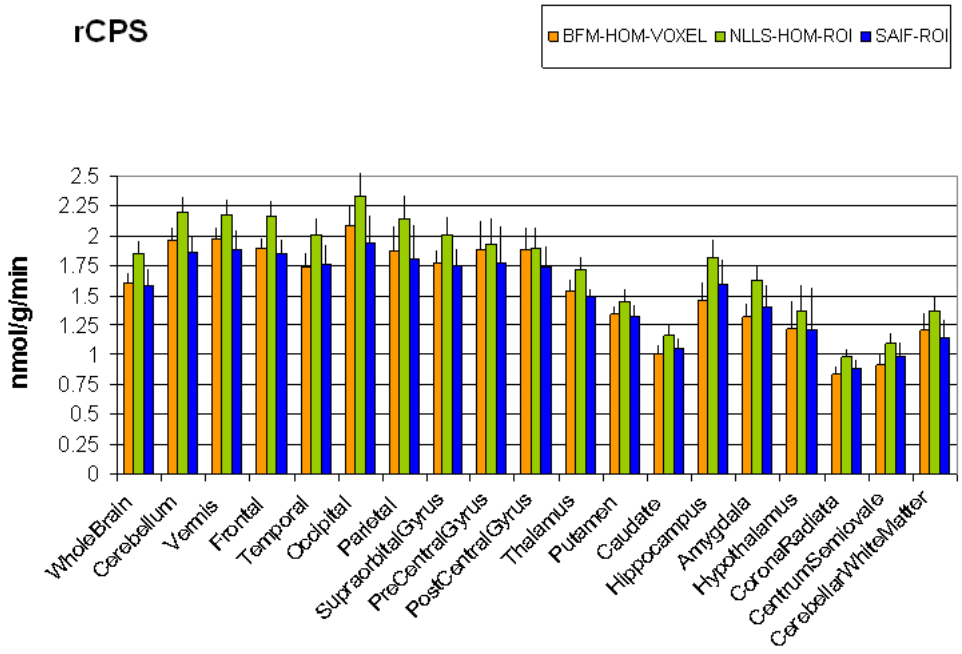

Figure 9.2: rates of cerebral protein synthesis (nmol/g/min) bar graph. The results are estimated with different algorithms in different regions of interest. The values are the mean for 9 subjects. The lines represent the SD.

Comparison Between different methods								
LAMBDA		BFM-HOM-VOXEL		NLLS-HOM-ROI		SAIF-ROI		
	ROI	mean	SD	mean	SD	mean	SD	
1	WholeBrain	0.76	0.02	0.7	0.03	0.76	0.03	
2	Cerebellum	0.78	0.02	0.75	0.03	0.79	0.02	
3	Vermis	0.77	0.03	0.74	0.04	0.78	0.04	
4	Frontal	0.74	0.02	0.70	0.03	0.74	0.03	
5	Temporal	0.74	0.03	0.69	0.03	0.73	0.03	
6	Occipital	0.75	0.03	0.73	0.04	0.78	0.03	
7	Parietal	0.75	0.03	0.71	0.03	0.76	0.04	
8	SupraorbitalGyrus	0.74	0.03	0.70	0.04	0.74	0.03	
9	PreCentralGyrus	0.76	0.02	0.72	0.03	0.77	0.04	
10	PostCentralGyrus	0.77	0.02	0.73	0.03	0.79	0.03	
11	Thalamus	0.77	0.02	0.74	0.03	0.78	0.02	
12	Putamen	0.79	0.02	0.78	0.02	0.79	0.03	
13	Caudate	0.78	0.02	0.74	0.02	0.77	0.03	
14	Hippocampus	0.74	0.02	0.65	0.04	0.69	0.05	
15	Amygdala	0.74	0.03	0.65	0.03	0.69	0.05	
16	Hypothalamus	0.79	0.03	0.74	0.03	0.78	0.05	
17	CoronaRadiata	0.78	0.02	0.73	0.03	0.75	0.02	
18	CentrumSemiovale	0.78	0.02	0.72	0.03	0.75	0.03	
19	CerebellarWhiteMatter	0.79	0.03	0.74	0.03	0.80	0.03	

Figure 9.3: λ estimated with different algorithms in different regions of interest. The values are the mean $\pm$ SD for 9 subjects.

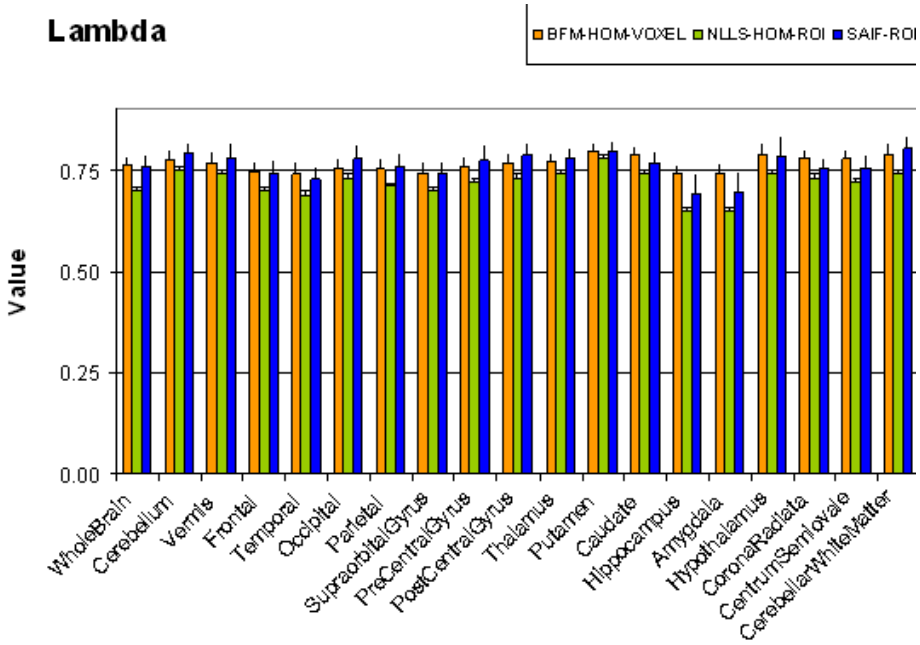

Figure 9.4: λ bar graph. The results are estimated with different algorithms in different regions of interest. The values are the mean for 9 subjects. The lines represent the SD

Comparison Between different methods							
K1 (mL/g/min)		BFM-HOM-VOXEL		NLLS-HOM-ROI		SAIF-ROI	
	ROI	mean	SD	mean	SD	mean	SD
1	WholeBrain	0.050	0.005	0.043	0.007	0.048	0.005
2	Cerebellum	0.069	0.007	0.062	0.007	0.067	0.007
3	Vermis	0.067	0.009	0.060	0.007	0.064	0.008
4	Frontal	0.053	0.006	0.048	0.005	0.051	0.005
5	Temporal	0.047	0.005	0.042	0.004	0.045	0.005
6	Occipital	0.065	0.007	0.058	0.005	0.064	0.007
7	Parietal	0.056	0.006	0.049	0.005	0.054	0.006
8	SupraorbitalGyrus	0.049	0.006	0.045	0.004	0.048	0.007
9	PreCentralGyrus	0.056	0.007	0.050	0.006	0.056	0.005
10	PostCentralGyrus	0.060	0.006	0.052	0.005	0.059	0.006
11	Thalamus	0.052	0.004	0.046	0.003	0.050	0.004
12	Putamen	0.052	0.006	0.047	0.006	0.049	0.006
13	Caudate	0.036	0.005	0.032	0.004	0.033	0.004
14	Hippocampus	0.037	0.004	0.032	0.004	0.035	0.004
15	Amygdala	0.033	0.003	0.029	0.002	0.031	0.003
16	Hypothalamus	0.043	0.008	0.038	0.005	0.042	0.010
17	CoronaRadiata	0.028	0.004	0.025	0.006	0.026	0.004
18	CentrumSemiovale	0.030	0.004	0.027	0.005	0.029	0.004
19	CerebellarWhiteMatter	0.045	0.007	0.038	0.007	0.044	0.007

Figure 9.5: K_1 estimated with different algorithms in different regions of interest. The values are the mean $\pm$ SD for 9 subjects.

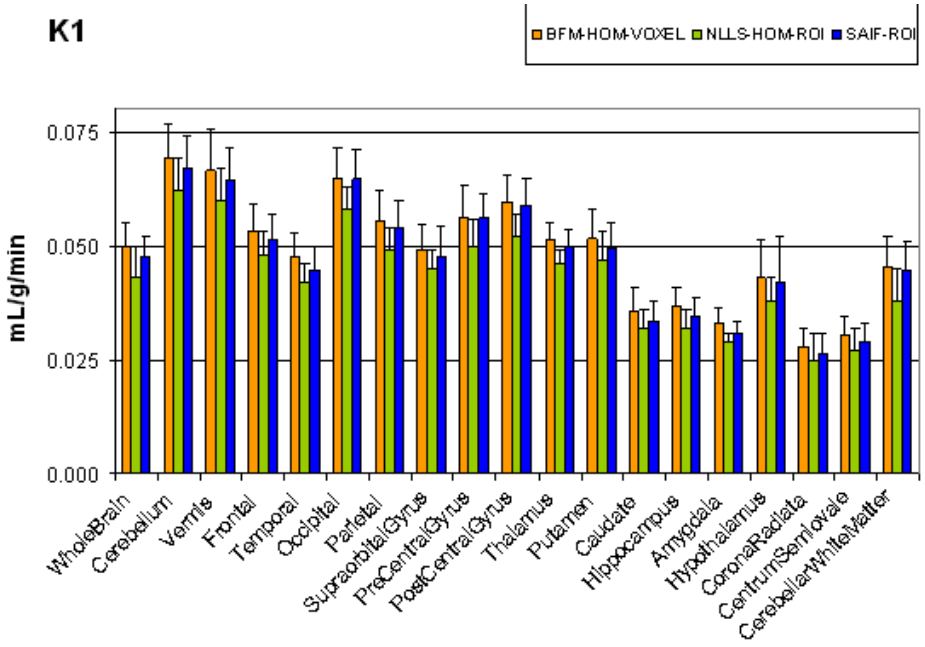

Figure 9.6: K_1 bar graph. The results are estimated with different algorithms in different regions of interest. The values are the mean for 9 subjects. The lines represent the SD.

Comparison Between different methods								
V_b		BFM-HOM-VOXEL		NLLS-HOM-ROI		SAIF-ROI		
	ROI	mean	SD	mean	SD	mean	SD	
1	WholeBrain	0.063	0.008	0.073	0.007	0.065	0.009	
2	Cerebellum	0.076	0.011	0.082	0.012	0.078	0.012	
3	Vermis	0.057	0.011	0.059	0.012	0.057	0.012	
4	Frontal	0.064	0.007	0.068	0.008	0.065	0.008	
5	Temporal	0.066	0.007	0.063	0.011	0.068	0.007	
6	Occipital	0.071	0.010	0.072	0.013	0.072	0.011	
7	Parietal	0.064	0.011	0.069	0.010	0.065	0.011	
8	SupraorbitalGyrus	0.054	0.007	0.070	0.012	0.055	0.007	
9	PreCentralGyrus	0.060	0.009	0.061	0.011	0.059	0.011	
10	PostCentralGyrus	0.057	0.009	0.057	0.008	0.057	0.009	
11	Thalamus	0.064	0.010	0.067	0.014	0.066	0.011	
12	Putamen	0.052	0.006	0.055	0.006	0.054	0.007	
13	Caudate	0.047	0.006	0.048	0.007	0.049	0.007	
14	Hippocampus	0.081	0.013	0.087	0.014	0.083	0.014	
15	Amygdala	0.062	0.013	0.065	0.014	0.064	0.014	
16	Hypothalamus	0.052	0.011	0.053	0.009	0.050	0.011	
17	CoronaRadiata	0.034	0.004	0.035	0.004	0.034	0.004	
18	CentrumSemiovale	0.034	0.004	0.037	0.004	0.035	0.004	
19	CerebellarWhiteMatter	0.044	0.007	0.05	0.008	0.044	0.008	

Figure 9.7: V_b estimated with different algorithms in different regions of interest. The values are the mean $\pm$ SD for 9 subjects.

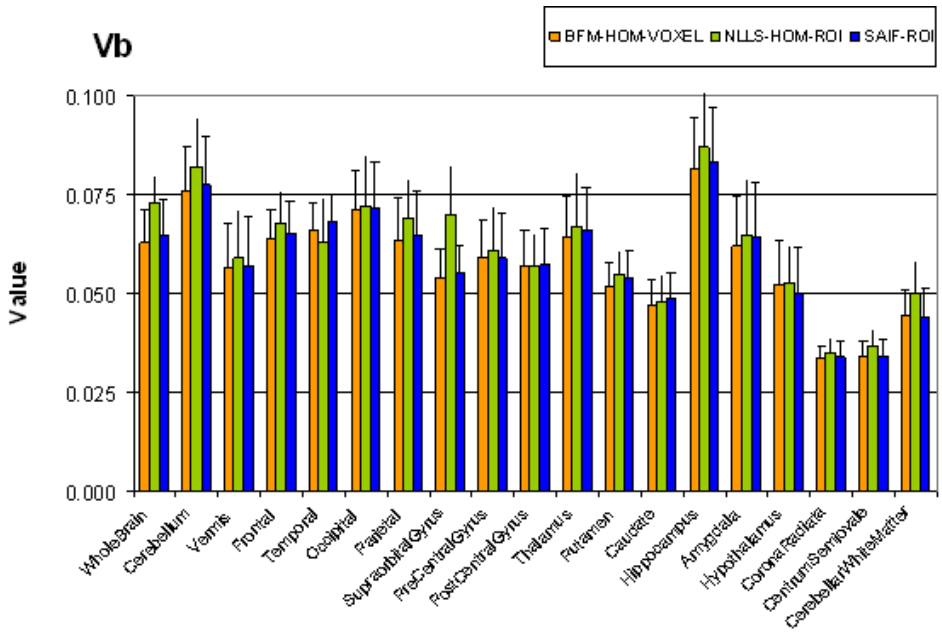

Figure 9.8: V_b bar graph. The results are estimated with different algorithms in different regions of interest. The values are the mean for 9 subjects. The lines represent the SD.

Chapter 10

Conclusions

The application of the NLLS based on the homogenous kinetic tissue model (HOM) to the leucine PET data at ROI level is not completely adequate for quantifying the rCPS and the other variables of interest. This fact is the consequence of the fact that HOM does not represent the mixture of tissues which are present in the data due the limited spatial resolution of the PET tomograph. The tissue heterogeneity that the HOM, by definition does not take into account influences the fit of the estimated-model curves with the data and the quality of estimates of the variables of interest. In fact, as previous application of the method have shown ([2];[35]) the typical trend of the HOM model-estimated curve underestimates and overestimates the data measures at the beginning and at the end of the data acquisition interval, respectively. The model specification error results in bias of the estimates provided by the NLLS-HOM-ROI: -20 to -30% for $k_2 + k_3$, -8% for λ and +15 to +20% for rCPS [35]. In light of these unsatisfactory values more accurate approaches for the rCPS quantification at ROI level are required.

A valid alternative to the NLLS-HOM-ROI is Spectral Analysis (SA). Based on a generic compartmental model, SA can be applied to heterogeneous as well as homogeneous tissues without

any prior assumptions concerning the number of tissue compartments. Firstly we used SA to choose the best compartmental model for the representation of the TACs associated with the different ROIs. Using an approach based on fixed SA models, i.e. fixing *a priori* different numbers of equilibrating components (with or without a trapping component) in different SA models, we determined the degree of heterogeneity necessary to explain the leucine PET data. From the Akaike Information Criterion the model with two equilibrating components and one trapping component was selected as the best. This SA model is consistent with the heterogeneous kinetic tissue model (HET) defined for the analysis of the leucine PET data [35]. This model, however, was not useful for analysis of measured data because the high number of parameters in the model caused convergence problems in the estimation process.

To overcome this limitation we applied the SA technique for quantifying the parameters of interest from the leucine PET data at ROI level. The traditional SA approaches, the Cunningham SA and the Turkheimer SA were tested and then applied to the measured data. The first method showed an excellent fit (WRSS < 3) of the data, but nonphysiological estimates of the variables of interest. The second, instead, presented a fit typical of the HOM model applied to ROI data and nonphysiological λ and rCPS estimates. The reason for the poor estimates of the variables of interest is related to the incapacity of the methods to provide a correct estimation of the spectra. The Cunningham SA method does not estimate the trapping component and the blood volume correctly. The Turkheimer SA technique, instead, is affected by problems with the slowest equilibrating components. These components are influenced by several of effects: noise in the PET data, distortion in the arterial signals, shifting of the trapping component, and the presence of real equilibrating components with slow kinetics.

Because these SA methods did not consistently produce reliable estimates when applied to L-[$1-^{11}C$]leucine data, we developed a new SA iterative filtering (SAIF) method to take into account all these facets of the rCPS estimation problem.
SAIF uses prior information concerning irreversibility of trapping of the tracer as well as components that cannot be distinguished from blood. This information determinates the value of a cut-off interval that the SAIF uses to select the range of the equilibrating components distinguishable in the data to be analyzed. A data-driven criterion to determinate the value of the cut-off is, however, missing. We used simulation-based approach for its choice.
Comparing SAIF with standard SA methods we observed that our method yielded the best fit, the lowest bias ($< 2\%$) and the lowest CV ($\sim 6\%$) in rCPS. In measured data, rCPS estimated with SAIF agreed with the average of rCPS values estimated by using HOM at the voxel level, but differed substantially from ROI-based rCPS estimated by HOM. This is consistent with the presence of a greater degree of tissue heterogeneity in the ROI, compared to individual voxels, that is not accounted for with the homogeneous tissue kinetic model. In most regions CVs with SAIF were somewhat higher than when a fixed kinetic model was used, probably due to the increased number of parameters estimated with SAIF.
Unlike the HOM, SAIF accounts for tissue heterogeneity and thus it was found to be a useful and robust method for estimating rCPS at the ROI level.

Appendix A

The data weighted

All the algorithms for the parameter estimation used in this work, like the NLLS for the HOM (Section 3.1), the WLLS for the BFM (Section 8.1) or the *lsqnonneg.m* for SA (Section 7.1), utilize for their processing the same weighted data approach in which the weight of a measure is inversely proportional to its standard deviation. The following equation represents this relationship

$$W_i = \frac{1}{SD_i} \tag{A.1}$$

where W_i and SD_i are the weight and the standard deviation of the i-data point, respectively.
With this formulation the problem of how to weight the data becomes the problem of how represent the error in the measured data. To resolve the problem we assumed that the measured activity follows Poisson statistics [42]. If we define the following variables as

- X_i= total counts Frame i (not decay-corrected)
- Y_i= count rate Frame i (not decay-corrected)
- Z_i= count rate Frame i (decay-corrected)
- Δt_i= Length Frame i

- t_i= Midscan time, Frame i
- K= decay constant ^{11}C = $ln(2)/20.38$ min

From the Poisson equation we know that

$$Variance(X_i) = X_i \tag{A.2}$$

i.e.

$$SD(X_i) = \sqrt{X_i} \tag{A.3}$$

For definition of count rate

$$Y_i = \frac{X_i}{\Delta t_i} \tag{A.4}$$

so

$$SD(Y_i) = SD\left(\frac{X_i}{\Delta t_i}\right) = \frac{\sqrt{X_i}}{\Delta t_i} = \frac{\sqrt{Y_i \Delta t_i}}{\Delta t_i} = \sqrt{\frac{Y_i}{\Delta t_i}} \tag{A.5}$$

From the expression for the decay correction we know that $Z_i = e^{K \cdot t_i} Y_i$ and in the same way $Y_i = e^{-K \cdot t_i} Z_i$.
Using these expressions combined with Equation A.5 we can write

$$\begin{aligned} SD(Z_i) = \;& SD(e^{K \cdot t_i} Y_i) \;\; = e^{K \cdot t_i} SD(Y_i) \\ = \;& e^{K \cdot t_i} \sqrt{\tfrac{Y_i}{\Delta t_i}} \;\; = \sqrt{\tfrac{e^{K \cdot t_i} Z_i}{\Delta t_i}} \end{aligned} \tag{A.6}$$

Equation A.6 is exactly the same, with some difference in notation, to that reported in (3.2), namely

$$Variance(C_T(t_i)) = N s_i^2 = N \sqrt{\frac{e^{\gamma \cdot t_i} C_T(t_i)}{\Delta t_i}} \tag{A.7}$$

where t_i is the midpoint of the i-th frame, γ is the decay constant for ^{11}C, Δt_i is the length of Frame i, N is a proportionality coefficient reflecting the noise level in the data and $C_T(t_i)$ is the total activity registered by the scanner.
In PET N is *a priori* unknown, but its value is not necessary for the estimation because it is only a scale factor. N is only required to calculate the precision of estimated parameters and for this reason it is estimated *a posteriori* [6].

Appendix B

The relationship between rCPS and the HOM parameters

To justify the equation

$$\text{rCPS} = \left(\frac{K_1 k_4}{k_2 + k_3} \right) C_p \tag{B.1}$$

is necessary to consider the equation of the HOM model for the unlabelled leucine

$$\begin{cases} \frac{dC_E}{dt} &= K_1 C_p(t) - (k_2 + k_3 + k_4) C_E(t) + k_5 P(t) \\ \frac{dP}{dt} &= k_4 C_E(t) - k_5 P(t) \end{cases} \tag{B.2}$$

where C_E is free unlabelled leucine in the tissue, P is the unlabelled leucine incorporated into protein in the tissue, C_p is the free leucine in the plasma and K_1, k_2, k_3, k_4 and k_5 are the rate constants of the homogeneous kinetic model for the unlabelled leucine (3.2).
One of the hypotheses of this model is that the leucine is in steady state in both the compartments. This means that

$$\begin{cases} \frac{dC_E}{dt} &= 0 \\ \frac{dP}{dt} &= 0 \end{cases} \tag{B.3}$$

In light of this B.2 can be written as

$$\begin{cases} K_1 C_p(t) - (k_2 + k_3 + k_4) C_E(t) k_5 P(t) &= 0 \\ k_4 C_E(t) - k_5 P(t) &= 0 \end{cases} \tag{B.4}$$

For its definition rCPS is the rate of proteins synthesis so it corresponds to the flux of leucine that comes from the free leucine compartment C_E to the Protein compartment

$$\text{rCPS} = k_4 C_E \tag{B.5}$$

Combing the two equations in B.4 it is possible to write that

$$C_E = \left(\frac{K_1}{k_2 + k_3} \right) C_p \tag{B.6}$$

Using Equations in B.5 in B.6 we obtain

$$\text{rCPS} = k_4 \left(\frac{K_1}{k_2 + k_3} \right) C_p = \left(\frac{K_1 k_4}{k_2 + k_3} \right) C_p \tag{B.7}$$

That is exactly Equation B.1, i.e. the relationship between rCPS and the homogenous model parameters.

Appendix C

The SAIF

In this section we report the details of the Spectral Analysis Iterative Filter algorithm

C.1 Algorithm - The MAIN PROGRAM

- *Set up of the SA model variables: We initialized the following variables:*
  - ⇒ Number of components (default: N=100)
  - ⇒ Kind of grid (default: DiStefano distribution)
  - ⇒ Choice of the Cut-off interval (default: Optimal value selected from simulation)

For subject=1 to 9

- *Load the arterial signals of the subject;*
- *Correction of the blood signal from the pre-determined tracer arrival delay;*
- *Set up of the SA required data:*
  - ⇒ Load of the ROI Leucine PET data (*OriginalPET-Data*);

⇒ Construction of Transfer Matrix (Figure C.1) through the convolutions between the betas of the grid and the plasma samples;

- **For ROI=1 to NumberOfROI**

  ⇒ Evaluation of the data weights

  ⇒ Reduction of the Transfer Matrix to the PET sampling grid

  ⇒ `Spectral Analysis Iterative Filter`

  ⇒ Conversion of the spectrum into the variables of interest

- **End ROI cycle**

End subject cycle.

Legend:	
N	number of betas in the grid
$NumberOfROI$	number of ROI examined for each subject

C.2 Algorithm - The SAIF

- Cunningham SA: The first Spectrum S (where S is the vector of α_i and V_b) is estimated applying the $lsqnonneg.m$ to the Transfer Matrix and the $OriginalPETData$;

- WRSS is calculated from the model-estimated curve and the $OriginalPETData$;

- Set Up for the iterative filter: From the Transfer Matrix we define the External component matrix M_e using the columns that refer to the trapping component and the blood component, and the Internal component matrix M_i using

the part of the Transfer Matrix related to equilibrating components inside the cut-off interval (Figure C.1);

- 1st filtering:

  ⇒ We defined *ModifiedPETData1 = OriginalPETData - Contributions* of M_i (Calculated from S)

  ⇒ New values of the trapping component and Vb are estimated applying *lsqnonneg.m* to the M_e and *ModifiedPETData1*. S is updated with the new estimates;

- 2nd filtering:

  ⇒ Define *ModifiedPETData2 = OriginalPETData - Contributions* of M_e (Calculated from S)

  ⇒ New values of equilibrating components are estimated applying *lsqnonneg.m* to the M_i and *ModifiedPETData2*. S is updated with the new estimates;

- A new value for WRSS is calculated after the two filtering steps. If the difference with the old value is more than 0.1% the algorithm restarts from the 1st filtering. If not, the algorithm exits from the correction cycle and last version of the spectrum S defines the final estimated spectrum S^*;

- Correction for the doubling effect in S^* by the Equation (4.3);

- Estimation of the CV for the detected components in S^* and V_b through the inverse of the Jacobian Matrix.

Figure C.1: The SAIF Matrices. The scheme shows how from the Transfer Matrix we defined the Internal and External component Matrixes, M_i and M_e, respectively, necessary for the iterative filtering cycle.

Appendix D

The BFM algorithm for the non-negativity correction

This is the algorithm used for the negativity correction of the parameters estimated with BFM [35]. The rate constants and the equations refer to the ones used to describe BFM (Equations 8.1-8.10). Defined by Giampaolo Tomasi of Yale University the method yields nonnegative estimates without using a non linear estimation approach. However, this algorithm doesn't work for all the voxels because some of them, even though only a very small fraction (generally $< 1\%$), cannot be corrected. Rather than apply a costly constrained NLLS approach, these voxels were omitted from the ROI averages.

Algorithm

Let Θ^*= [Θ_1^*,Θ_2^*,Θ_3^*] be the estimated parameter vector at $\beta = \beta^*$. Calculate K_1, $k_2 + k_3$, k_4 and V_b from Equations (Equations 8.7-8.10).

If $K_1 \leq 0$ or $k_2 + k_3 \leq 0$:
Discard voxel.
Else if $V_b < 0$:
Set $\Theta_3^* = V_b = 0$ in Eq (8.3) and re-estimate Θ^*= [Θ_1^*,Θ_2^*].

Calculate K_1, $k_2 + k_3$, k_4 from Eqs (8.7-8.9) .

If $k_4 < 0$:

Set $\Theta_2^* = \Theta_3^* = 0$ in Eq (8.3) and re-estimate Θ^*=$[\Theta_1^*]$

Set $k_4 = 0$ and calculate K_1, $k_2 + k_3$ from Eqs (8.7-8.8).

If $K_1 \leq 0$ or $k_2 + k_3 \leq 0$ discard voxel; otherwise retain voxel.

Else if $k_4 < 0$:

Set $\Theta_2 = 0$ in Eq (8.3) and re-estimate Θ^*= $[\Theta_1^*, \Theta_3^*]$.

Set $k_4 = 0$ and calculate K_1, $k_2 + k_3$, V_b from Eqs (8.7, 8.8, 8.10).

If $V_b < 0$:

Set $\Theta_2^* = \Theta_3^* = 0$ in Eq 8.3 and re-estimate Θ^*=$[\Theta_1^*]$

Set $V_b = 0$ and calculate K_1, $k_2 + k_3$ from Eqs (8.7, 8.8).

If $K_1 \leq 0$ or $k_2 + k_3 \leq 0$ discard voxel; otherwise retain voxel.

Else

Retain voxel.

End

Bibliography

[1] A. Bertoldo, P. Vicini, G. Sambuceti, A. A. Lammertsma, O. Parodi, and C. Cobelli. Evaluation of compartmental and spectral analysis models of [^{18}F]FDG kinetics for heart and brain studies with PET. *IEEE Trans Biomed Eng*, 45(12):1429–48, 1998.

[2] S. Bishu, K. C. Schmidt, T. Burlin, M. Channing, S. Conant, T. Huang, Z. H. Liu, M. Qin, A. Unterman, Z. Xia, A. Zametkin, P. Herscovitch, and C. B. Smith. Regional rates of cerebral protein synthesis measured with L-[1-^{11}C]leucine and PET in conscious, young adult men: normal values, variability, and reproducibility. *J Cereb Blood Flow Metab*, 28(8):1502–13, 2008.

[3] S. Bishu, KC Schmidt, and CB Smith. Propofol anesthesia does not alter the regional rates of cerebral protein synthesis measured with L-[1-^{11}C]leucine and PET in healthy male subjects. *J Cereb Blood Flow Metab*, 2009.

[4] D. J. Brooks, A. A. Lammertsma, R. P. Beaney, K. L. Leenders, P. D. Buckingham, J. Marshall, and T. Jones. Measurement of regional cerebral pH in human subjects using continuous inhalation of $^{11}CO_2$ and positron emission tomography. *J Cereb Blood Flow Metab*, 4(3):458–65, 1984.

[5] R. B. Buxton, N. M. Alpert, V. Babikian, S. Weise, J. A. Correia, and R. H. Ackerman. Evaluation of the $^{11}CO_2$

positron emission tomographic method for measuring brain pH. I. pH changes measured in states of altered PCO_2. *J Cereb Blood Flow Metab*, 7(6):709–19, 1987.

[6] R.E. Carson, C. Cobelli, and L. Filkestein. *The Mathematical Modeling of Metabolic and Endocrine Systems*. Wiley, New York, 1993.

[7] R. C. Collins, N. Nandi, C. B. Smith, and L. Sokoloff. Focal seizures inhibit brain protein synthesis. *Trans Am Neurol Assoc*, 105:43–6, 1980.

[8] V. J. Cunningham and T. Jones. Spectral analysis of dynamic PET studies. *J Cereb Blood Flow Metab*, 13(1):15–23, 1993.

[9] B Efron. Bootstrap methods: another look at the jackknife. *Ann. Statistic*, 1979.

[10] Carson R et. al. Design of a motion-compensation OSEM list-mode algorithm for resolution-recovery reconstruction for the HRRT, 2003.

[11] Johnson CA et. al. Software architetture of the MOLAR-HRRT recostruction engine. *IEEE Trans. Nucl Sci.*, 2004.

[12] B. Fischer and J. Modersitzki. Intensity-based image registration with a guaranteed one-to-one point match. *Methods Inf Med*, 2004.

[13] Akaike Hirotugu. On a decision procedure for system identification. *Engineering approach to computer control*, 1971.

[14] H. Hsu, V.R. Young, and A.J. Fischman. Measurement of muscle protein synthesis by positron emission tomography with L-[methyl-^{11}C]methionine. *Proc Natl Acad Sci USA*, 1996.

[15] H. Iida, S. Higano, N. Tomura, F. Shishido, I. Kanno, S. Miura, M. Murakami, K. Takahashi, H. Sasaki, and K. Uemura. Evaluation of regional differences of tracer appearance time in cerebral tissues using [^{15}O] water and dynamic positron emission tomography. *J Cereb Blood Flow Metab*, 8(2):285–8, 1988.

[16] M. C. Ingvar, P. Maeder, L. Sokoloff, and C. B. Smith. Effects of ageing on local rates of cerebral protein synthesis in sprague-dawley rats. *Brain*, 108 (Pt 1):155–70, 1985.

[17] A. Lajtha, L. Latzkovits, and J. Toth. Comparison of turnover rates of proteins of the brain, liver and kidney in mouse in vivo following long term labeling. *Biochim Biophys Acta*, 425(4):511–20, 1976.

[18] E. M. Landaw and 3rd DiStefano, J. J. Multiexponential, multicompartmental, and noncompartmental modeling. II. data analysis and statistical considerations. *Am J Physiol*, 246(5 Pt 2):R665–77, 1984.

[19] K. Murase. Spectral analysis: principle and clinical applications. *Ann Nucl Med*, 17(6):427–34, 2003.

[20] K. Murase, T. Tsuda, T. Mochizuki, and J. Ikezoe. Hepatic extraction fraction of hepatobiliary radiopharmaceuticals measured using spectral analysis. *Nucl Med Commun*, 20(11):1041–5, 1999.

[21] K. Murase, T. Tsuda, T. Mochizuki, S. Tanada, and J. Ikezoe. Spectral analysis applied to hepatobiliary dynamic scintigraphy with 99Tcm-N-pyridoxyl-5-methyltryptophan. *Nucl Med Commun*, 18(11):1049–56, 1997.

[22] H. Nakanishi, Y. Sun, R. K. Nakamura, K. Mori, M. Ito, S. Suda, H. Namba, F. I. Storch, T. P. Dang, W. Mendelson,

M. Mishkin, C. Kennedy, J. C. Gillin, C. B. Smith, and L. Sokoloff. Positive correlations between cerebral protein synthesis rates and deep sleep in macaca mulatta. *Eur J Neurosci*, 9(2):271–9, 1997.

[23] PV. Nguyen, T. Abel, and E.R. Kandel. Requirement of a critical period of transcription for induction of a late phase of LTP. *Science*, 1994.

[24] C.S. Patlak and R.G. Blasberg. Graphical evaluation o of blood-to-brain transfer constants from multiple-time uptake data. *J Cereb Blood Flow Metab*, 1985.

[25] M. Qin, J. Kang, T. V. Burlin, C. Jiang, and C. B. Smith. Postadolescent changes in regional cerebral protein synthesis: an in vivo study in the FMR1 null mouse. *J Neurosci*, 25(20):5087–95, 2005.

[26] Hawkins RA. Estimation of local cerebral protein synthesis rates with L-[1-^{11}C]leucine and PET: methods, model, and results in animals and humans. *Cereb Blood Flow Metab*, 1989.

[27] K. Schmidt. Which linear compartmental systems can be analyzed by spectral analysis of PET output data summed over all compartments? *J Cereb Blood Flow Metab*, 19(5):560–9, 1999.

[28] K. C. Schmidt, M. P. Cook, M. Qin, J. Kang, T. V. Burlin, and C. B. Smith. Measurement of regional rates of cerebral protein synthesis with L-[1-^{11}C]leucine and PET with correction for recycling of tissue amino acids: I. kinetic modeling approach. *J Cereb Blood Flow Metab*, 25(5):617–28, 2005.

[29] C. B. Smith and J. Kang. Cerebral protein synthesis in a genetic mouse model of phenylketonuria. *Proc Natl Acad Sci U S A*, 97(20):11014–9, 2000.

[30] C. B. Smith, K. C. Schmidt, M. Qin, T. V. Burlin, M. P. Cook, J. Kang, R. C. Saunders, J. D. Bacher, R. E. Carson, M. A. Channing, W. C. Eckelman, P. Herscovitch, P. Laverman, and B. K. Vuong. Measurement of regional rates of cerebral protein synthesis with L-[1-^{11}C]leucine and pet with correction for recycling of tissue amino acids: II. validation in rhesus monkeys. *J Cereb Blood Flow Metab*, 25(5):629–40, 2005.

[31] C.B. Smith. Measurament of local cerebral protein synthesis in vivo: influence of recyling of amino acids derived from protein degradation. *Proc Natl Acad Sci USA*, 85(23):9341–5, December 1988.

[32] A.R. Studenov, D.E. Szalda, and Ding Y.S. Synthesis of nocarrier-added C-^{11} labeled D- and l-enantiomers of phenylalanine and tyrosine for comparative PET studies. *Nucl Med Biol*, 2003.

[33] Y. Sun, G. E. Deibler, J. Jehle, J. Macedonia, I. Dumont, T. Dang, and C. B. Smith. Rates of local cerebral protein synthesis in the rat during normal postnatal development. *Am J Physiol*, 268(2 Pt 2):R549–61, 1995.

[34] S. K. Sundaram, O. Muzik, D. C. Chugani, F. Mu, T. J. Mangner, and H. T. Chugani. Quantification of protein synthesis in the human brain using L-[1-^{11}C]-leucine PET: incorporation of factors for large neutral amino acids in plasma and for amino acids recycled from tissue. *J Nucl Med*, 47(11):1787–95, 2006.

[35] G. Tomasi, A. Bertoldo, and K. Schmidt. Voxel-based estimation of kinetic model parameters of the L-[1-^{11}C]leucine PET method for determination of regional rates of cerebral protein synthesis: Validation and comparison with region-of-interest based methods. *Submitted to Journal of Cerebral Blood Flow Metabolism*, 2009.

[36] F. Turkheimer, R. M. Moresco, G. Lucignani, L. Sokoloff, F. Fazio, and K. Schmidt. The use of spectral analysis to determine regional cerebral glucose utilization with positron emission tomography and [^{18}F]fluorodeoxyglucose: theory, implementation, and optimization procedures. *J Cereb Blood Flow Metab*, 14(3):406–22, 1994.

[37] F. Turkheimer, L. Sokoloff, A. Bertoldo, G. Lucignani, M. Reivich, J. L. Jaggi, and K. Schmidt. Estimation of component and parameter distributions in spectral analysis. *J Cereb Blood Flow Metab*, 18(11):1211–22, 1998.

[38] J. Ventura, R. P. Liberman, M. F. Green, A. Shaner, and J. Mintz. Training and quality assurance with the structured clinical interview for DSM-IV (SCID-I/P). *Psychiatry Res*, 79(2):163–73, 1998.

[39] R. Widmann, M. Kocher, R. I. Ernestus, and K. A. Hossmann. Biochemical and autoradiographical determination of protein synthesis in experimental brain tumors of rats. *J Neurochem*, 59(1):18–25, 1992.

[40] R. Widmann, T. Kuroiwa, P. Bonnekoh, and K. A. Hossmann. [^{14}C]leucine incorporation into brain proteins in gerbils after transient ischemia: relationship to selective vulnerability of hippocampus. *J Neurochem*, 56(3):789–96, 1991.

[41] K Wienhard. The ECAT HRRT: Performance and first clinical application of the new high resolution research tomogrph. *IEEE Trans Nucl Sci*, pages 104–110, 2002.

[42] Y. Wu and R. E. Carson. Noise reduction in the simplified reference tissue model for neuroreceptor functional imaging. *J Cereb Blood Flow Metab*, 22(12):1440–52, 2002.

Acknowledgment

I thank my professor Alessandra Bertoldo for the possibility to write my thesis in an important research center, such as the NIH. I thank Kathleen Schmidt for the invaluable teaching that she provided me during all my work. I thank the SNPM, in particular the chief Carolyn Beebe Smith, PhD., Dr. Bishu, Aaron and Ariel for the help and the patience that they had with me and my English. I thank also the Bioengineering group of Padova, in particular Denis who taught some interesting "secrets"of Matlab. Thank you to everyone that has contributed to the realization of this work.